

ABSTRACT

CHERON, CHARLES MARIE NICOLAS. Implementation and Testing of High Burnup Fuel Performance Models in CTF. (Under the direction of Dr. Maria Avramova).

As nuclear fuel technology develops, updated methodologies and computational tools are needed for safety analysis prior to commercial operation. For high burnup nuclear fuel simulations in system and subchannel thermal-hydraulic codes, a need is present for updated modeling of phenomena such as the steady state and transient fission gas release, changes in fuel and cladding material structure, fuel fragmentation, relocation and dispersal, fuel pellet-cladding mechanical interaction, among others. A literature review is performed on the relevant phenomena and their state-of-the-art modeling. An analysis of the current capabilities and shortcomings in the high burnup nuclear fuel models of the advanced subchannel thermal-hydraulic code CTF is presented. CTF is updated to include both steady state and transient fission gas release models and supporting submodels for the modeling of high burnup and high enrichment fuels. Following implementation, a verification process is conducted using a wide range of burnup and enrichments values, and the code is validated for use in high burnup reactivity insertion calculations.

Test cases are taken from the HERA Modeling and Simulation benchmark to ascertain CTF's fuel performance capabilities. The steady state fission gas release model is verified and validated using data from the FRAPCON integral assessment. The transient fission gas release model is validated using data from the FRAPTRAN integral assessment.

A sensitivity study using HERA benchmark data shows good agreement in CTF's enthalpy prediction capabilities compared to experimental RIA data at low burnup. The steady state fission gas release model verification obtains mixed results. CTF overpredicts fission gas release,

maintaining conservatism. However, the overprediction is significant in situations where axially uniform power profiles are input, especially at lower burnups. Taking all cases, CTF overpredicts by 11% FGR. The accuracy of the CTF prediction excluding the axially uniform cases is 3.25% FGR. The transient release model validation also shows good agreement with the FRAPTRAN fission gas release predictions, though the code tends to underpredict the FGR values, particularly at higher burnups.

In short, multiple fuel performance models were implemented or enhanced in CTF to improve its predictive capabilities with respect to fuel performance in reactivity insertion accidents. The range of applicability of this updated version of CTF is presented, as well as validation metrics. Future work is proposed for continuous improvement of CTF's fuel performance capabilities.

© Copyright 2025 by Charles Cheron

All Rights Reserved

Implementation and Testing of High Burnup Fuel Performance Models in CTF

By: Charles Marie Nicolas Cheron

A dissertation submitted to the Graduate Faculty of
North Carolina State University in partial fulfillment of the
requirements for the degree of Doctor of Philosophy

Nuclear Engineering

Raleigh, North Carolina

2025

APPROVED BY:

Dr. Maria Avramova

Committee Chair

Dr. Agustin Abarca

Dr. Gregory Stehle

Dr. Michael Goshe

Dr. Kostadin Ivanov

Dr. Grigorios Delipei

Mr. Yixing Sung

BIOGRAPHY

Charles Cheron is a graduate nuclear engineering student at the North Carolina State University College of Engineering. Hailing from the American South through his mother and France through his father, he has always had a particular interest in engineering and the STEM field in general. He received a bachelor's and a master's degree in nuclear engineering from North Carolina State University in 2021 and 2023, respectively. He is interested in computational Thermal Hydraulics, with experience in the COBRA family of codes and in fuel performance modeling. He currently resides in Raleigh, North Carolina, and following the obtention of his PhD in nuclear engineering, plans to work in industry using and improving computational tools for reactor safety analysis.

ACKNOWLEDGMENTS

I would like to express my deepest appreciation to Dr. Maria Avramova, Dr. Agustin Abarca, Dr. Grigorios Delipei, and Dr. Kostadin Ivanov, and Dr. Michael Goshe without whom this project would not have achieved fruition. I would also like to thank the contributions of Westinghouse Electric Company, both for their support and expertise. This endeavor would also not have been possible without the expert knowledge of Yixing Sung and Gregory Stehle. Lastly, I would like to acknowledge the contributions of Paul-Ernest Cheron, Elizabeth Cheron, and Anna Elizabeth McCormick for their combined support over the past four years.

This material is based upon work supported by the Department of Energy under Award Number DE-NE00090333.

This report was prepared as an account of work sponsored by an agency of the United States Government. Neither the United States Government nor any agency thereof, nor any of their employees, makes any warranty, express or implied, or assumes any legal liability or responsibility for the accuracy, completeness, or usefulness of any information, apparatus, product, or process disclosed, or represents that its use would not infringe privately owned rights. Reference herein to any specific commercial product, process, or service by trade name, trademark, manufacturer, or otherwise does not necessarily constitute or imply its endorsement, recommendation, or favoring by the United States Government or any agency thereof. The views and opinions of authors expressed herein do not necessarily state or reflect those of the United States Government or any agency thereof.

TABLE OF CONTENTS

ABSTRACT.....	i
BIOGRAPHY	ii
ACKNOWLEDGMENTS	iii
TABLE OF CONTENTS.....	iv
LIST OF TABLES.....	vi
LIST OF FIGURES	vii
LIST OF ACRONYMS	ix
CHAPTER 1 - Introduction	1
Background.....	1
Motivation.....	2
CHAPTER 2 – High Burnup Fuel Behavior.....	5
Introduction.....	5
High Burnup Structures	5
Fission Gas Release	14
Transient Fission Gas Release	22
Other Phenomena in High Burnup Nuclear Fuel.....	25
CHAPTER 3 – Review of Current CTF Capabilities	31
Introduction.....	31
Available Models in CTF.....	32
Gaps in CTF Modeling Capabilities	55
CHAPTER 4 – Modeling Approaches for Fission Gas Release.....	57
Introduction.....	57
Steady State Fission Gas Release Models	58
Transient Fission Gas Release Models	64
Non-FGR Modeling Improvements.....	69
CHAPTER 5 – Model Implementation and Test Cases.....	74
Introduction.....	74
CTF Steady State FGR Implementation	75
CTF Transient Implementation.....	80
Test Case Description	83
CHAPTER 6 – Results.....	93
FRAPCON to CTFFuel.....	93

FRAPTRAN to CTFFuel	103
HERA Sensitivity Study	104
CHAPTER 7 – Discussion.....	112
Discussion	112
CHAPTER 8 – Conclusion and Future Work.....	119
Conclusion	119
Future Work	120
References	122
APPENDICES	128
Appendix A: Description of fgr.ctf input file	129

LIST OF TABLES

Table 1: Material Property Modeling Options in CTF	38
Table 2: Empirical Coefficients for UO ₂ Specific Heat Capacity	41
Table 3: Fuel Performance Models in CTF	43
Table 4: Fuel Deformation Modeling Options in CTF	47
Table 5: Hoppe Irradiation Creep Material Constants in CTF	53
Table 6: ESCORE Clad Creep Model Material Constants	55
Table 7: MATPRO-11 Fuel Enthalpy Constants	72
Table 8: Steady State FGR Validation Cases	86
Table 9: CTFFuel Modeling Options.....	87
Table 10: Transient FGR V&V Test Cases	89
Table 11: HERA M&S Exercise Part 1 Test Matrix.....	90
Table 12: Experimental Difference between TREAT and NSRR Facilities.....	91
Table 13: HERA M&S Exercise Part 1 Experimental Parameters	92
Table 14: FRAPCON vs. CTFFuel Integral Steady State FGR values.....	94
Table 15: tFGR Simulation Results	104
Table 16: Adiabatic Gap Peak RAE Calculations	106
Table 17: Peak RAE Calculations using Updated Numerical Scheme in CTF	106

LIST OF FIGURES

Figure 1: Ceramography of LWR rim regions at high burnup showing the fully developed high burnup structure [4].....	7
Figure 2: Radial porosity distribution in high burnup samples measure through optical microscopy [14].....	8
Figure 3: Fission gas bubble diameter prior (left) and post (right) to recrystallization of grains in high burnup fuel [13]	9
Figure 4: Influence of HBS on thermal diffusivity of high burnup uranium dioxide fuel [14]....	11
Figure 5: Pre (top) and Post (bottom) irradiation LOCA transient fuel fragmentation for low (left) and medium (right) burnup fuel rods [19]	13
Figure 6: Fuel Fragmentation in HBS [19].....	14
Figure 7: Fission product yield by mass [24].....	16
Figure 8: Formation and growth of grain boundary bubbles	18
Figure 9: Cracking of LWR fuel pellet [18]	21
Figure 10: Cladding rupture and ballooning following transient fission gas release [37].....	24
Figure 11: Ballooned region of cladding with relocation of fuel present [19]	27
Figure 12: Fragmented fuel at rupture plane [19].....	28
Figure 13: Estimate Thresholds for UO ₂ fuel pellet melting under BWR CZP RDA and PWR HZP REA [8].....	30
Figure 14: NRC provided tFGR correlation with experimental data points provided [73]	65
Figure 15: FRAPTRAN tFGR model logic [74].....	66
Figure 16: Micro-cracking parameter for BISON code tFGR model [78]	68
Figure 17: CTF Selection Algorithm for Heat Transfer Regime [3]	71
Figure 18: Proposed CTF FGR Algorithm	82
Figure 19: FRAPTRAN tFGR Model Logic and Release	83
Figure 20: HERA M&S Exercise Part 1 Experimental Capsule.....	91
Figure 21: Case 28i6 Steady State Fission Gas Release	95
Figure 22: Case 36i8 Steady State Fission Gas Release	96
Figure 23: Case 111i5 Steady State Fission Gas Release	96
Figure 24: Case 332 Steady State Fission Gas Release	97
Figure 25: Case 429-DH Steady State Fission Gas Release	97
Figure 26: Case 4110-ae2 Steady State Fission Gas Release	98
Figure 27: Case 4110-be2 Steady State Fission Gas Release	98
Figure 28: Case 15309 Steady State Fission Gas Release	99
Figure 29: Case BNFL-DE Steady State Fission Gas Release	99
Figure 30: Case BNFL-DH Steady State Fission Gas Release.....	100
Figure 31: Case CBP Steady State Fission Gas Release.....	100
Figure 32: Case CBR Steady State Fission Gas Release	101
Figure 33: Case CBY Steady State Fission Gas Release	101
Figure 34: Case EPL-4 Steady State Fission Gas Release.....	102
Figure 35: Case IFA597-3 Steady State Fission Gas Release	102
Figure 36: Case LFF Steady State Fission Gas Release	103
Figure 37: HERA Test Case 1 Bishop-Sandberg-Tong Peak Cladding Temperature	107
Figure 38: HERA Test Case 1 Bishop-Sandberg-Tong RAE.....	108
Figure 39: HERA Test Case 6 Bishop-Sandberg-Tong Peak Cladding Temperature	108
Figure 40: HERA Test Case 6 Bishop-Sandberg-Tong RAE.....	109

Figure 41: HERA Test Case 1 Condie-Bengston-IV Peak Cladding Temperature 109
Figure 42: HERA Test Case 1 Condie-Bengston-IV RAE..... 110
Figure 43: HERA Test Case 6 Condie-Bengston-IV Peak Cladding Temperature 110
Figure 44: HERA Test Case 6 Condie-Bengston-IV RAE..... 111
Figure 45: Sample fgr.ctf input file..... 130

LIST OF ACRONYMS

BWR	Boiling Water Reactor
CASL	Consortium for the Advanced Simulation of Light Water Reactors
CHF	Critical Heat Flux
COBRA-TF	Coolant Boiling in Rod Arrays- Two Fluid
CTF	COBRA-TF
DNB	Departure from Nucleate Boiling
DOE	Department of Energy
EPMA	Electron Probe Microanalysis
EPRI	Electric Power Research Institute
FFRD	Fuel Fragmentation, Relocation, and Dispersal
FGR	Fission Gas Release
FP	Fission Product
HBHE	High Burnup High Enrichment
HBS	High Burnup Structure
HBU	High Burnup
HRTEM	High-Resolution Transmission Electron Microscopy
INL	Idaho National Laboratory
LWR	Light Water reactor
LOCA	Loss of Coolant Accident
NCSU	North Carolina State University
NRC	Nuclear Regulatory Commission
NSRR	Nuclear Safety Research Reactor
ORNL	Oak Ridge National Laboratory
PCI	Pellet Cladding Interaction
PCMI	Pellet Cladding Mechanical Interaction
PNNL	Pacific Northwest National Laboratory
PWR	Pressurized Water Reactor
QOI	Quantity Of Interest
RDFMG	Reactor Dynamic and Fuel Modeling Group
RAE	Radially Average Enthalpy
RIA	Reactivity Insertion Accident
RIP	Rod Internal Pressure
RMSE	Root Mean Square Error
SEM	Scanning Electron Microscopy
TCD	Thermal Conductivity Degradation
TDE	Total Deposited Energy
TEM	Transmission Electron Microscope
tFGR	Transient Fission Gas Release
TH	Thermal-Hydraulic
TREAT	Transient Reactor Test facility
V&V	Verification and Validation
WEC	Westinghouse Electric Company

CHAPTER 1 - Introduction

Background

Assuring the accuracy of a computational tool is one of the most important aspects of its use. In this assessment, the accuracy of the calculation as well as the accuracy of the physics modeled must both be considered. In this PhD research, the accuracy of the computational tool CTF is being assessed. Gaps in modeling capability are identified and addressed. Model improvements are proposed and implemented, and verification and validation studies are conducted to test the accuracy of the newly updated code. This research is focused on the development and improvement of the CTF capabilities for high burnup (HBU) nuclear fuel rods during steady state and transient operation.

Several transient scenarios are of consideration for Light Water Reactor (LWR) safety analysis, most prominently the loss of coolant accidents (LOCAs) and the reactivity insertion accidents (RIAs). For this work, the focus is on RIAs, specifically the effects of fission gas release (FGR) prior to and during the RIA and its' effect on fuel integrity. The simulation results from the proposed model improvements are compared to experimental data and to fuel performance calculations, notably FRAPCON [1] and FRAPTRAN [2].

CTF [3] is an advanced subchannel thermal-hydraulic (TH) code designed for core and fuel analysis of LWRs. CTF is based on the COBRA-TF (Coolant Boiling in Rod Array – Two Fluid) code which was initially developed in the 1980s at Pacific Northwest National Laboratory (PNNL) to model LOCA. CTF and its nuclear fuel rod solver CTFFuel are being jointly developed and maintained by the Reactor Dynamic and Fuel Modeling Group (RDFMG) at North Carolina State University (NCSU) and Oak Ridge National Laboratory (ORNL). The code was substantially improved through the U.S. Department Of Energy (DOE) Consortium for Advanced Simulation

of LWR (CASL) project. NCSU currently provides a unified and up-to-date version of CTF v4.2 supplemented with a verification and validation suite, application guidelines, and an automated test matrix. FRAPCON and FRAPTRAN are the steady state and transient fuel performance codes used by the U.S. Nuclear Regulatory Commission (NRC) to calculate the high-burnup response of light water reactor fuels. Both codes were originally developed by PNNL and serves as the reference for currently licensed nuclear reactors in the United States.

The motivation behind this research is presented, along with a brief overview of RIAs, the CTF computational tool, and the difficulty of high burnup fuel modeling. Following a literature review of relevant scientific papers and journal articles, the phenomena that occur within the nuclear fuel at high burnup are explained. A review of the current CTF capabilities is presented, as well as the gaps in the current modeling approaches. A review of current computational models for FGR and other code improvements is performed, and several models are proposed for implementation in CTF. A description of these implementations is included, and simulations are performed to verify model implementation and validate CTF capabilities for use in calculating high burnup high enrichment (HBHE) fuel simulations. An analysis of these results is provided, and conclusions are drawn from the results regarding model implementation and accuracy. Future work for the improvement of the CTF computational capabilities is explored and studies to determine are offered.

Motivation

To be licensed for operation by the U.S. NRC, a nuclear power plant must first be shown to be safe. To demonstrate this, tests are performed using computational tools that demonstrate a plant's safety given unique geometric, neutronic, and material (fuel, cladding, and support)

choices. The computational tools used for these tests are created to model the relevant physics as closely as possible.

The advancement of fuels for existing LWRs is primarily directed towards prolonging the fuel cycle duration from the current 12-month period to either an 18-month or 24-month cycle. This extension necessitates the adaptation of fuel rods to endure HBU and increased enrichment levels, prompting the development of HBHE fuel. This specialized fuel, engineered to endure such demanding conditions throughout the extended fuel cycle, necessitates thorough testing and simulation to assess its safety thresholds and stringent criteria must be met by the fuel during transient conditions to mitigate the risk of fuel damage or radioactive release. Computational tools are used to calculate fuel state and/or failure during and after transient events. It must be determined whether the computational tool is sufficient for HBHE fuel or be adapted to it if necessary.

During an RIA, a large reactivity incursion occurs in a short period of time. This rapid increase in reactivity will cause an ensuing increase in the fission rate and power in a fuel rod or assembly. This type of accident can occur globally across the core such as during an unintended decrease of the soluble boron concentration (Pressurized Water Reactors (PWR)) or locally as during a control rod drop (Boiling Water Reactors (BWR)) or ejection (PWRs). In both cases, the rapid power increase causes temperatures in the fuel to increase rapidly, threatening fuel integrity. The release of fission gases can cause rod over pressurization, leading to cladding ballooning or rupture. The threat to fuel integrity causes further complications in the core due to the concern for fuel fragmentation, relocation, and dispersal (FFRD). In addition to issues within the fuel, the temperature increase can cause a local boiling crisis where departure from nucleate boiling (DNB)

occurs. This can cause issues with reactor power fluctuations and further damage cladding integrity.

At higher burnups, these effects are further compounded by the added effect of high burnup fuel phenomena. As burnup increases, the thermal conductivity of the bulk fuel will decrease, limiting heat transfer in the fuel rod. In addition, changes to the fuel microstructure due to thermal effects and the high burnup structure (HBS) will affect FGR, the thermal conductivity degradation, pellet-cladding mechanical interaction (PCMI), and other fuel factors. The FGR is also affected by burnup, as a higher burnup usually means longer irradiation and more fission gases presence in the fuel. The effect of higher enrichment on the fuel appears to have less of an effect on the phenomena of interest but must still be considered to maintain future fuel enrichments within the CTF range of applicability.

CTF currently serves as a state-of-the-art subchannel analysis tool for LWRs. As the nuclear power industry moves towards higher burnups and enrichments in core loading patterns, the applicability of the CTF models must be verified and new models may need to be added to consider new phenomena because of the higher burnup or enrichments. These improvements target the fuel performance models in CTF, where the deficiencies in modeling ability are expected. Of particular concern are the transient fission gas release (tFGR) and the formation and effect of the HBS. These two phenomena, as well as others, can have a greater effect on fuel failure at higher burnups. This necessitates some type of treatment to maintain CTF's accuracy at higher burnups and higher enrichments. Background information on high burnup fuel performance phenomena is provided following a literature review of applicable documentation and articles.

CHAPTER 2 – High Burnup Fuel Behavior

Introduction

A variety of phenomena occur at higher burnups that are not present at low and medium burnup or affect the fuel differently at high burnup. A review of the current understanding of these phenomena is presented below. The review examines the occurrence of these phenomena as well as their effect on nuclear fuel performance during steady state and transient conditions. The HBS is investigated, as well as its effect on the bulk fuel thermal conductivity and FGR. The FGR is further investigated through its development and effects on the thermal conductivity and fuel rod internal pressure (RIP) as well as the relationship it has with HBS formation and development. The difference between FGR and tFGR is explained and their effects on fuel performance are quantified. Further phenomena such as fuel cracking and FFRD are also explored.

High Burnup Structures

During nuclear fission in nuclear fuels, atoms split and release free neutrons and fission products (FPs), both gaseous and solid. The neutrons continue to travel through space until they impact further particles, while the much larger gaseous and solid FPs attempt to reintegrate the crystal lattice found in uranium dioxide. However, this process is imperfect, and defects sometimes do not recombine, causing a buildup of defects that may further affect the lattice structure. In addition, several of these FPs are transuranic elements such as plutonium or neptunium that may be fissile or decay to fissile materials [4]. This causes an increase in the local fission density, causing a higher local burnup that can be two to three times that of the rod average burnup [5].

This behavior tends to be seen in the outer rim region of the fuel pellet, as there is a higher density of epithermal neutron resonance absorption in uranium-238. Due to this, there is often an

increased concentration of the fissile isotope plutonium-239 [6] [7]. While this increase in fission density could theoretically occur anywhere in the pellet [8], the neutron energy spectrum conducive to plutonium-239 formation in current uranium dioxide LWR fuel is focused in the rim region [9]. While most commercial fuel (and thus most research in the area) is done on ceramic uranium dioxide, tests using mixed oxide fuels have also shown the formation of this region where burnup and fission density conditions are optimal. Grain restructuring has also been reported in fast reactor mixed oxide, nitride, and carbide fuels [4]. For our purposes, we will focus on the formation of the HBS in ceramic uranium dioxide.

As a result of this increased burnup and the average operating temperature (less than 1173 K) [5] at that radial depth, the fuel matrix begins a restructuring process. At higher temperatures such as the temperatures at the center of the fuel rod, the possibility of annealing effectively negates the restructuring [10]. The process tends to begin at a burnup anywhere from 40-55 GWd/MTU [8], and some questions exist as to what exactly causes the change in grain size and distribution. The grain morphology in the HBS is characterized by decreased grain sizes and the redistribution of interstitial and fission gases to high pressure intragranular pores. The fuel grains in the HBS recrystallize to around 0.15 microns and the intragranular pores found are on the order of 1 to 2 microns [11]. Other studies characterize the grain subdivision as including grains with a size between 10 and 0.15 microns [12]. These values change depending on the initial conditions and power history, but are significantly different than the un-recrystallized grains, where grains start on the order of 5 to 10 microns [4].

Figure 1 shows the cross sectional ceramography of etched LWR pellets at a burnup of 65 GWD/MTU, well within the ranges of the fully developed structure. It is seen in Figure 1a that the unrestructured fuel taken at an intermediate region of the fuel, where the grain restructuring has

not taken place. The grains are larger, and planar defects are visible as dark features within the grains. Figure 1b shows the HBS at the pellet rim. Significantly smaller grains can be noticed in the intermediate region, as full restructuring of the grains has not occurred.

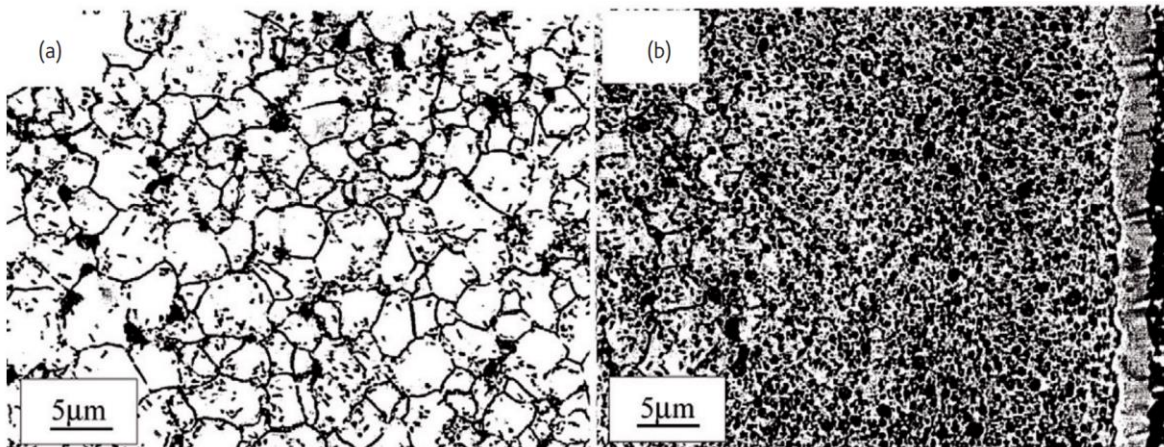


Figure 1: Ceramography of LWR rim regions at high burnup showing the fully developed high burnup structure [4]

The HBS is characterized not only by the smaller grain sizes smaller than 200-300 nm [10], but also by the larger number of intergranular pores. These pores contain highly pressurized fission gases that have congregated during the grain restructuring and can reach a porosity of up to 20%, though 10% is more common as the upper limit [13], particularly in the case where PCMI is present [8]. This is shown in Figure 2 below where the HBS effect on fuel porosity can be seen [14]. The HBS formation in ceramic uranium dioxide is thus characterized by sub-micron grain subdivisions with concentrations of fission gases in pores along grain boundaries.

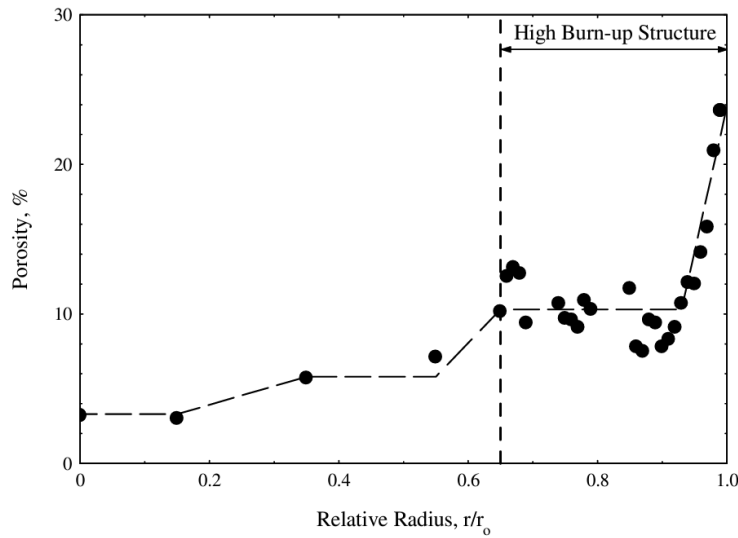


Figure 2: Radial porosity distribution in high burnup samples measure through optical microscopy [14]

There are several theories as to the formation of these smaller grains. The two main theories as to the primary formation mechanism of the HBS are recrystallization or polygonization [5]. In recrystallization, the subgrains are formed with spherical grains, the subgrains grow into recrystallization nuclei and the recrystallized grains finally grow. The dislocation nuclei are caused by the high grain angle boundaries where the fission gases precipitate on the recrystallized boundaries and link up in the grain growth of the recrystallized grains [13]. These findings were found in high burnup uranium dioxide fuels using transmission electron microscopy (TEM) to detect the recrystallization of the grains and electron probe microanalysis (EPMA) to identify the fission gas precipitation at grain boundaries, particularly that of xenon and krypton [14]. The diameter of the fission gas bubbles is also identified as on the order of nanometers as shown in Figure 3, which agrees with other studies from [4].

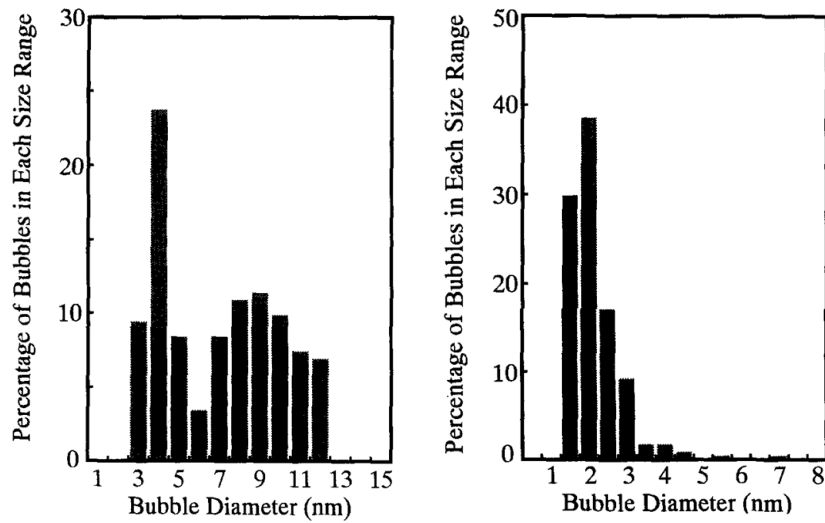


Figure 3: Fission gas bubble diameter prior (left) and post (right) to recrystallization of grains in high burnup fuel [13]

In polygonization, over pressurized fission gas bubbles cause non-uniform stress fields cause the formation of high-density dislocation walls that transform into new subgrain boundaries. As a result of the large dislocation density, the stress fields act as the driving force for dislocation movement. The dislocations that do not annihilate each other create walls that form low energy, imperfect sub boundaries between new subgrains [15]. While this work focuses mainly on the HBS modeling and open questions surrounding HBS formation, it also presents results from TEM, scanning electron microscopy (SEM), and high-resolution TEM (HRTEM). It has to be noted that there is much information missing in the analysis of HBS formation and that further experiments are needed to complete our understanding [15].

While high burnup fuels present challenges across all aspects of fuel performance and safety, the HBS adds extra difficulty in determining fuel integrity in a reactor. The change in fuel structure will change the fuel thermal conductivity and the radial temperature distribution when

compared to high burnup fuel with no HBS. In addition, the grain restructuring in the rim region poses PCMI concerns due to material swelling and stress interactions [16]. The high burnup fission gas pores that accumulate at grain boundaries also diffuse slowly during normal operation with no additional concern; however, in transient conditions such as LOCAs or RIAs may release a much larger quantity of gas and over pressurize the rod interior, causing cladding ballooning and blowout [17]. In addition, the HBS increases the risk and consequences of FFRD due to the grain restructuring. The FGR may exacerbate this further [7].

The main concern with grain restructuring is the change in thermal conductivity and other fuel thermal properties after recrystallization. In general, as burnup increases there is a noted decrease in the thermal conductivity of uranium dioxide fuel [14]. This is due to the accumulation of various defects in the lattice such as FPs, radiation damage defects, or any kind of heterogeneity such as bubbles or cracks [4]. This behavior is true for most crystal structures, as the impurities and defects slow the transfer of heat and lead to a net smaller heat transfer coefficient. As the HBS is further characterized by a larger concentration of fission gases accumulated at grain boundaries, it is expected that the transformed fuel has a lower thermal conductivity than untransformed fuel, as in general, gases have lower thermal conductivity than solids.

However, it is found that that this region of fuel has a higher thermal conductivity than if the recrystallization has not occurred [14]. This is since although the presence of fission gases accumulating at pores decreases the thermal conductivity in that region, the recrystallization process removes many the lattice defects present in the fuel and eliminates FPs from the bulk lattice, concentrating them in pores. This greatly increases the thermal conductivity of the solid in the HBS, resulting in a net higher thermal conductivity. This in turn increases the heat transfer to the coolant in a reactor and helps with the thermal efficiency of the system, a benefit rather than a

drawback. This behavior is shown in Figure 4, where the increases in thermal diffusivity as a function of local burnup is presented. At 100 GWd/MTU, it was found that the thermal diffusivity of the fuel increases by 50% [14].

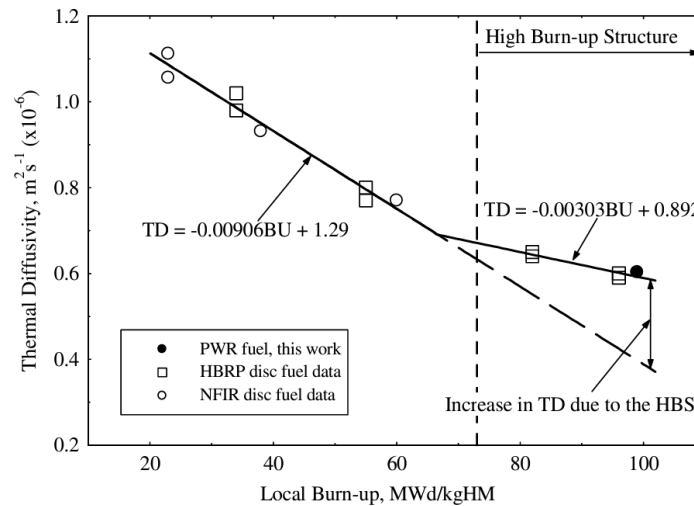


Figure 4: Influence of HBS on thermal diffusivity of high burnup uranium dioxide fuel [14]

A more significant concern with the HBS formation in nuclear fuel rods is the increased risk of pellet cladding interaction (PCI) and more specifically PCMI. In PCI, the chemical and material interactions between the pellet and the cladding following gap closure are of special interest for cladding integrity and fuel performance purposes. As conduction through solids, such as when the cladding is in contact with the fuel pellet, is more efficient than heat transfer through convection or gaseous contact, such as when the pellet and the cladding are not in contact, PCI generally results in better heat transfer and a higher thermal efficiency. At operating temperatures and intermediate and high burnup levels the pellet and clad can interact with each other, gradually becoming bonded [7] [8]. They interact with each other following fuel pellet swelling and cladding creep during irradiation. This type of interaction can further lead to PCMI, where stress forces

transfer between the cladding and pellet and vice versa. By itself PCMI can increase heat transfer through heat conduction rather than convection at the pellet cladding interface. However, in conjunction with other phenomena that cause large stresses, such as rapid thermal expansions or significant FGR, PCMI can serve as an aggravating factor for crack formation [17] in both the cladding and the fuel.

As the formation of the HBS is correlated with the formation of the subgrains described in the polygonization theory [15], this PCMI also affects the rate at which it may form. Studies conducted by the Electric Power Research Institute (EPRI) [7] have concluded that the HBS formation allows for a better formation of PCMI. However, in transient conditions, the stresses from the cladding can cause the fuel to fracture and crack, as ceramic uranium dioxide pellets are more brittle than metallic clad materials. In addition, the FGR can directly contribute to fragmentation of the fuel outer edge [8]. The hoop stress from the fuel pushing on the inside of the cladding can propagate through the HBS and PCI layer, causing cladding fracture at lower temperatures where cladding is less elastic [8, 18]. This fracture causes irreversible damage to the pellet, impacting fuel performance and in the event of cladding failure and thus causing more significant dispersal of fuel material.

The HBS causes additional difficulties with FFRD due to the changes in microstructure and grain sizes. In normal operating conditions, fuel cracking is relatively well understood. The roles that pellet thermal gradient, thermal expansion, and creep in crack nucleation and propagation have been observed and models exist to simulate these [6]. However, the phenomena and roles they play in transient operations are less well known, including crack propagation in the HBS. Reports from the U.S. NRC indicate that the HBS in the rim may fragment more easily if fission gases are released rapidly [19]. Indeed, we can see the effect of burnup and transient testing on the

fuel rod cross sections in Figure 5. It is noted that the darker grains in the medium burnup rods are the beginning of the HBS restructuring. In addition, the same source tested the FFRD risk for a high burnup rod of 90 GWd/MTU where the HBS was found in over a third of the fuel radius. In this transient test, a target temperature of 800 °C was achieved and cladding rupture with a large ballooning occurred. Figure 6 shows the fragmentation of the fuel pellet. It is noted that the rim structure portion of the fuel fragmented into both larger and micrometer sized holes. It appears the remaining fuel volume has a more robust grain structure, but conclusions were unable to be pulled given that the relocation and release of particles was significant [19].

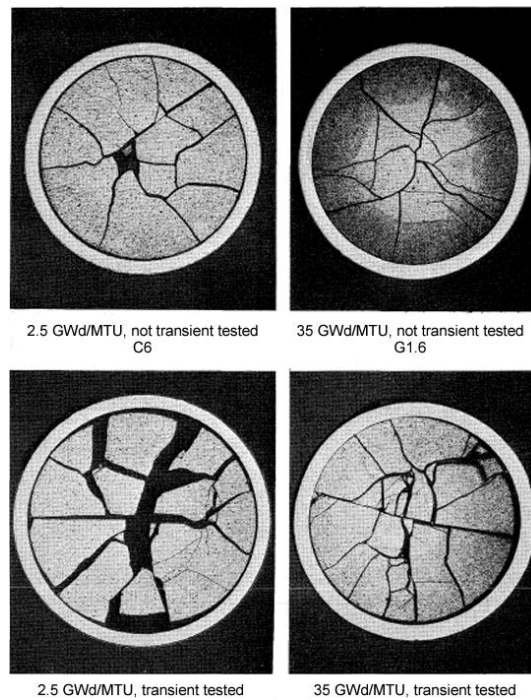


Figure 5: Pre (top) and Post (bottom) irradiation LOCA transient fuel fragmentation for low (left) and medium (right) burnup fuel rods [19]

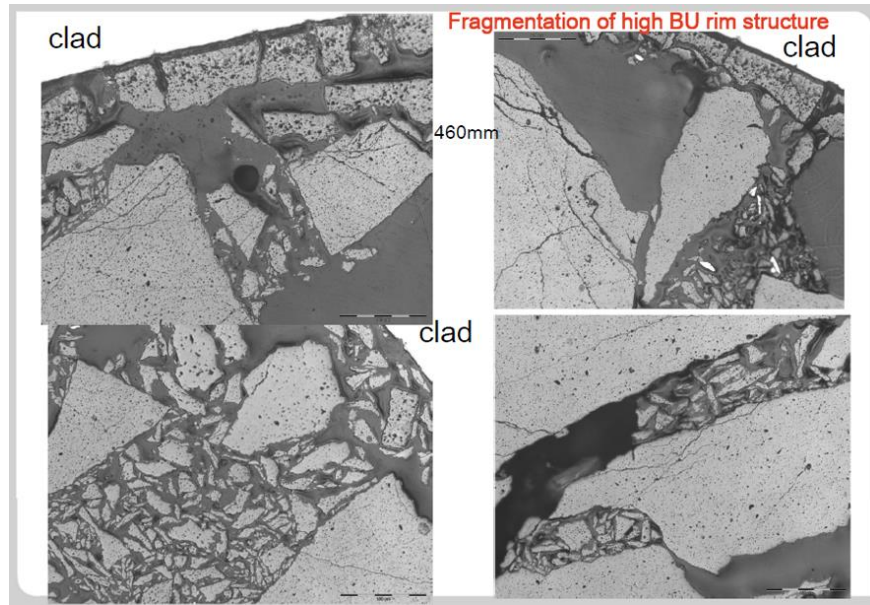


Figure 6: Fuel Fragmentation in HBS [19]

Another concern for fuel performance and fuel rod safety lies in the fission gas bubbles. In normal operation, fission gases are released from the grain structure through diffusive processes [20]. During normal operation, this does not pose a more significant concern than for non-restructured fuel, as the released is slow over time [21]. In transient or off normal operations however, the highly pressurized fission gas bubbles may crack the brittle fuel matrix and slip into the gap region of the fuel significantly quicker than in normal operation. The cracks may also be caused by the stress fields caused by PCMI. This release is more significant in transient conditions such as RIAs or LOCAs and may cause fuel failure via fragmentation or cladding damage through the form of ballooning or fracture.

Fission Gas Release

As the fissile materials in nuclear fuel undergo nuclear fission, various fission products are created. The distribution of the products varies in isotopes and forms and is strongly dependent on

the initial fissile species that split the energy of the neutron causing the fission process, but a general graph showing the distribution of fission products by mass for several fissile isotopes is shown in Figure 7. In current and planned fuel for LWRs, most of the nuclear fuel is made up of uranium-235 at fabrication and contains fractions of other transuranic isotopes because of irradiation in the reactor, particularly plutonium-239. The various fission gas atoms, particularly xenon and krypton [22], travel through the crystal lattice and eventually settle in several sinks, including pores and free surfaces. The free surfaces cause a release of the gaseous atoms to the fuel-pellet gap, and the inter and intra-granular pores will cause a variety of behaviors in the fuel that differs from fuel with no significant steady state release. Over time, these accumulations can cause strain within the fuel pellet and issues in the gap behavior but can globally be predicted within reasonable limits.

The most common gaseous fission products for uranium-235 based fuel are xenon and krypton [22], as can be determined by post-irradiation analysis from sources available by the same authors. In Figure 7, the peaks in fission product yields by mass are found between 90 and 100 amu and 130 and 140 amu. As krypton has an atomic mass of 83.798 amu and xenon an atomic mass of 131.293 amu [23], they are among the most common products following fission. These gases form and settle in the fuel crystal lattice, but do not remain static. Both xenon and krypton will form preferentially in vacancies in the uranium dioxide lattice, especially in the uranium (fluoride-type) sublattice; though as krypton is a smaller sized atom it has a greater likelihood compared to xenon of settling in the oxygen vacancies over the uranium vacancies. While both interstitial and vacancy diffusion are possible, the larger sizes of both atoms and in xenon's case, a high thermal state following fission, tend to facilitate vacancy diffusion over interstitial diffusion [20].

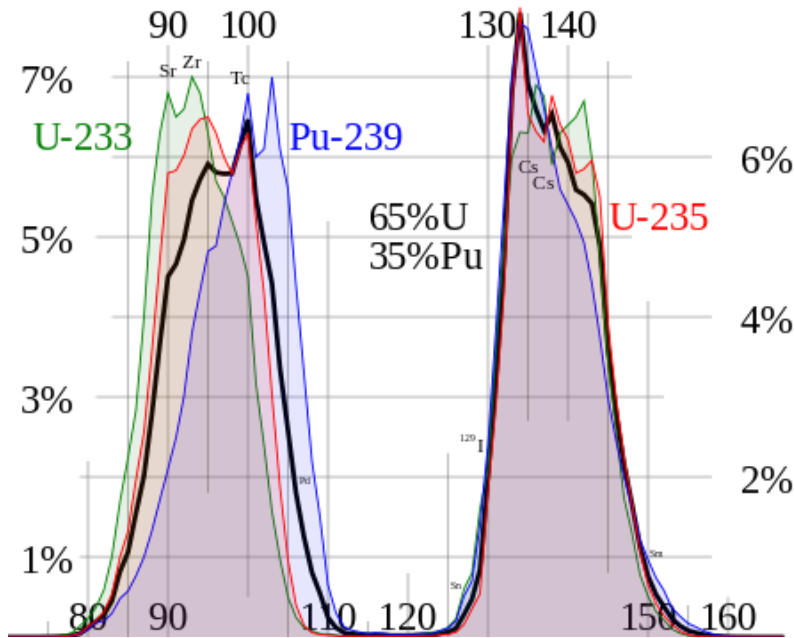


Figure 7: Fission product yield by mass [24]

Following the formation of the atoms following nuclear fission, the gases will begin to diffuse throughout the fuel. On the crystal lattice level within the fuel microstructure, the individual atoms tend to diffuse towards lattice defects. On the fuel microstructure scale, the defects translate to be radiation or thermally induced intra-granular defects or grain boundary defects. As the atoms diffuse towards defects, they congregate and form small gas pockets. These bubbles, on the order of 2 nanometers [21], will continue to grow unless destroyed by one of two manners. The bubbles may re-resolve back into the bulk fuel matrix due to changing thermal conditions or may be impacted by high-energy fission fractions following nucleation on the lattice defect. The bubbles formed will continue to grow and move with temperature through an increased thermal diffusion rate and with burnup through a larger production of fission gases. A higher concentration of intra-granular bubbles is expected at and near grain boundaries due to the higher number of lattice vacancies that exist near grain boundaries. The bubbles on the grain boundaries

are considered fixed as grain boundary diffusion is not a significant transport mechanism during normal conditions [25].

The movement of intra-granular bubbles is simpler than grain boundary bubbles. The diffusion speed of intra-granular bubbles is closely tied to the temperature and fuel structure. Below 800°C, the movement of the intra-granular bubbles is rather limited. Above 800°C, the intra-granular bubbles diffuse more rapidly to the grain boundaries [26]. The grain boundary bubble kinetic behavior is more complicated and depends on both the temperature and fuel structure but also considers other factors. Less knowledge exists about grain boundary (inter-granular) diffusion process than the intra-granular diffusion process.

FGR as diffusion in nuclear fuel has three broad steps. After the individual gas atoms are formed and diffuse through the bulk material, they congregate at radiation defects and form bubbles. After bubble formation on grain boundaries, the bubbles grow and eventually connect to the rod free surface. The current understanding of bubble mechanics is limited here, and several theories exist for bubble growth. Regardless of the underlying mechanism for bubble growth, several facts are accepted as part of this process. The bubbles nucleate on grain faces and grow through absorption of gas atoms found in the surrounding fuel matrix. At a certain point, the bubbles will grow enough to begin to connect with each other. Following bubble connections on grain surfaces, often denoted grain boundary tunnels, the connection process occurs at so called grain boundary triple junctions [27]. These triple junctions occur at the intersection of three or more grains. This creates a quicker escape route for grain boundary fission gases than direct connections between two grains [20]. This behavior is shown in Figure 8. Research into the formation and saturation rates of grain triple junctions is ongoing to better model this behavior.

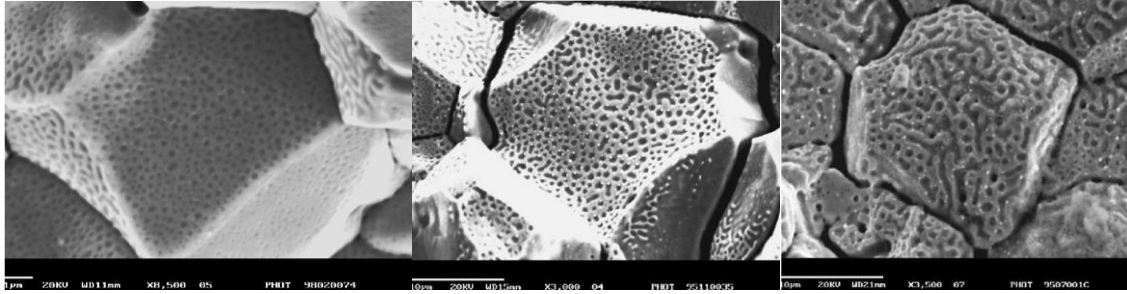


Figure 8: Formation and growth of grain boundary bubbles

(In the left window, the initial formation of bubbles on the grain surface is seen. In the middle window, the connection of these bubbles to form “cigar shaped” bubbles are present; the space between the fuel grains is also more apparent. In the right window, the formation of grain boundary tunnels is noticed. Examining the corners of the grain boundary, triple junctions where multiple grain tunnels connect can be seen [28].)

In short, the fission gas bubbles converge into intra-granular bubbles and grain boundaries following their formation. Eventually, most gases during normal reactor operation and at standard operating temperatures will converge to grain boundaries, where they coalesce into inter-granular bubbles. These will eventually connect to one another, forming cigar-shaped bubbles. These grain boundary tunnels stretch throughout the fuel until they reach a free surface. However, to release from the matrix, a saturation condition must be reached. This condition is also the subject of debate, with some papers attributing a constant concentration [29] and others preferring a calculated saturation [30] based on fuel conditions. Once saturation conditions are met, the trapped fission gases are released from the nucleation sites.

The three steps of FGR—gas atom diffusion, bubble formation and growth, and release—are dependent on several factors at the location of occurrence. There is a significant dependence of the FGR process on temperature, grain size, burnup, fission rate, and fuel stoichiometry.

Elevated temperatures to increase FGR as it accelerates the atomic diffusion process, as well as in some models playing a factor in the release saturation. The grain size is strongly correlated with the rate at which atoms diffuse through the grains and accumulate at the boundaries. The grain size is determined by the initial grain size following fabrication, as well as the temperature and pressure in the fuel matrix, and can vary significantly over the course of the reactor operation. The fission rate is directly correlated with fission gas production, though an increase in fission rate that increases FGR can potentially be mitigated by the re-resolution of gases following fission fragment impact on gas bubbles. The fuel stoichiometry, as well as enrichment, will have a strong effect on the diffusion process through the calculation of the diffusion coefficients used in the reaction. Due to these factors, fission gas production and accumulation is hard to predict, and there is no complete understanding of the release process and conditions for current LWR fuel. The interactions that the FGR process with other phenomena occurring both at low and high burnup are also complicated, particularly when it comes to the HBS and PCMI. However, the effect of FGR on fuel rod performance is well documented.

Prior to release, the presence of the gas bubbles will also cause a change in material properties, as the stoichiometry of the fuel is no longer the same as fabricated. Numerous studies have documented the degradation caused by xenon on uranium dioxide thermal conductivity and this effect is also considered by various governmental agencies [31]. This will be investigated further. The build-up of fission gases also causes irradiation induced swelling of the fuel pellet [32]. This is due to the significantly smaller density of gaseous fission products when compared to fuel materials, particularly uranium dioxide.

The presence of these fission gas atoms in the fuel microstructure changes the bulk material properties. The change in the fuel lattice due to the presence of interstitial atoms and vacancies

following fission changes diffusion coefficients, density, thermal conductivity, yield stress, and most other properties but the most significant in modeling the fuel performance is the change in ductility and thermal conductivity. As the fuel microstructure is damaged by radiation and the presence of these fission gas atoms, the ductility of the uranium dioxide will decrease, and the material can become more prone to cracking. This effect is further compounded by the thermal swelling of the gas bubbles in the matrix, as the gases have a greater thermal expansion coefficient than the bulk fuel material. The damage combined with the thermal swelling can increase the likelihood of cracks forming in the fuel pellet and increase the effect of PCMI [33].

When FGR does occur, a quantity of high-pressure gas bubbles connects to the rod fuel surface. This release adds to the quantity of gas atoms in the rod free volume, comprised of the pellet cladding gap and the fuel rod plenum, while adding a negligible increase in volume. This increases the pressure in the rod free volume. It also changes the composition of the free volume in accordance with the ideal gas law. When fabricated, most fuel rods utilize a fill gas of either argon or helium [34] due to their inertness. With the addition of the xenon and krypton fission gases, the material properties of the gap will change. This will change the thermodynamics of the gap, changing the radial temperature distributions in the gap over time. In addition, the increase in pressure because of the added gas inventory will force the gap to increase as more gas is added. This can lead to reduced heat transfer through the gap region, or in extreme cases to cladding ballooning and rupture, as shown in Figure 9 below. All these can lead to an increased risk of cladding failure.

Another method of release that can occur during steady state operation is with the development of cracks in the bulk fuel material. During normal operation, cracks due to thermal and irradiation induced expansion may develop in the fuel pellet [18]. These cracks develop prior

to any geometric effects from creep or swelling and are a result of the increase in power in the fuel pellet. Further pellet expansion and cracking can take place after temperature ramps. The main effects of these cracks on the fuel are the difference in heat transfer mode (from conduction through a solid to conduction through an interface with gas surrounding it) and an increase in rod free surface for FGR purposes. The increase in surface area allows more locations for the gases to escape to the rod free volume.

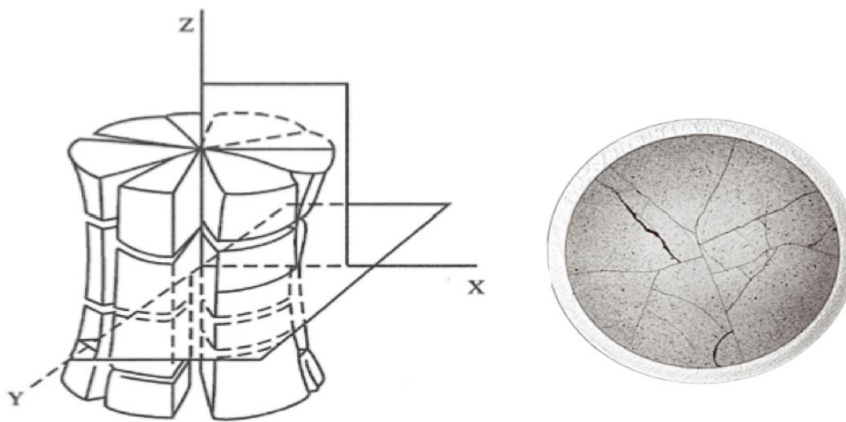


Figure 9: Cracking of LWR fuel pellet [18]

(On the left the “bamboo” or “hourglass” shape due to thermal stresses is seen. On the right a schematic of a cracked PWR pellet is provided [18].)

In addition to the direct consequences of FGR, several other phenomena exist that can exacerbate the steady state FGR. As discussed in this work prior, the HBS is a region of recrystallized fuel grains that is characterized by smaller grain sizes and multiple high pressure gas pores on grain boundaries. Due to the higher number of lattice vacancies (from the smaller grain size) in the HBS and the affinity of lattice defects to become bubble nucleation sites [13], the recrystallized zone tends to retain more gaseous fission products in high pressure coarse bubbles

(on the order of 1-2 microns) than the uncrystallized zone [11]. These are connected via grain boundary tunnels, sized in the order of nanometers. Where the HBS is not present, the fission gases are spread throughout the fuel rod albeit with a higher concentration far from the fuel center. This is due to the thermal gradient allowing for faster diffusion of gaseous atoms and smaller bubbles from the center of the rod, while larger bubbles remain immobile. This combined with the higher concentration of vacancies in the pellet edge in the HBS traps the fission gases in the coarse grain boundary bubbles on the pellet edge. The effect of other phenomena on FGR will be introduced when those are detailed further in this work.

The diffusion-based process is dominant during steady state operations due to the time it takes for changes in gas concentrations to occur. It is the most common type of FGR found in fuel rods in LWRs, and FGR release values for PWRs tend to fall between 5-20% of available inventory for fuel rods undergoing no significant transients [32]. The FGR can cause issues with rod over pressurization and changes in the gap composition, leading to changes in thermophysical properties. The release can also cause fuel failure through cladding rupture following over pressurization, though this issue is less common in normal operation. Several phenomena occur that can affect the amount and severity of FGR during normal operation. These are explored following an investigation of transient FGR, as seen during off-normal operations.

Transient Fission Gas Release

The behavior of fission gases under steady state conditions differs significantly from that under transient conditions, primarily due to the differing release mechanisms involved. In steady state scenarios, gas release is governed by diffusion, a gradual process that requires extended periods to release substantial quantities of gas. Although high burnups introduce complexities such as HBS and PCMI, diffusion remains the primary mode of gas transport. In contrast, transient

conditions—regardless of their specific nature—are characterized by a rapid, non-diffusion-based burst release that can expel a large fraction of the fission gas inventory within a short timeframe.

The prevailing consensus is that this burst release mechanism is driven by the formation of micro-cracks, both along grain boundaries and within the grains themselves [35]. Supporting evidence from various studies [36] suggests that these rapid gas releases are triggered by temperature fluctuations, leading to swift kinetics. Burst release is less likely at lower temperatures, with the release rate being influenced by the temperature range of the transient. It is also hypothesized that there is an optimal temperature at which gas release is maximized [36]. This type of cracking following thermal changes is noted during normal operation [18], but the magnitude and speed at which the temperature change occurs is key in transient micro-cracks.

During transient conditions, micro-cracking in the fuel's microstructure is induced by thermal swelling and the stresses arising from cladding interaction and irradiation damage. This swelling increases thermal stress beyond the material's yield point, resulting in plastic deformation and crack formation. These micro-cracks lead to a rapid release of gas due to the exposure of more fuel surface area to the rod free volume. This simultaneously releases trapped gases and reduces the storage capacity of the affected grains [36]. During burst release events, fission gas is rapidly expelled from both the grain boundaries and, to some extent, from intra-granular bubbles. Collecting data on transient burst releases is challenging due to the rapidity of the transient, particularly for high burnup fuel rods, making this phenomenon less understood compared to steady state FGR.

Like steady state FGR, transient FGR is significantly influenced by the fuel rod's burnup level. As burnup increases, the distribution of fission gases within the fuel rod changes, as discussed in the context of steady state release. The development of the HBS results in a higher

concentration of fission gases near the pellet's periphery in high-pressure bubbles. Although these peripheral gases have minimal impact during diffusion, they represent a substantial inventory available for burst release during transients. The high-pressure pores at the pellet's rim provide favorable sites for crack propagation, leading to increased gas release when the HBS is present. Research has shown that the transient FGR in fuel with a well-developed HBS is closely linked to the gas retained in the rim bubbles [16]. This suggests that a significant portion of the gas released during transient FGR is trapped within the HBS. In addition, at higher burnup the gas inventory for release is much larger than at lower burnup. This increases the risk of cladding rupture following a transient event, as shown in Figure 10.

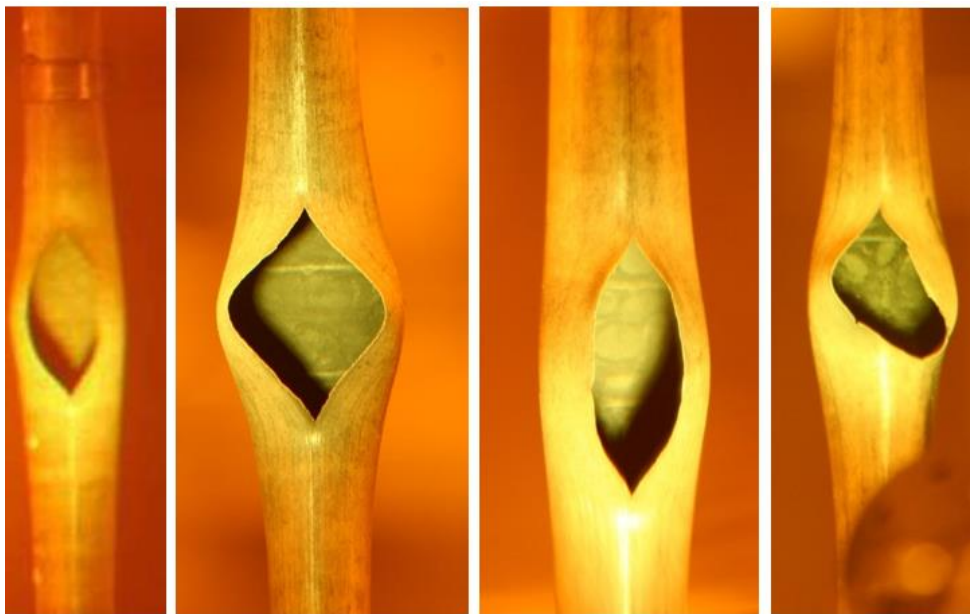


Figure 10: Cladding rupture and ballooning following transient fission gas release [37]

Contrary to steady state FGR, PCMI exerts a considerable influence on the transient release mechanism. Regardless of the HBS development status, PCMI tends to suppress gas release by applying external pressure on the fission gas bubbles within the fuel structure. Increased external

pressure reduces tFGR in both the HBS and the bulk pellet lattice [16]. Thus, PCMI is expected to decrease tFGR by inhibiting HBS formation and exerting an opposing force on fission gas bubbles within the bulk fuel material. The transfer of stress between the pellet and cladding also helps mitigate cracking in the pellet, potentially diminishing the burst release effect in transient tFGR. This and other phenomena are considered in conjunction with both steady state and transient FGR and the complex interactions between high burnup fuel phenomena and FGR are investigated.

Other Phenomena in High Burnup Nuclear Fuel

Several phenomena exist that have a significant effect on the occurrence and severity of both steady state and transient FGR. Some have been already mentioned in passing in the previous section and will be fully explained and others are introduced hereafter and their effect on FGR explored. These include fuel geometrical changes such as fuel cracking, FFRD, thermal conductivity degradation, PCMI and PCI. The effect that these have on the FGR as well as how FGR may impact them is investigated.

As cracks occur in the fuel, both thermally induced and irradiation induced, they cause irreparable damage to the fuel pellet. The ceramic fuel pellet will begin to fragment and separate into separate pieces held together by the cladding [19]. This behavior is shown visually in Figure 5 and in Figure 6. The fragmentation is caused by the stress in the fuel pellet exceeding the yield strength of the material at temperature. The yield strength is further affected by the material composition and microstructure. This changes over time due to irradiation and fission product formation and the moment at which fuel may fracture is difficult to determine. Once fractured, the main effect during operation is a reduced heat transfer and greater ease of release for FGR due to the increased fuel surface area. Following fracture, the fuel may relocate to an area other than the as built location. This change can occur radially and axially but is of greater concern axially [19].

In case of cladding rupture, the possibility of fuel dispersing and escaping the closed fuel rod is of vital importance for reactor safety reasons.

FFRD is a key consideration when assessing fuel failure in the reactor core. Given the nature of RIAs and the heightened risk of cladding failure, minimizing FFRD is critical to reducing the severity of radiation leakage into the primary coolant. FFRD encompasses a wide range of potential fuel movements and fractures, including fine fuel fragmentation and axial and radial relocation within the fuel pin. It also includes mobile fuel, which refers to fuel that has separated from the fuel compact and has not yet relocated. According to a study by the U.S. NRC, under LOCA conditions, fine fragmentation is confined to fuel regions with a pellet average burnup exceeding 55 GWD/MTU [38], and axial relocation is limited by a cladding strain greater than 3%. This fine fragmentation is more severe and intense than the cracking and fragmenting observed during normal operations [38].

Additionally, Bales, Chung, Corson, & Kyriazidis [38] highlight the impact of tFGR on cladding rupture, specifically regarding the size of the burst and the extent of fuel fragmentation. They provide several models for predicting the mass of dispersed fuel, emphasizing that the accuracy of these models is tied to the precision of the cladding's axial strain measurement. Other sources [6] identify fine fuel fragmentation as occurring at 68 GWD/MTU, with a higher frequency above 72 GWD/MTU. Fragmentation that takes place before this burnup level is generally attributed to normal operational effects rather than burnup itself. FFRD poses the greatest risk to fuel failure through FGR from fractured grain boundaries. Although this project does not cover all aspects of FFRD, it is essential to acknowledge that an increased risk of FFRD significantly heightens the severity of rod bursts, as it leads to the release of fuel material into the primary coolant.

The role that FGR plays in FFRD is twofold. The presence of the fission gas bubbles decreases the strength of the material and increases the possibility and severity of fragmentation [33]. At high burnup and with the presence of the HBS, the size of the fragments is smaller, further allowing more potential for relocation within the fuel rod. The second role that FGR plays in FFRD is in the increased potential for cladding rupture due to over pressurization. This increases the risk of fuel dispersion in the primary coolant. Figure 11 shows an image of cladding rupture and fuel relocation from Halden IFA tests [19]. In Figure 12, we see examples of fuel fragmentation at the axial level at which rupture occurs. Gravity has pulled fragmented portions of pellets at a higher elevation to fill the gaps created by the fragmentation.



Figure 11: Ballooned region of cladding with relocation of fuel present [19]



Figure 12: Fragmented fuel at rupture plane [19]

As noted, as burnup increases there are concerns with thermal conductivity degradation in the fuel pellet. This is due to the irradiation damage to the fuel lattice and the build-up of fission products in the fuel. While it can be difficult to separate the effects of the fission gasses from other changes such as the buildup of transuranic elements and other fission products, it is known that the presence of gases is expected to cause a decrease in fuel thermal conductivity due to a stronger phonon-scattering effect [39]. The phonon-scattering is also strengthened by the buildup of point defects in the fuel matrix as the grains restructure [14]. This is further compounded at high burnup when the gases have had time to accumulate and leads to higher temperatures in the fuel pellet, increasing the risk of melting or worsening thermal expansion and other harmful phenomena [36].

However, as noted prior, the formation of the HBS can negate this degradation effect due to the removal of fission gas atoms and the reduction of defects from the smaller grain size [40] [41]. In addition, Reference [14] note that the thermal annealing of the fuel pellet will cause a

recovery of the fuel thermal conductivity to a certain extent. Thermal annealing at lower temperatures removes point defects in the lattice and higher temperature annealing will cause the removal of solid solution fission product atoms in the crystal lattice [14]. The net effect of high burnup on thermal conductivity can thus vary based on radial position on the fuel rod history, making it difficult to draw general conclusions regarding the degradation.

As the fuel pellet expands due to thermal and irradiation induced swelling, contact may occur between the cladding and the fuel pellet. Even in cases where contact does not occur, interaction between the pellet and cladding may exist and affect the FGR. PCMI and PCI do not appear to have a significant effect on the steady state FGR process. The largest recording effect is the potential for accelerating or slowing down release at the fuel pellet edge [16]. Unlike in steady state Fission Gas Release (FGR), Pellet-Cladding Mechanical Interaction (PCMI) plays a significant role in influencing gas release during transient conditions. Regardless of whether the High Burnup Structure (HBS) is fully developed, PCMI typically suppresses gas release by exerting external pressure on the fission gas bubbles within the fuel. This additional pressure reduces the release of fission gases from both the HBS and the main fuel pellet lattice [16]. Consequently, PCMI is expected to lower FGR by both hindering the formation of the HBS and counteracting the release of fission gases within the bulk fuel material.

The fuel melting temperature is significantly affected by the fuel burnup. Research indicates that as burnup increases to 50 GWD/MTU, the fuel's solidus melting temperature can drop by as much as 100°C [8]. Fuel melting is considered to occur when either the fuel centerline or the hottest part of the rod reaches or surpasses the solidus melting temperature under the given conditions [42]. An example threshold is shown in Figure 13 below, where the dotted lines

illustrate a 30 K uncertainty in predicting the fuel's melting point [8]. At high burnup levels, the U. S. NRC considers that the fuel temperature remains the most critical limiting factor [42].

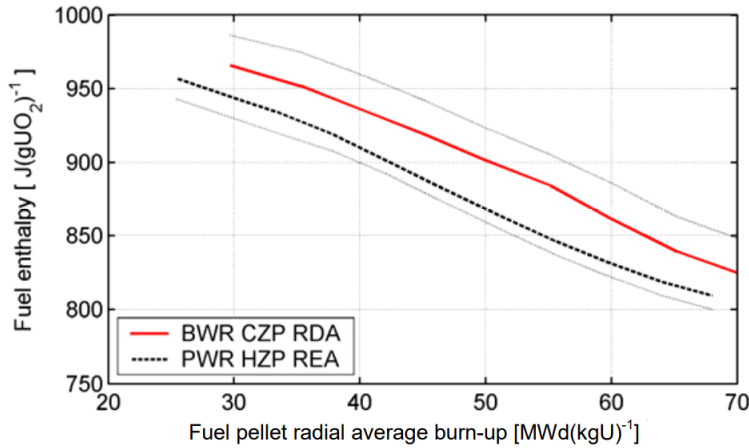


Figure 13: Estimate Thresholds for UO₂ fuel pellet melting under BWR CZP RDA and PWR HZP REA [8]

In short, several phenomena of interest for high burnup fuel calculations are investigated. The HBS is reviewed and its' effects on fuel performance are considered, particularly with regard to FGR. FGR is also quantified and the difference between steady state and transient FGR is considered. Other phenomena of interest such as FFRD, PCMI, thermal conductivity degradation, and fuel cracking are investigated. Again, particular attention is given to these regarding FGR. These phenomena are then compared to the modeling capabilities of CTF.

CHAPTER 3 – Review of Current CTF Capabilities

Introduction

Following an in-depth literature review of fuel performance phenomena and their effect on nuclear reactor fuel, the CTF computational tool is introduced. The codes' current capabilities are explained, and existing models are provided with equations and sources. An analysis of the gaps in the codes modeling capabilities is provided as well.

CTF is a sophisticated computational tool designed to assess the behavior of nuclear reactor cores. As mentioned before, it is based on the COBRA-TF code, which was initially developed in 1980 by PNNL under the sponsorship of the U.S. NRC as a thermal-hydraulic (TH) analysis code for analysis of fuel rod bundles. Over the decades, it has been continuously updated and enhanced. CTF employs a two-fluid, three-field modeling approach, accounting for three distinct, independent flow fields: fluid film, vapor, and liquid droplets. The code integrates a comprehensive range of TH models that are essential for accurate safety analysis of LWRs. These models encompass flow regime-dependent two-phase heat transfer, inter-phase heat transfer and drag, droplet breakup, and quench-front tracking.

With full three-dimensional capabilities and extensive suite of reactor thermal-hydraulic modeling features, CTF is extensively used for simulating LWR rod-bundle transient behavior in PWRs [3]. CTF has undergone an extensive verification and validation (V&V) process [43], including better mixing and void drift models, better numerical schemes, and better documentation. CTF further contains an independent fuel performance module, CTFFuel. CTFFuel is normally run as a part of CTF simulations for nuclear fuel rods but can also be run independently as a fuel performance code using set boundary conditions at the cladding. This module has enhanced fuel models when compared to other sub channel TH codes and attempts to

better model behavior within the cladding. As a TH code, CTF does not attempt to replicate a dedicated fuel performance code's performance; rather it is desired that reasonable estimates of quantities of interest are calculated by CTF.

The current modeling capabilities of CTF are reviewed. Modeling options are presented and considered for use in high burnup calculations for this project. Moreover, gaps in the modeling capabilities of CTF are also considered. Following the identification of the modeling needs for CTF at high burnup, models are proposed to help fill those gaps. Much of this information is sourced from the CTF Theory Manual, but some is sourced directly from the CTF source code and confirmed from supporting documentation.

Available Models in CTF

With regards to modeling high burnup fuel performance, there are certain quantities of interest that need to be considered. For fuel performance, the most important quantities necessary are the temperature gradient within fuel rods, the stresses and strains in the cladding and fuel, and fuel rod internal pressure. Using this information, the fuel performance can be evaluated accordingly to U.S. NRC methodology to operate a reactor in a safe manner. Accurate modeling of these quantities and the physics that affect them are of paramount importance for CTF to be considered a valid code for use of fuel performance modeling. The current capabilities of CTF for fuel performance can be split between the three major categories described above. For phenomena that affect multiple categories, for example creep affecting cladding strain and thermal gradients due to geometric changes, their effect is described in both categories.

The non-fluid temperature gradient in CTF is calculated using the general heat conduction equation found below (Equation 1). This approach splits a solid object into mesh cells to allow for treatment of temperature and space dependent material properties, unequal mesh sizes, as well as

variations in the heat generation rates and non-solid gaps (particularly between the fuel and cladding). This allows the system to be more variable and accounts for a variety of geometries and changing properties.

$$\frac{d}{dt} \int_V \rho C_p VT = \oint_A n_k Q_k dA + \int_V Q'' dV - \oint_A Q_s dA \quad \text{EQ 1}$$

The left-hand-side term is the transient term, that accounts for changes in density (ρ), material specific heat (C_p), temperature, and volume over time, where t is the timestep size. The right-hand side terms are the unit cell energy conduction term, heat generation term, and the convective heat transfer term. The first term represents the energy conduction in axial, radial, and azimuthal directions where n is the orthogonal unit vector, k is the current surface, and A is the surface area of the solid cell. The second term represents the heat generated due to fission within the mesh cell, where Q'' is the volumetric heat generation rate and V the cell volume. The third term only applies to mesh cells in contact with fluid cells and describes the convective heat transfer to the cooling fluid from the solid. The solution is kept explicit in the azimuthal and axial directions and implicit in the radial direction. In addition, the solid modeling capabilities in CTF include features for changes in heat transfer capabilities due to rod geometry changes and pellet cracking and sintering. Options exist in CTF to reduce this equation to calculate heat conduction only in the radial direction as well as an option to calculate heat conduction radially and axially without the azimuthal component.

The formulas for cladding hoop stress, axial stress, hoop strain, and axial strain are shown below in Equations 2÷7. In these equations $E(Pa)$ refers to Young's modulus and the shear modulus depending on whether the axial or hoop stress is calculated. This approach is the same approach

used by fuel performance codes such as FRAPCON, although the CTF approach includes certain assumptions not used in FRAPCON [44]. The remaining terms are defined below the equations.

$$\Delta r_{th} = \sum_{i=1}^{N_{radial}} \epsilon_{fuel} (T_{ij}) \Delta r_i \quad \text{EQ 2}$$

$$\Delta l_{th} = \sum_{i=1}^{N_{axial}} \epsilon_{fuel} (\bar{T}_i) \Delta \bar{r}_i \quad \text{EQ 3}$$

$$\sigma_{\theta} = \frac{r_i P_i - r_o P_o}{t_c} \quad \text{EQ 4}$$

$$\sigma_Z = \frac{\pi r_i^2 P_i - \pi r_o^2 P_o}{\pi (r_o^2 - r_i^2)} \quad \text{EQ 5}$$

$$\epsilon_{\theta} = \frac{\sigma_{\theta} - \nu \sigma_Z}{E} \quad \text{EQ 6}$$

$$\epsilon_Z = \frac{\sigma_Z - \nu \sigma_{\theta}}{E} \quad \text{EQ 7}$$

The terms defined are as follows:

t_c = Cladding thickness (*ft*)

r_o = Cladding outer radius (*ft*)

r_i = Cladding inner radius (*ft*)

P_o = Outer (system) pressure (*Psia*)

P_i = Rod internal pressure (*Psia*)

The RIP calculation in CTF is performed in one of two ways, depending on whether the pellet-cladding gap is closed or opened. This determination is discussed further below when addressing the dynamic gap conductance modeling. When the gap is open, the RIP calculated is the pressure of the gas within the cladding. This gas is calculated using a static lumped pressure model that is also used in the FRAPCON and GAPCON fuel performance codes. The pressure is assumed to be uniform throughout the fuel rod and no changes in gas inventory are permitted, even

in the case of fission product release. The equation for gas pressure is shown below in Equation 8. In the case where the gap is closed, the rod internal pressure is the contact pressure between the fuel pellet and the clad. Gap closure is caused in CTF by the calculated gap thickness being less than 1.8 times the sum of the surface roughness of the pellet and clad. The equation for rod internal pressure in a closed gap is shown below in Equation 9.

$$P_g = \frac{MR}{\frac{V_p}{T_p} + \sum_{j=1}^N \pi \Delta X_j \left[\frac{r_{ci}^2 - r_{fo}^2}{T_g} + \frac{r_v^2}{T_v} + \frac{r_{fo}^2 - r_f^2}{T_f} \right]} \quad \text{EQ 8}$$

The terms defined are as follows:

M = Gram-moles of gas in the fuel rod

R = Universal gas constant $\left(6.1313 \frac{ft \cdot lbm}{g \cdot mol \cdot K}\right)$

V_p = Gas plenum volume (ft^3) with expansion effects included

T_p = Gas plenum temperature (K) (defined as the outlet fluid temperature plus 10 K)

ΔX_j = Computational cell height at axial level j (ft)

r_{ci} = Cladding inside radius (ft) including expansion effects

r_{fo} = Fuel outside radius (ft) including thermal expansion and relocation effects

r_f = Fuel outside radius (ft) considering thermal expansion only

r_v = Radius of the central void in the fuel (ft) (User input)

T_g = Gas gap temperature (K)

T_v = Temperature of the fuel central void (K)

T_f = Average fuel pellet temperature (K)

$$P_{int} = \frac{\Delta r_{clad} E t_c (r_o^2 - r_i^2)}{\bar{r} [r_i (r_o^2 - r_i^2) - r_i^2 t_c v]} + P_o \frac{r_o (r_o^2 - r_i^2) - r_o t_c v}{r_i (r_o^2 - r_i^2) - r_i t_c v} \quad \text{EQ 9}$$

The terms defined are as follows, where the cladding dimensions do not account for previously calculated elastic and thermal expansion:

Δr_{clad} = Cladding radial displacement (ft)

E = Young's Modulus (Pa)
 t_c = Cladding thickness (ft)
 r_o = Cladding outer radius (ft)
 r_i = Cladding inner radius (ft)
 \bar{r} = Cladding mean radius (ft)
 ν = Poisson's Ratio (*Unitless*)
 P_o = System pressure ($psia$)

An important factor in the calculation of fuel performance (for all three quantities of interest) is the material properties used by the code. Material properties for nuclear materials are the subject of much ongoing research, particularly with regards to high burnup due to the difficulty in obtaining data during reactor operation. A general expression concerning models is that a model is only as good as its input. To have effective high burn up models, the model must be accurately informed. High burnup and long-term depletion fundamentally change the composition of the fuel and as a result, the material properties. Some of the changes are discussed below, but as a note the obtention of these material properties is particularly difficult, as very sensors or instruments can survive the harsh environment found in irradiated fuel.

As the burn up changes, the grain microstructure is strongly affected. As mentioned prior, HBS may develop at sufficiently high burnups but even at moderate burnups, the fuel grains can shrink. This reduction in grain size through the fuel lifespan will cause fundamental changes in pellet material properties. The effect of those changes causes long term changes throughout the fuel's lifespan and is of significance especially during transient conditions at the higher burnups, as the severity of a transient may be higher because of the changed material properties. The modeling of these microstructural changes is usually reserved for high fidelity fuel performance codes, as it is computationally intense to model the fuel microstructure; however, these strongly

affect the temperature gradient, stresses and strains, and the rod internal pressure. In CTF, the changes in material properties are considered by selection of the material property tables from the input. Available in CTF are several correlations for multiple properties, such as thermal conductivity and other material properties. A list of available material properties is included in Table 1 below, but most are taken or include an option from the MATPRO-11 material properties calculations. As a note, solid fuel enthalpy for built-in materials is calculated from the specific heat capacity using the relationship shown in Equation 10 and 11 below. The integral is calculated numerically using Simpsons Rule [45] and splits the range of temperature into 10 bins of equal value. This general form allows for the calculation of any material for which specific heat capacity is known. Those built into CTF are calculated using the MATPRO-11 specification. Materials with property tables not built into CTF can also be input as part of the input file, allowing more flexibility in modeling options.

$$h = \int_{68.27}^T c_p dT^* \quad \text{EQ 10}$$

$$T^* = \frac{T-68.27}{10} \quad \text{EQ 11}$$

Table 1: Material Property Modeling Options in CTF

Material property	Modeling Options
Fuel Thermal Conductivity	Halden, Amaya [46], Duriez, Modified NFI [47], MATPRO-11 [48], User Input Table
Fuel Emissivity	MATPRO-9 [49], User Input Table
Fuel Specific Heat Capacity	MATPRO-11 [48], User Input Table
Fuel Melting Temperature	MATPRO-11 [48]
Cladding Properties (zirconium)	MATPRO-11 [48]

The cladding thermal expansion, elastic modulus, and shear modulus are calculated using relations taken from MATPRO-11. The cladding thermal expansion is calculated using the moduli from the MATPRO-11 materials tables and the stresses and strains calculated from them based on the thermal gradient across the cladding. The equations for uranium dioxide material property options are shown below in Equations 12-22. The clad material properties equations are not shown but can be accessed through the MATPRO-11 handbook.

$$K_{MATPRO}(T) = C \left\{ \max \left(\frac{2335}{464+T}, 1.1038 \right) + 7.027 \cdot 10^{-3} \exp(1.867 \cdot 10^{-3} \cdot T) \right\} \quad \text{EQ 12}$$

$$C = \frac{1-\beta \cdot (1-TD)}{1-0.05 \cdot \beta} \quad \text{EQ 13}$$

$$\beta = 2.58 - (5.8 \cdot 10^{-4})T \quad \text{EQ 14}$$

Where: K_{MATPRO} = Thermal Conductivity $\left(\frac{Btu}{hr \cdot ft \cdot F} \right)$

T = Temperature (K)

TD = Theoretical Density (Unitless)

The MATPRO-11 model is valid over the range 500-3000 °K.

$$K_{Modified\ NFI}(T, Bu, Gad) =$$

$$\frac{1}{0.0452+0.000246T_k+0.00187Bu+1.1599Gad+(1-0.9\exp(-0.04Bu))0.038h\cdot Bu^{0.28}}$$

$$+ \frac{3.5 \cdot 10^9}{T_K^2} \exp\left(-\frac{16361}{T_K}\right) \quad \text{EQ 15}$$

$$h = \frac{1}{\left\{1.0+396 \exp\left(-\frac{6380}{T_K}\right)\right\}} \quad \text{EQ 16}$$

Where: $K_{Modified\ NFI}$ = Thermal Conductivity $\left(\frac{W}{m \cdot K}\right)$

T_K = Temperature (K)

Bu = Burnup $\left(\frac{MWd}{kgU}\right)$

Gad = Gadolinia Content (wt. %)

The Modified NFI model is valid over the following ranges of values:

$$300 \leq T_K \leq 3000$$

$$0 \leq Bu \leq 62$$

$$0.92 \leq TD \leq 0.97$$

$$0 \leq Gad \leq 10$$

$$K_{Halden}(T, Bu, Gad) = \frac{1}{0.1148+1.1599Gad+4 \cdot 10^{-3}Bu+2.475 \cdot 10^{-4}(1-0.00333Bu)T_C}$$

$$+0.0132 \exp(0.00188 \cdot T_C) \quad \text{EQ 17}$$

Where: K_{Halden} = Thermal Conductivity $\left(\frac{W}{m \cdot K}\right)$

T_C = Temperature (°C)

Bu = Burnup $\left(\frac{MWd}{kgU}\right)$

Gad = Gadolinia Content (wt. %)

The Halden model is valid over the following ranges of values:

$$300 \leq T_K \leq 3000$$

$$0 \leq Bu \leq 62$$

$$0.92 \leq TD \leq 0.97$$

$$0 \leq Gad \leq 10$$

The thermal conductivity models are further adjusted for the as-fabricated fuel density using correction factors. The Halden and Modified NFI models are adjusted using the Lucuta correction factor [50] in Equation 18 and the MATPRO-11 correlation is adjusted using the Fink factor formulation [51] in Equation 19.

$$K_{fuel} = K_{Correlation} \left(\frac{1.0789TD}{1+0.5(1-TD)} \right) \quad \text{EQ 18}$$

$$K_{fuel} = K_{Correlation} \left(\frac{1-(2.58-5.8 \cdot 10^{-4}T_C)(1-TD)}{1-0.05 \cdot (2.58-5.8 \cdot 10^{-4}T_C)} \right) \quad \text{EQ 19}$$

Where: T_C = Temperature ($^{\circ}C$)

TD = Theoretical Density (*Unitless*)

The fuel emissivity is calculated according to the following equation:

$$\epsilon_{UO_2} = 0.78557 + 1.5263 \cdot 10^{-5}T \quad \text{EQ 20}$$

Where: ϵ_{UO_2} = Fuel Emissivity (*Unitless*)

T = Temperature (K)

The specific heat capacity is calculated according to the following equation:

$$C_p = \left\{ \frac{K_1 \theta^2 \exp\left(\frac{\theta}{T}\right)}{T^2 \left(\exp\left(\frac{\theta}{T}\right) - 1\right)^2} + K_2 T + \frac{OM}{2} \frac{K_3 E_d}{RT^2} \exp\left(-\frac{E_D}{RT}\right) \right\} \quad \text{EQ 21}$$

Where: C_p = Specific Heat Capacity of uranium dioxide fuel $\left(\frac{J}{kg \cdot K}\right)$

T = Temperature (K)

OM = Oxygen-metal ratio (taken to be 2)

$$R = 8.3143 \left(\frac{J}{mol \cdot K}\right)$$

θ = Einstein Temperature

Table 2: Empirical Coefficients for UO2 Specific Heat Capacity

Fuel Type	$K_1 \left(\frac{J}{kg \cdot ^\circ K} \right)$	$K_2 \left(\frac{J}{kg \cdot ^\circ K} \right)$	$K_3 \left(\frac{J}{kg \cdot ^\circ K} \right)$	θ ($^\circ K$)	$E_D \left(\frac{J}{mol} \right)$
UO ₂	296.7	$2.43 \cdot 10^{-2}$	$8.745 \cdot 10^7$	535.285	$1.577 \cdot 10^5$

The fuel melting temperature is calculated according to the following equation:

$$T_M = \begin{cases} 3113.15 - 5 \cdot 10^{-4} Bu & X_{Pu} = 0 \\ T_{solidus} - 5 \cdot 10^{-4} Bu & X_{Pu} \neq 0 \\ 3115 - 4.8 Gad & Gad \neq 0 \end{cases} \quad \text{EQ 22}$$

$$T_{solidus} = 3113.15 - 5.41395 X_{Pu} + 7.46839 \cdot 10^{-3} X_{Pu}^2 \quad \text{EQ 23}$$

Where: T_m = Melting temperature (K)

Gad = Gadolinia content (wt. %)

Bu = Burnup $\left(\frac{MWd}{kgU} \right)$

X_{Pu} = Plutonia content (wt. %)

After calculating the material properties, the CTF fuel rod model further models several phenomena that are not included in the material property calculation. These include geometrical changes in the rod but also changes in conditions such as pressure and composition due to burnup. These are detailed below, and Table 3 contains a listing of some of the models available for the advanced fuel performance phenomena as well as the applicable models for the dynamic gap conductance model. Table 4 contains more information regarding the fuel deformation modelling options CTF accepts.

CTF includes a fuel deformation model that considers two types of deformation. The effect of pellet cracking on fuel thermal conductivity is considered as well as the thermo-mechanical effects of pellet and cladding expansion are considered in the gap thickness calculations. For the thermal conductivity effect, the uncracked conductivity is multiplied by a conductivity factor that is a function of the volume available for cracking (the gap thickness), as well as the uncracked thermal conductivity and the fill gas thermal conductivity. A mixture of up to six gases can be modeled by CTF. The effect of fuel and pellet expansion on the pellet cladding gap is considered using four phenomena: the fuel pellet thermal expansion, cladding thermal expansion, fuel relocation due to cracking, and cladding elastic expansion. This change in gap thickness affects the gap gas pressure for all cases including closed and open gap cases. The models for cracking are developed in CTF but certain portions—such as the fuel pellet cracking model—are lifted from third party simulation tools such as FRAPCON. This can be further investigated reading the CTF Theory Manual [3] and a listing of the fuel deformation modeling options in CTF can be found in Table 4.

Table 3: Fuel Performance Models in CTF

Fuel Performance Phenomenon	Modeling Option in CTF
Fuel Deformation (cracking, pellet/clad thermal expansion, clad elastic expansion)	CTF Default Model
Convective Gap Heat Transfer	Lanning & Hann [52]
Temperature Jump Distance	GAPCON-2 [53]
Conductive Gap Heat Transfer	Mikic/Todreas [54] [55]
Radiative Heat Transfer	Newton's law of Cooling and the Stefan-Boltzmann Equation

The general equation for the gap thickness change in a single time step is found below in Equation 24. The terms on the right-hand side are calculated in equations 25-31 below. Similar equations exist for axial changes in geometry but are omitted in this paper. A full list is available in the CTF Theory Manual [3].

$$\delta = \delta_0 - (\Delta r_{th})_{fuel} + (\Delta r_{th})_{clad} + (\Delta r_{rel})_{fuel} - (\Delta r_{el})_{clad} \quad \text{EQ 24}$$

Where: δ = Gap thickness (*in*)

δ_0 = Initial Gap thickness (*in*)

$(\Delta r_{th})_{fuel}$ = Pellet thermal expansion (*in*)

$(\Delta r_{th})_{clad}$ = Clad thermal expansion (*in*)

$(\Delta r_{rel})_{fuel}$ = Fuel relocation due to cracking (*in*)

$(\Delta r_{el})_{clad}$ = Clad elastic expansion (*in*)

$$(\Delta r_{th})_{fuel} = \sum_{i=1}^{NFUEL} \epsilon_{UO_2}(T_{ij}) \Delta r_i \quad \text{EQ 25}$$

$$(\Delta r_{th})_{clad} = \epsilon_r(T_j) \bar{r} \quad \text{EQ 26}$$

$$(\Delta r_{rel})_{fuel} = \delta_0 - 0.005r_f \quad \text{EQ 27}$$

$$(\Delta r_{el})_{clad} = \epsilon_\theta \bar{r} \quad \text{EQ 28}$$

$$\epsilon_\theta = \frac{\sigma_\theta - \nu \sigma_Z}{E} \quad \text{EQ 29}$$

$$\sigma_\theta = \frac{r_i P_i - r_o P_o}{t_c} \quad \text{EQ 30}$$

$$\sigma_Z = \frac{\pi r_i^2 P_i - \pi r_o^2 P_o}{\pi(r_o^2 - r_i^2)} \quad \text{EQ 31}$$

Where: ϵ_{UO_2} = Temperature dependent thermal strain for uranium dioxide

ϵ_r = Temperature dependent thermal strain for cladding material

Δr_i = Radial node radial width (*in*)

\bar{r} = Average cladding width (*in*)

r_f = Cold state fuel radius (*in*)

ν = Poisson's ratio (*unitless*)

E = Elastic modulus

t_c = cladding thickness (*in*)

σ_θ = Clad hoop stress

σ_Z = Clad axial stress

P_j = Pressure, where j=i refers to the clad interior and j=0 the clad outer

r_j = Clad radius, where j=i refers to the clad interior and j=0 the clad outer (*in*)

Heat transfer through the gap is a difficult quantity to determine, particularly in the case where a gap opens and closes over time, so various means of heat transfer are possible. To account for this, CTF calculates the gap heat transfer as the sum of three types of heat transfer modes: conduction through fill gas, solid-solid contact conduction, and radiative heat transfer. The

equations for each of these are shown below in Equations 32-41 as well as a listing of the equation terms.

$$H_{gap} = H_{gas} + H_{contact} + H_{rad} \quad \text{EQ 32}$$

$$H_{gas} = \begin{cases} \frac{k_{gas}}{t_g + 1.845(g_1 + g_2)} & \text{If Gap is open} \\ \frac{k_{gas}}{1.8(C(R_f + R_c) + (g_1 + g_2)) - 4.2 \cdot 10^{-7}} & \text{If Gap is closed} \end{cases} \quad \text{EQ 33}$$

$$C = 1.98 \exp(-8.8 \cdot 10^{-5} P_{int}) \quad \text{EQ 34}$$

$$(g_1 + g_2) = 2.0358 \cdot 10^{-5} \frac{k_{gas} \sqrt{\bar{T}_{gas}}}{P_{gas} \sum_{j=1}^N \frac{a_{jfj}}{\sqrt{M_j}}} \quad \text{EQ 35}$$

$$H_{contact} = \frac{5k_m}{\sqrt{R_f^2 + R_c^2}} \left(\frac{P_{int}}{Hz} \right)^n \left(\frac{R_f}{\lambda_f} \right) \quad \text{EQ 36}$$

$$k_m = \frac{2k_c k_f}{k_f + k_c} \quad \text{EQ 37}$$

$$n = \begin{cases} 0.5 & \frac{P_{int}}{Hz} < 0.0001 \\ 0.01 & 0.001 < \frac{P_{int}}{Hz} < 0.01 \\ 1.0 & \frac{P_{int}}{Hz} > 0.01 \end{cases} \quad \text{EQ 38}$$

$$\frac{R_f}{Hz} \approx \exp[0.5285 \ln(R_f - 5.738)] \quad \text{EQ 39}$$

$$H_{rad} = \frac{q_r''}{T_f - T_c} \quad \text{EQ 40}$$

$$q_r'' = \sigma_{SB} \frac{T_f^4 - T_c^4}{\frac{1}{\epsilon_f} + \frac{d_f}{d_c} \left(\frac{1}{\epsilon_c - 1} \right)} \quad \text{EQ 41}$$

The terms are defined as follows:

$$k_{gas} = \text{Gas thermal conductivity } \left(\frac{Btu}{hr \cdot ft \cdot F} \right)$$

$$k_f = \text{Fuel thermal conductivity } \left(\frac{Btu}{hr \cdot ft \cdot F} \right)$$

$$k_c = \text{Clad thermal conductivity } \left(\frac{Btu}{hr \cdot ft \cdot F} \right)$$

$$t_g = \text{Clad thickness } (ft)$$

$$(g_1 + g_2) = \text{Temperature jump distances } (ft)$$

$$R_f = \text{Fuel roughness } (ft)$$

$$R_c = \text{Cladding roughness } (ft)$$

$$P_{int} = \text{Interface pressure } (Psia)$$

$$P_{gas} = \text{Gas pressure } (Psia)$$

$$\bar{T}_{gas} = \text{Average gap gas Temperature } (^{\circ}K)$$

$$a_j = \text{Accommodation coefficient of gas } j \text{ (Correlation developed from GAPCON-2)}$$

$$f_j = \text{Mole Fraction of gas } j \text{ (Unitless)}$$

$$M_j = \text{Molecular weight of gas } j$$

$$T_f = \text{Fuel surface temperature } (R)$$

$$T_c = \text{Cladding surface temperature } (R)$$

$$\sigma_{SB} = \text{Stefan-Boltzmann constant } \left(1.714 \cdot 10^{-9} \frac{Btu}{hr \cdot ft^2 \cdot R^4} \right)$$

$$\epsilon_f = \text{Fuel emissivity } (Unitless)$$

$$\epsilon_c = \text{Clad emissivity } (Unitless)$$

$$d_c = \text{Clad diameter } (ft)$$

$$d_f = \text{Fuel diameter } (ft)$$

Another important part of CTF's fuel rod model is the dynamic gap conductance modelling. This model allows the gap conductance to change based on changes in gap thickness, contact between pellet and clad, and radiation heat transfer. The model also accounts for the non-linearity of the temperature gradient across the gap near the gap-surface interfaces when applying

convective heat transfer. This non-linearity is accounted for using a temperature jump distance. Conductive heat transfer is used when contact occurs between the pellet and clad. Contact occurs when the calculated gap thickness is less than the sum of the pellet and cladding surface roughness, provided as a user input. Radiative heat transfer across the gap is calculated as the radiative heat flux divided by the gap temperature gradient [3].

The fuel deformation model in CTF allows for selection of differing models to calculate individual deformation phenomena. CTF allows for the whole deformation/degradation model to be toggled on and off, as well as allowing individual phenomena modeling to be toggled. The specific phenomena that CTF allows toggling for are the fuel relocation induced thermal conductivity degradation, fuel degradation, fuel swelling, fuel densification, fuel relocation induced gap conductivity changes, and cladding creep. The modeling options available in CTF can be found in Table 4 below.

Table 4: Fuel Deformation Modeling Options in CTF

Fuel Deformation Phenomenon	Modeling Option in CTF
Thermal Conductivity Degradation from Fuel Relocation	FRACAS-1 [44]
Fuel Swelling	MATPRO-11 [48] for all FPs, MATPRO-11 for solid FPs & FRACAS-1 [44] for gaseous FPs
Fuel Densification	MATPRO-11 [48], FRACAS-1 [44], ESCORE
Gap Conductivity Changes from Fuel Relocation	FRACAS-1 [44], ESCORE [56], Modified ESCORE
Cladding Creep	BISON [57], ESCORE [56]

The FRACAS-1 model mentioned in Table 4 is the default deformation model in FRAPCON for solid materials. CTF does not take any of the cladding deformation portions on the model, only fuel deformation portions. CTF also has several options for creep and fuel densification sourced from different fuel performance codes such as FRAPCON, BISON, and ESCORE (FALCON is developed from ESCORE and there is a large overlap in the code options). The equation for the thermal conductivity degradation because of fuel relocation is provided below from the FRACAS-1 fuel relocation model in FRAPCON:

$$k_{eff} = \left[1 - 0.3 \frac{\delta_0}{0.8 \cdot 10^{-4}} \left(1 - \frac{k_g}{k_{lab}} \right) \right] k_{lab} \quad \text{EQ 42}$$

The terms are defined as follows:

$$k_{eff} = \text{Effective fuel thermal conductivity} \left(\frac{\text{Btu}}{\text{hr} \cdot \text{ft} \cdot \text{F}} \right)$$

$$k_g = \text{Gap gas thermal conductivity} \left(\frac{\text{Btu}}{\text{hr} \cdot \text{ft} \cdot \text{F}} \right)$$

$$k_{lab} = \text{Uncracked fuel thermal conductivity} \left(\frac{\text{Btu}}{\text{hr} \cdot \text{ft} \cdot \text{F}} \right)$$

$$\delta_0 = \text{Initial gap thickness (m)}$$

The fuel swelling models available in CTF are the MATPRO-11 models and the FRACAS-1 models. The MATPRO-11 solid FP swelling model is the only solid FP model available and is shown in Equation 43 below. The MATPRO-11 and FRACAS-1 gaseous FP models are shown in Equations 44 and 45 below. The MATPRO-11 gaseous FP model is used when temperature is below 2800 K; if the fuel temperature exceeds this quantity, the swelling is assumed to be 0. The FRACAS-1 gaseous FP swelling model [58] is phased in between 40 and 50 GWd/MTU using a linear factor that varies between 0 and 1 from 40 to 50 GWd/MTU, respectively.

$$S_S = 2.5 \cdot 10^{-29} B_S \quad \text{EQ 43}$$

Where: S_S = Fractional volume change due to solid FPs (*Unitless*)

B_S = Burnup over the timestep increment (incremental burnup) $\left(\frac{\text{fission}}{\text{m}^3}\right)$

$$S_{G,MATPRO-11} = 8.8 \cdot 10^{-56} (2800 - T)^{11.73} \exp[-0.0162(2800 - T)] \\ \times \exp[-8.0 \cdot 10^{-27} Bu] B_S \quad \text{EQ 44}$$

$$S_{G,FRACAS-1} = \begin{cases} 4.55 \cdot 10^{-5} T_C - 4.37 \cdot 10^{-2} & 960^\circ\text{C} < T_C < 1370^\circ\text{C} \\ -4.05 \cdot 10^{-5} T_C + 7.4 \cdot 10^{-2} & 1370^\circ\text{C} < T_C < 1832^\circ\text{C} \end{cases} \quad \text{EQ 45}$$

Where: $S_{G,Model}$ = Fractional volume change due to gaseous FPs (*Unitless*)

B_S = Burnup over the timestep increment (incremental burnup) $\left(\frac{\text{fission}}{\text{m}^3}\right)$

Bu = Total fuel burnup $\left(\frac{\text{fission}}{\text{m}^3}\right)$

T = Fuel temperature (K)

T_C = Fuel temperature ($^\circ\text{C}$)

The fuel densification model equations available in CTF are the FRACAS-1 model, the MATPRO-11 model, and the ESCORE model. They are shown below in Equations 46-53. The MATPRO-11 model has two different formulations, depending on if the resintering density is provided as part of the input. The formulation if resintering density is provided can be found in Equation 46 and the other formulation if not resintering density is provided is found in Equation 47. The constant B in Equation 46 is taken to be 0 in CTF.

$$D_{S,max,MATPRO} = \begin{cases} -0.0015 \rho_{rs} & T < 1000 \text{ K} \\ -0.00285 \rho_{rs} & T \geq 1000 \text{ K} \end{cases} \quad \text{EQ 46}$$

$$D_{S,max,MATPRO} = \begin{cases} -\frac{22.2(1.0-TD)}{(T_{sint}-1453)} & T < 1000 \text{ K} \\ -\frac{66.6(1.0-TD)}{(T_{sint}-1453)} & T \geq 1000 \text{ K} \end{cases} \quad \text{EQ 47}$$

$$D_{S,MATPRO} = D_{S,max,MATPRO} + \exp[-3(Bu + B)] + 2 \exp[-35(Bu + B)] \quad \text{EQ 48}$$

Where: $D_{S,max,MATPRO}$ = Maximum possible dimension change from irradiation densification
(Unitless)

$D_{S,MATPRO}$ = Fuel dimension change (Unitless)

ρ_{rs} = Resintering density change $\left(\frac{kg}{m^3}\right)$

TD = Theoretical density (Unitless)

Bu = Total fuel burnup $\left(\frac{MWd}{kgU}\right)$

T = Fuel temperature (K)

T_{sint} = Sintering temperature (K)

The ESCORE model requires resintering density to be provided as user input.

$$D_{S,ESCORE} = \rho_{rs} \left(\exp \left(\frac{\log(0.010)Bu}{C \cdot 5 \cdot 10^3} \right) \right) \quad \text{EQ 49}$$

$$C = \begin{cases} 7.2 - 4.3 \frac{(T-25)}{500} & T \leq 1382^\circ F \\ 1.0 & T > 1382^\circ F \end{cases} \quad \text{EQ 50}$$

Where: $D_{S,ESCORE}$ = Fuel dimension change (Unitless)

ρ_{rs} = Resintering density change $\left(\frac{kg}{m^3}\right)$

T = Fuel temperature ($^\circ F$)

Bu = Total fuel burnup $\left(\frac{MWd}{kgU}\right)$

The FRACAS-1 model is similar in form to the MATPRO-11 model in that it calculates a maximum dimensional change possible prior to calculating the actual change over the timestep. It also includes two formulations for whether resintering density is included or not. The formulation with the resintering density is found in Equation 51 and the formulation for no provided resintering density is found in Equation 52.

$$D_{S,max,FRACAS} = \frac{100\rho_{rs}}{3TD} \quad \text{EQ 51}$$

$$D_{S,max,FRACAS} = \begin{cases} -\frac{22.2(1.0-TD)}{(T_{sint}-1453)} & T < 1000 K \\ -\frac{66.6(1.0-TD)}{(T_{sint}-1453)} & T \geq 1000 K \end{cases} \quad \text{EQ 52}$$

$$D_{S,FRACAS} = D_{S,max,FRACAS} + \exp[-3(Bu + B)] + 2 \exp[-35(Bu + B)] \quad \text{EQ 53}$$

Where: $D_{S,max,FRACAS}$ = Maximum possible dimension change from irradiation densification (*Unitless*)

$D_{S,FRACAS}$ = Fuel dimension change (*Unitless*)

ρ_{rs} = Resintering density change $\left(\frac{kg}{m^3}\right)$

TD = Theoretical density (*Unitless*)

Bu = Total fuel burnup $\left(\frac{MWd}{kgU}\right)$

T = Fuel temperature (K)

T_{sint} = Sintering temperature (K)

To account for changes in gap width because of fuel relocation, CTF uses the three models listed in Table 4. The formulation for the FRAPCON (FRACAS-1) model is shown below in Equations 54 and 55. Equation 54 is only valid for a burnup higher than 0.0937 GWd/MTU; at lower burnups the fractional gap closure is set to 0.055.

$$\frac{\Delta t_g}{t_g} = 0.055 + \min(reloc, reloc \cdot (0.5795 + 0.2447 \ln(BU))) \quad \text{EQ 54}$$

$$reloc = \begin{cases} 0.345 & P < 20 \\ 0.345 + \frac{P-20}{200} & 20 < P < 40 \\ 0.445 & P > 40 \end{cases} \quad \text{EQ 55}$$

Where: $\frac{\Delta t_g}{t_g}$ = Fraction of as fabricate gap closure (*unitless*)

P = Local power $\left(\frac{kW}{ft}\right)$

BU = Local burnup $\left(\frac{GWd}{MTU}\right)$

The ESCORE model formulation is shown below in Equations 56 and 57. This model is sourced from ESCORE, and further information can be found in the FALCON Theory manual [56].

$$\frac{\Delta t_g}{t_g} = 0.8 \cdot reloc(0.005BU^{0.3} - 0.2D_o + 0.3) \quad \text{EQ 56}$$

$$reloc = \begin{cases} 0 & q' \leq 6 \\ (q' - 6)^{\frac{1}{3}} & 6 < q' \leq 14 \\ \frac{q' - 10}{2} & q' > 14 \end{cases} \quad \text{EQ 57}$$

Where: $\frac{\Delta t_g}{t_g}$ = Fraction of as fabricate gap closure (*unitless*)

q' = Pellet average linear heat rate $\left(\frac{kW}{ft}\right)$

BU = Local burnup $\left(\frac{MWd}{MTU}\right)$

The Modified ESCORE model uses the same formulation as the standard ESCORE relocation induced gap change shown in Equations 56. It is modified from the “standard” ESCORE model by difference in the “reloc” factor. This change is shown in Equation 58 below.

$$reloc = \begin{cases} \frac{q'}{3} & q' \leq 6 \\ (q' - 6)^{\frac{1}{3}} & 6 < q' \leq 14 \\ \frac{q' - 10}{2} & q' > 14 \end{cases} \quad \text{EQ 58}$$

Where: q' = Pellet average linear heat rate $\left(\frac{kW}{ft}\right)$

BU = Local burnup $\left(\frac{MWd}{MTU}\right)$

The cladding creep models available are sourced from BISON and ESCORE. The BISON sourced model is the Hoppe irradiation creep model [59] and the Hayes-Kassner thermal creep model [60]. The ESCORE cladding creep model combines both irradiation and thermal creeps into one model. It is included as a default option in the FALCON fuel performance code [56]. In both the ESCORE and BISON (Hoppe-Hayes) models, the irradiation and thermal creep rates are added to one another to find a net creep rate. The equations for the Hoppe Hayes model can be found below in Equations 59 -61 while the ESCORE cladding creep equations are shown in Equations 62 and 63. The material constants for various cladding types are also included in Table 5 and Table 6 for the Hope Hayes model and ESCORE model, respectively.

$$\dot{\epsilon}_{ir} = C_0 \Phi^{C_1} \sigma_m^{C_2} \quad \text{EQ 59}$$

Where: $\dot{\epsilon}_{ir}$ = Effective irradiation Creep Rate $\left(\frac{1}{s}\right)$

Φ = Fast neutron flux $\left(\frac{\text{neutrons}}{m^2 \cdot s}\right)$

σ_m = Effective (von Mises) stress (MPa)

With material constants C_0 , C_1 , and C_2 implemented in CTF shown below in Table 5 for stress relief annealed (SRA) cladding. The Hoppe model as implemented in BISON, includes additional cladding types including recrystallized annealed (RXA), partially recrystallized annealed (PRXA), and SRA ZIRLO.

Table 5: Hoppe Irradiation Creep Material Constants in CTF

Clad Type	C_0	C_1	C_2
SRA	9.88e-28	0.85	1.0

$$\dot{\epsilon}_{ss} = A_0 \left(\frac{\sigma_m}{G} \right)^n e^{\frac{-Q}{RT}} \quad \text{EQ 60}$$

$$G = 4.2519 \times 10^{10} - 2.2185 \times 10^7 T \quad \text{EQ 61}$$

Where: $\dot{\epsilon}_{ss}$ = Effective thermal creep rate $\left(\frac{1}{s} \right)$

σ_m = Effective (von Mises) stress (MPa)

Q = Activation Energy $\left(\frac{J}{mol} \right)$

R = Universal gas constant $\left(\frac{J}{mol \cdot K} \right)$

G = Shear modulus (Pa)

T = Clad Temperature (K)

And with material constants $A_0 = 3.14 \times 10^{24}$ and $n = 5.0$. The formulation for the ESCORE clad creep model is found below.

$$\dot{\epsilon}_{ss} = A_1 [\sinh(A_2 - \sigma_\theta^{A_3})]^{A_4} A_5 t^{A_5-1} \cdot t \cdot \sigma_y^{A_6} e^{\frac{-A_7}{T}} \quad \text{EQ 62}$$

$$\dot{\epsilon}_{ir} = B_1 B_2 t^{B_2-1} \cdot t \cdot \Phi^{B_3} \sigma_\theta^{B_4} e^{\frac{-B_5}{T}} \sigma_y^{B_6} [\cos(\theta_{max})]^{B_7} \quad \text{EQ 63}$$

Where: $\dot{\epsilon}_{ss}$ = Effective thermal creep rate $\left(\frac{1}{s} \right)$

$\dot{\epsilon}_{ir}$ = Effective irradiation Creep Rate $\left(\frac{1}{s} \right)$

Φ = Fast neutron flux $\left(\frac{neutrons}{m^2 \cdot s} \right)$

σ_θ = Midwall hoop stress (MPa)

t = Time of exposure (hours)

T = Clad Temperature (K)

σ_y = Clad yield strength at room temperature (MPa)

θ_{max} = Angle of maximum basal pole or radial direction intensity = 30°

With the following material constants in Table 6:

Table 6: ESCORE Clad Creep Model Material Constants

Constant	Value	Constant	Value
A_1	1.39E08	B_1	2.35E – 21
A_2	3.29E – 05	B_2	0.811
A_3	2.28	B_3	0.595
A_4	0.997	B_4	1.352
A_5	0.77	B_5	22.91
A_6	0.956	B_6	1.58
A_7	24657	B_7	2.228

Gaps in CTF Modeling Capabilities

While the inclusion of the CTFFuel fuel rod module increases the fuel performance capabilities of CTF, there remain some gaps in the modeling ability when compared to standard fidelity fuel performance codes. These gaps exist due to the difficulty of modeling certain fuel performance phenomena, as well as the computational cost of macro-level fuel mechanics. The gaps within CTF fuel rod modeling can be split into three groups: (1) missing phenomena, (2) incomplete or partial modeling, and (3) limits in ranges of applicability of existing models.

The primary gaps in CTF’s modeling abilities are the missing phenomena. These are physical phenomena that are not modeled at all in CTF, leading to inaccuracy in the simulation when those phenomena occur. The primary missing phenomenon for this work is the lack of FGR modeling. CTF does not offer any kind of fission gases, and no models currently implemented take fission gases into account other than certain thermal conductivity models, but their effect is not fully quantified. In addition, there is no modeling of FFRD effects compared to traditional fuel

performance codes, one other key model missing is burst and rod failure modeling. Burst modeling allows the fuel performance tool to determine whether a fuel rod has failed and is not incorporated into CTF. This would include including the operational limits for various models and geometry to determine not only when failure occurs, but what constitutes fuel failure.

Another shortcoming of the CTF modeling abilities is the incomplete or partial modeling of physical phenomena. There are certain phenomena that are modeled in CTF using either incomplete models, or models that are not the most accurate. As a TH code, it is expected that fuel performance modeling will not be at the same standard as dedicated fuel solvers such as OFFBET, BISON, or FRAPTRAN/FRAPCON; however, it is desired that all models are high enough resolution to provide meaningful results. To this end, the resolution of existing models should be verified to be sufficiently high for the CTF goals. For example, CTF does not allow for changing gas type inventory in the pellet-clad gap. As these gases have different material properties, heat transfer in the gap will depend on the gap gas composition. In situations where the gap composition may change, such as when significant FGR occurs, it may be worth investigating the effect of the gap gas composition changes on gap heat transfer.

The effect of the thermal conductivity degradation (TCD) is also unconfirmed. The thermal conductivity correlations that are burnup dependent are likely considered TCD due to fission gases and grain restructuring, but TCD due to HBS formation may not be considered. As these are correlations from experimental data, the limits of applicability are also important to consider. Within CTF, no models are approved for use above 62 GWd/MTU, which is the former operational limit for nuclear reactors in the United States [61]. The conditions of the experimental data must also be considered, as if the experimental samples did not include HBS formation, it is unlikely that they will be accurate for fuel where the HBS is present.

CHAPTER 4 – Modeling Approaches for Fission Gas Release

Introduction

Having discussed the current capabilities in the CTF solid component modeling approach, the shortcomings were identified with respect to HBU modeling. In this chapter, the approaches to steady state and transient FGR modeling are presented to fill the shortcomings CTF has for modeling FGR. Additional background is provided on a model-by-model basis for quantities needed in certain FGR models.

To model FGR, the existing gas distributions within the fuel pellet must be known. This is true both for steady state and transient models, but especially for the transient models as steady state models can calculate gas concentrations themselves. The gas concentrations are strongly dependent on the fuel microstructure due to the formation mechanisms of fission gases (namely nuclear fission). This in depth and high-fidelity type of calculation is beyond the capabilities of CTF as a subchannel code, and implementing a full microstructure model in CTF would lead to outwardly expensive computation times. However, the effect of the fission gas atom creation can be modeled without knowing the complete fuel microstructure. Regardless of the atomic transport method, general transport rates can be calculated, specifically for diffusion of atoms through the fuel and applied to the fuel structure on a macro scale.

Steady state and transient FGR models of varying degrees of fidelity will be introduced and explained. Starting from low fidelity models using simple correlations and going to high fidelity microstructure-based models, the design space for FGR models is investigated. The advantages and disadvantages of each model are explored, and the modeling requirements are noted. Finally, suitable models for implementation in CTF are identified and selected for future testing.

Steady State Fission Gas Release Models

Steady-state FGR models attempt to model the gas concentrations in the fuel compact and amount of gas released from the crystal matrix. Gas concentrations are useful for determining changing material properties, while the release quantities are often used for rod failure modeling. There are three distinct fidelities of steady state FGR models: low fidelity, standard fidelity, and high fidelity. These model steady state diffusion process to varying degrees, as well as having different release criteria for the fission gases.

Low fidelity steady state models simulate the initial phase of the FGR process described in Chapter 2—specifically, the formation and diffusion of gas atoms within the grains. These models rely on atomic diffusion to estimate concentrations of fission gases within the fuel matrix. To achieve this, the existing gas concentrations and the diffusion through the fuel pellet must be computed. A release criterion is established, and the impact of the released gas is then evaluated. The next types of models are standard fidelity models, which simulate not only the diffusion of gas atoms through the bulk uranium dioxide lattice but also their coalescence and release at the grain boundaries. This higher level of fidelity provides more accurate predictions of fission gas distribution and a more precise determination of release criteria. In contrast, low-fidelity models often assume gas release occurs immediately after diffusion to the grain boundaries. However, research indicates this assumption is unrealistic, as fission gases tend to accumulate at grain boundaries before release. Standard fidelity models aim to replicate this grain boundary behavior as well as model the intra-granular fission gas behavior.

High fidelity steady-state FGR models attempt not only to calculate the intra- and inter-granular gas concentrations but also to fully model the inter-granular behavior, including grain boundary tunneling, and more accurately predict the release criteria. This type of model tends to

model the full grain microstructure to predict defects in the crystal lattice that will lead to changes in inter-granular behavior. All three steady-state FGR model fidelities model the atomic diffusion process to calculate the gas concentrations within the fuel pellet and the amount of gas released.

The Booth model [62] serves as a prime example of a low-fidelity steady-state FGR model. It employs a set of integro-differential equations and simplifies the process by treating all fission products as a single "gas type," along with several other assumptions. This approach results in a low-fidelity FGR model. The Booth model does not distinguish between intra-granular gas bubbles and grain boundary bubbles, instead assuming that all gas is released upon reaching the grain boundary. The fuel rod is divided into cells, with the contribution of each cell multiplied by its fractional volume. The sum of these contributions gives the overall net release percentage. The release percentage for each individual cell is determined using Equation 64 below, where D' represents the diffusion coefficient divided by the square of the average grain size. The model does not account for varying grain sizes or other fuel microstructures, does not model gas re-solution, and uses a constant diffusion coefficient based on the mean fuel rod temperature. Additionally, the Booth model does not accommodate HBS. Despite these limitations, it is effective as a low-fidelity model for calculating steady-state FGR. While the Booth model only predicts steady-state fission gas behavior, it can be paired with an empirical transient model to simulate both steady-state and transient FGR.

$$F = 1 - \frac{6}{90D'T} + \frac{6}{4\pi D't} \sum_{n=1}^{\infty} \frac{e^{-n^2\pi^2 D't}}{n^4} \quad \text{EQ 64}$$

A prominent example of a standard fidelity FGR model is the Modified Forsberg-Massih model [30]. This integro-differential model calculates the release of general fission gas atoms

based on the material properties and burnup of the fuel. The original model [63], derived from the Booth model, modifies the Booth model boundary conditions to account for time-varying grain boundary concentrations. This transforms the original equation into a system of equations that can calculate gas particle density at the grain boundary and within intra-granular bubbles. Additional dependencies between these quantities are introduced, and the full system can be found in Forsberg & Massih's second paper, with the general rate equation presented in Equation 65. Unlike low-fidelity models where diffusion coefficients remain static, this model allows the diffusion coefficients to change over time, with burnup and power. These improvements enable the calculation of both steady-state release and the accumulation of fission gases in intra-granular bubbles and at grain boundaries.

$$\frac{\partial C(r,t)}{\partial t} = D(t) \left(\frac{\partial}{\partial r^2} + \frac{2}{r} \frac{\partial}{\partial r} \right) C(r,t) + \beta(t) \quad \text{EQ 65}$$

With boundary conditions:

$$C(r, 0) = 0,$$

$$C(a, t) = \frac{b(t)\lambda N(t)}{2D(t)}$$

Where: $C(r, t)$ = Concentration of gas atoms

a = Radius of fuel grain

$\beta(t)$ = Gas production rate $\left(\frac{1}{s}\right)$

b = Gas re-solution rate $\left(\frac{1}{s}\right)$

λ = Re-solution depth from grain boundary (m)

$N(t)$ = Number of gas particles per unit area of grain on the grain boundary $\left(\frac{1}{m^2}\right)$

$D(t)$ = Gas diffusion coefficient

Further modifications included to the Modified Forsberg Massih model enhance its accuracy by allowing grain sizes to evolve and accounting for gas re-solution within the grains

[44]. The HBS effect is incorporated by modeling grain restructuring and changes in porosity and gas release behavior. This model is the standard model implemented in the fuel performance code FRAPCON and is referred to as the FRAPFGR model. The addition of these supporting models to better simulate the input to the Modified Forsberg Massih model, namely the grain size change over time [64], better inform the model and are expected to increase the accuracy particularly in situations where the grain size has changed significantly from the as-fabricated microstructure. This is particularly true at high temperatures and varying burnups [65].

TRANSURANUS fuel performance code [66] employs a diffusion-based model like the Modified Forsberg-Masih model, and in fact, the governing rate equation is identical (found in Equation 63). However, there are differences in how diffusion coefficients are calculated and in certain assumptions, such as variations in dihedral half angles and grain sizes [66]. These differences are due to a different application of the basic intra-granular fission gas diffusion, taken from research by Speight [67]. The release mechanism remains the same, relying on a saturation concentration at which gas is released. In TRANSURANUS, this concentration can be set as a constant, though advancements allow for the calculation of both grain sizes and average bubble volumes [68] to establish the release criterion. Unlike earlier models, TRANSURANUS specifically accounts for lenticular bubbles rather than assuming they are spherical. It also assumes that no loss occurs between the gas arrival rate and the absorption rate at the grain boundary. Additionally, this model utilizes a different grain growth approach compared to the modifications made to the Modified Forsberg-Masih model by earlier authors implemented in FRAPCON [44]. Gas re-resolution is possible for intra-granular bubbles in this model, but atoms cannot re-solve from the grain boundaries back into the grain interior. A more in-depth analysis and discussion of the modeling of fission gas behavior in TRANSURANUS is also available in the references [66].

The FALCON fission gas behavior model provides a more detailed analysis by breaking the process down to the microstructural level [69]. This model calculates the equilibrium concentrations of vacancies and interstitials within the lattice and uses this data to determine bubble coalescence both within the grains and on the grain surfaces. It offers a more comprehensive calculation of bubble radius through a differential equation that tracks changes in bubble size and distinguishes between individual species of fission gas. Additionally, it separates intra-granular and inter-granular processes while relying on a similar formulation for grain boundary physics as seen in the TRANSURANUS model [28]. The calculations for diffusion coefficients, as well as the formulation of grain growth and kinetics models, also differ from those used in earlier described models.

The BISON [57] steady state modeling of fission gases is based on the TRANSURANUS model [68]. This model is described in detail earlier in this paper. The governing equations and supporting models to calculate bubble growth, coalescence, and release are identical and identified in both the TRANSURANUS and BISON theory manuals and their supporting documentation.

OFFBEAT [70], a complex multi-dimensional fuel behavior solver is an open-source fuel performance code based on OpenFOAM [71] that also includes a fission gas behavior module. The SCIANTIX gas behavior solver is incorporated in this fuel performance code to model fission gas behavior. SCIANTIX is a 0-dimensional open-source code to model the behavior of inert gases (i.e. fission gases) in nuclear fuel at a material grain level. It can be used as a standalone code, but it is suggested to be coupled with separate fuel performance codes such as TRANSURANUS, OFFBEAT, and FRAPCON/FRAPTRAN [72]. SCIANTIX covers intra-granular gas diffusion, bubble nucleation, bubble growth through trapping and fission fragment interaction, including re-solution events. Accumulation of bubbles at grain phases is modeled, as well as bubble growth,

interconnection, coalescence, and eventual grain face saturation and release. It also calculates the fuel swelling due to gaseous FPs. It can also consider fuel microstructure changes with regards to changing average grain size and phenomena particular to the HBS. SCIANTIX models the intra-granular gaseous diffusion using spherical grains, similarly to the Booth and Modified Forsberg Massih models [62] [63]. It uses the same changing boundary conditions as the Modified Forsberg Massih model and uses the system of equations shown in Equations 66-68. Several modeling options are provided for values such as diffusion coefficients, intra-granular resolution, trapping, and nucleation rates. A description of the full set of equations for the calculation of both inter- and intra-granular bubbles, as well as the calculation of the modeling options can be found in the references [72].

$$\frac{\partial c}{\partial t} = D \frac{1}{r^2} \frac{\partial}{\partial r} r^2 \frac{\partial}{\partial r} + bm - gc + S \quad \text{EQ 66}$$

$$\frac{\partial m}{\partial t} = -bm + gc \quad \text{EQ 67}$$

$$\frac{dN_{ig}}{dt} = \nu - bN_{ig} \quad \text{EQ 68}$$

Where: c = single-atom gas concentration $\left(\frac{1}{m^3}\right)$

D = Intra-granular diffusivity $\left(\frac{m^2}{s}\right)$

b = Intra-granular irradiation-induced resolution rate $\left(\frac{1}{s}\right)$

m = Gas concentration in intra-granular bubbles $\left(\frac{1}{m^3}\right)$

g = Intra-granular trapping rate $\left(\frac{1}{s}\right)$

S = Intra-granular bubble gas production rate $\left(\frac{1}{m^3 s}\right)$

N_{ig} = Intra-granular bubble concentration $\left(\frac{1}{m^3}\right)$

ν = Intra-granular nucleation rate $\left(\frac{bub}{m^3 s}\right)$

Transient Fission Gas Release Models

As noted in Chapter 2, the release process for transient FGR is significantly different from the steady state release process. Steady state release tends to be a diffusive process while transient release is a cracking or burst phenomenon that is related to micro-cracking and geometrical changes in the crystal microstructure. A different model must thus be used to determine the FGR. Two distinct model fidelities exist for transient models: low fidelity and high-fidelity models. Low fidelity models are temperature or enthalpy-based correlations based on experimental data while high fidelity models will determine where cracking will occur and to what extent, then use this information to determine the volume of released gas. Transient FGR models are currently being developed as new experiments are performed and sensors are developed to gather relevant information.

The simplest models for FGR are empirical models for transient release, which are based on the fuel temperature or energy deposition and burnup and are derived from experimental data. These models tend to be highly conservative but provide an estimate of the release percentage in the gap and plenum areas. An example, presented by the U.S. NRC [42] and shown in Figure 14, illustrates the high burnup correlation with the upper red line and the low burnup correlation with the lower blue line. The data points used in this model come from PWR, BWR, and VVER reactors and include both uranium dioxide-based and MOX fuels. The equations for the high and low burnup correlations are shown in the graph in Figure 14.

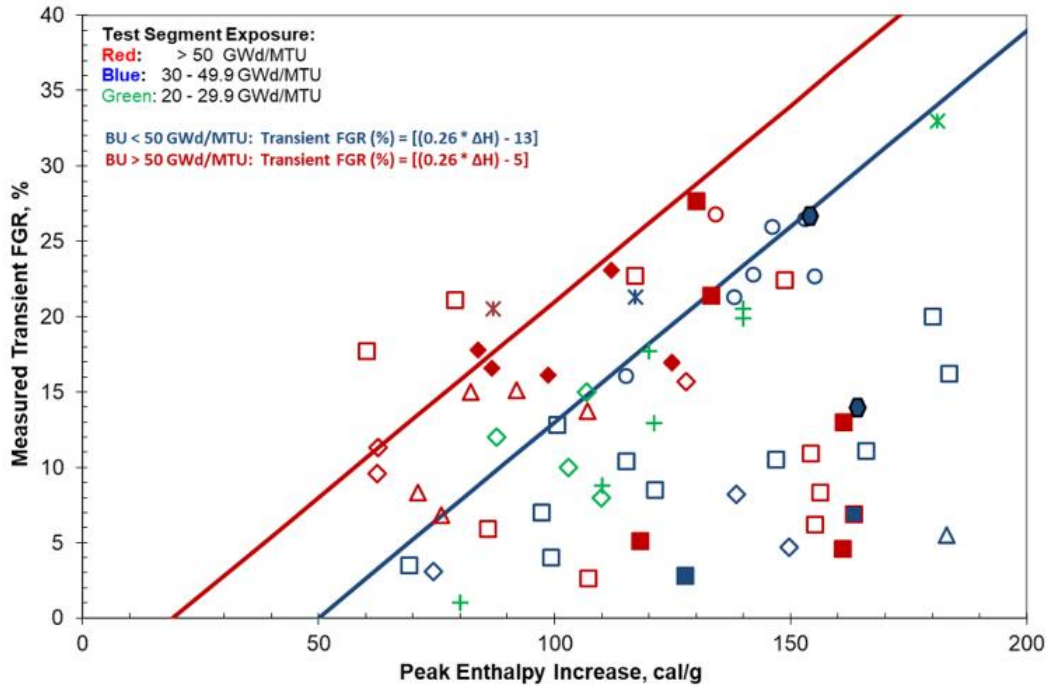


Figure 14: NRC provided tFGR correlation with experimental data points provided [73]

Transient FGR models for high-fidelity simulations are still largely empirical. Due to the complexity of burst cracking, empirical models currently offer the most accurate predictions for transient gas release. A representative example is the FRAPTRAN release model [74], which relies on the fuel's microstructure and temperature. The model distinguishes between gas located at grain boundaries and within intra-granular bubbles, releasing different percentages of the available gas inventory depending on whether the fuel grains have been restructured due to the HBS. One limitation of this model is that it requires pre-existing gas concentration throughout the fuel microstructure, which means that a detailed steady-state model for grain boundary concentration is needed, or external gas concentration data must be provided from a separate computational tool. Pseudo-code logic for this model is provided below in Figure 15. Unlike the U.S. NRC's suggested release model, which estimates a release percentage, this model directly outputs the quantity of

gas released, making it particularly useful for calculating parameters like rod internal pressure. Despite its simplicity, the model remains effective as it is primarily based on temperature and HBS formation.

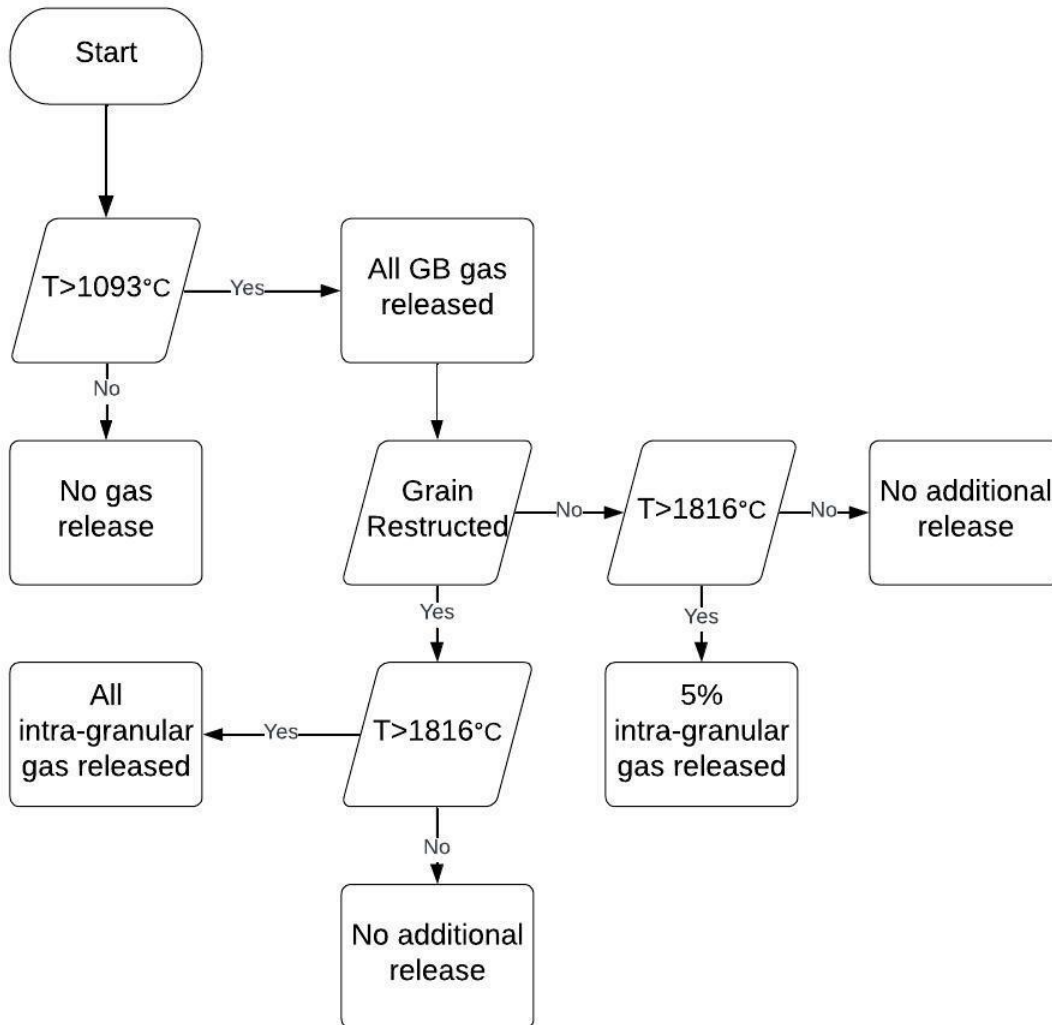


Figure 15: FRAPTRAN tFGR model logic [74]

Additional transient FGR models can be found in the FALCON fuel performance code. The FALCON tFGR model features multiple release pathways for fission gases in both restructured and unrestructured fuel grains [75]. The criterion for gas release due to grain boundary

fracture involves calculating the de-cohesive stress normal to the fission gas bubble, which depends on the pressure inside the fission gas bubbles, the external hydrostatic pressure, and the fractional coverage of both closed and open gas pores. The fracture threshold is derived from the MATPRO material libraries [76] and calculates fracture stress based on the temperature prior to the transient event and the fractional coverage of fission gas pores on the grain faces. This model also accounts for the over-pressurization of fission gas pores during high burnup irradiation [75]. Gas release is divided between grain boundary pores and intra-granular bonding traps, with both release rates driven by the pressure differential between the fission gas traps and the nearest open surface. The equations governing these processes are provided below in Equations 69 and 70. Here, t and t_0 represent the timestep and the time of fracture occurrence, respectively, while k_1 is the fraction of closed pores that open when the fracture happens. $N_1(t_0)$ refers to the concentration of fission gas available at the time of fracture, and τ_i represents time constants for burst FGR at the grain boundaries and intra-granular traps. The L_3 term is the specific gas loss to bonding-assisted traps, a type of loss accounted for in the model. The full system of differential equations governing the loss and change in bubble pore coverage in the FALCON tFGR model are found in equations 17-22 of Reference [75].

$$Release_{GB} = k_1 N_1(t_0) e^{\left(\frac{-t-t_0}{\tau_1}\right)} \quad \text{EQ 69}$$

$$Release_{TR} = \frac{L_3}{\tau_2} \quad \text{EQ 70}$$

The transient FGR model used in TRANSURANUS is also available as an option in BISON [36] and differs from the FALCON and FRAPTRAN models previously discussed. The TRANSURANUS model emphasizes the role of micro-cracks in the fuel lattice in altering the gas storage capacity. It considers the healing of these micro-cracks, with the rate of their formation

dependent on both temperature and burnup and varies depending on whether the transient involves heating or cooling [77]. The effect of micro-cracking increases exponentially as the fuel temperature approaches a critical value where cracking is most pronounced. This results in the gas release rate reaching its peak at a central temperature calculated for each burnup. As of 2017, the same model has been implemented in BISON [78], providing similar functionalities. A distinctive feature of this model is its non-discrete release threshold, which allows for continuous gas release during transients while still capturing the burst behavior typical of transient release. Figure 16 below illustrates the micro-cracking effect parameter for a central temperature of 1773 K for both heating and cooling transients. Since the release rate is closely tied to the micro-cracking parameter, the gas release behavior on a grain-by-grain basis reflects the pattern shown in Figure 16.

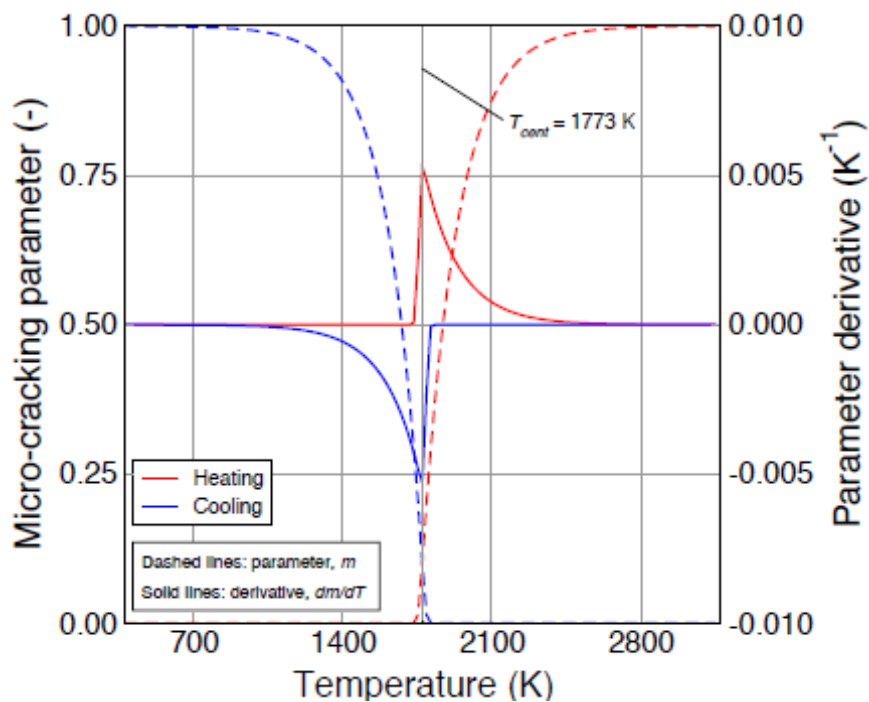


Figure 16: Micro-cracking parameter for BISON code tFGR model [78]

In the SCIANTIX code, non-diffusional (transient) gas release uses a semi-empiric model based on grain separation from fuel microcracking [72]. This work is based on prior work in BISON and TRANSURANUS [36]. The implementation is described in the prior paragraph describing the model implementation in TRANSURANUS, as well as in Figure 16 above. The OFFBEAT fuel solver also uses these models, as it uses the SCIANTIX code package to calculate fission gas release [70].

Non-FGR Modeling Improvements

Several enhancements are proposed to CTF that are not directly related to the main focus of FGR modeling. These enhancements aim to improve the accuracy of CTF or to increase its range of applicability. They also include the addition of several quantities of interest (QOIs) to be either calculated or printed within CTF. The enhancements proposed are the inclusion of additional post-CHF (Critical Heat Flux) heat transfer models, accurate enthalpy calculations in CTF, and the printing of several additional QOIs for fuel performance purposes.

In an RIA, the cladding temperature increases sufficiently to cause DNB. To properly model this, CTF includes a robust post-CHF heat transfer algorithm which accounts for four different types of heat transfer regimes. The selection algorithm for the default heat transfer regime in CTF can be found in Figure 17. To investigate its accuracy, two post-CHF correlations are implemented in CTF. The models selected for implementation are the Bishop-Sandberg-Tong [79] correlation and the Condie-Bengston-IV [80] correlation. These correlations span a large range of values and replace the DFFB (Dispersed Droplet Deposition Heat Transfer), TRAN (Transition Boiling), IAFB (Inverted Annular Film Boiling), and IADF (Dispersed Droplet Film Boiling) heat transfer regimes with a single post-CHF regime. The equation for the Bishop-Sandberg-Tong is shown below with the range of applicability. It uses units of $\frac{Btu}{hr-ft^2-^{\circ}F}$.

$$\left(\frac{h_{BST}D_e}{k}\right)_f = 0.0193 \left(\frac{D_e G}{\mu}\right)_f^{0.80} \left(\frac{c_p \mu}{k}\right)_f^{1.23} \left(\frac{\rho_v}{\rho_{bulk}}\right)^{0.68} \left(\frac{\rho_v}{\rho_{sat}}\right)^{0.068} \quad \text{EQ 71}$$

Where:

$$T_f = \frac{T_w + T_{bulk}}{2} \quad \text{EQ 72}$$

$$0.11 \times 10^6 < q'' < 0.61 \times 10^6 \frac{Btu}{hr - ft^2}$$

$$0.88 \times 10^6 < G < 2.5 \times 10^6 \frac{lbm}{hr - ft^2}$$

$$580 < p < 3190 \text{ psia}$$

$$0.10 < D_e < 0.32 \text{ in}$$

$$483 < T_{bulk} < 705 \text{ }^\circ F$$

$$658 < T_w < 1109 \text{ }^\circ F$$

The Condie-Bengson-IV correlation equation is shown below along with the range of applicability. The heat transfer coefficient is calculated in units of $\frac{kW}{m^2-K}$. CTF uses default British units, so a unit conversion is required; however, parameter ranges are shown here in imperial units and not metric units.

$$h_{CB4} = \frac{q''_{CB4}}{T_w - T_{bulk}} \quad \text{EQ 73}$$

$$q''_{CB4} = 0.00128 \frac{k_g^{0.4593} Pr_w^{2.2598}}{D_e^{0.8095} (1+x)^{2.0514}} \times Re_g^{[0.6249 + 0.2043 \ln(x+1)]} (T_w - T_{sat}) \quad \text{EQ 74}$$

$$1.08 \times 10^4 < q'' < 6.58 \times 10^5 \frac{Btu}{hr - ft^2}$$

$$1.22 \times 10^4 < G < 3.86 \times 10^6 \frac{lbm}{hr - ft^2}$$

$$61 < p < 3117 \text{ psia}$$

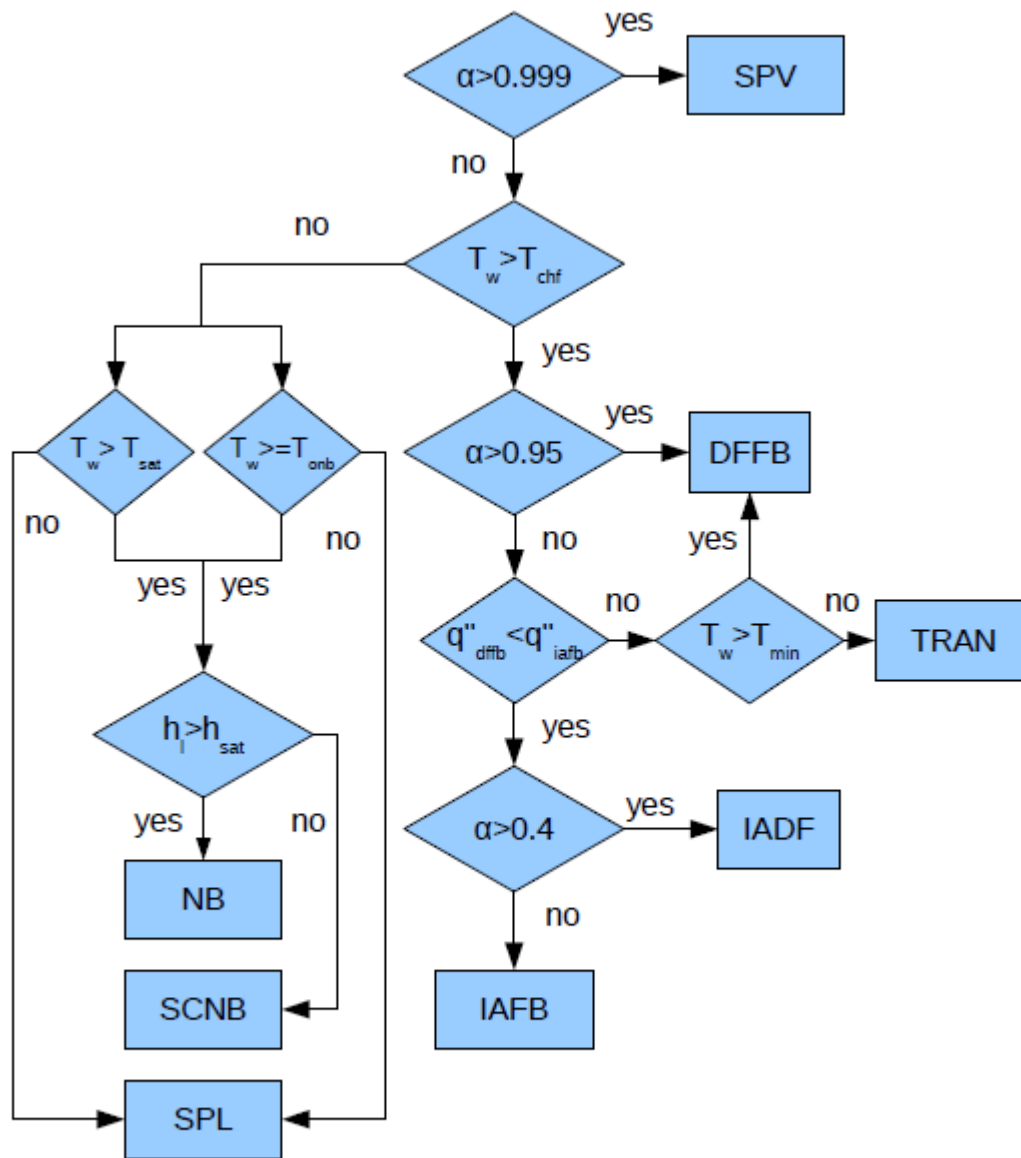


Figure 17: CTF Selection Algorithm for Heat Transfer Regime [3]

An additional improvement to the enthalpy calculation accuracy in CTF is desired. To improve accuracy, the material specific MATPRO-11 formulation for fuel enthalpy for uranium dioxide is implemented in CTF, as well as an investigation in the current numerical implementation

in CTF. The equation for fuel enthalpy according to MATPRO-11 was submitted to the U.S. NRC in a report [81] amending the original MATPRO-11 handbook [48]. The enthalpy calculated according to the equation below is calculated in $\frac{J}{g}$, where the temperature is input in Kelvin, the universal gas constant R is taken to be $8.3143 \frac{J}{mol-K}$. The oxygen-to-metal ratio Y is equal to 2 for uranium dioxide. The material specific constants can be found in Table 7.

$$h = \frac{K_1 \theta}{\exp\left(\frac{\theta}{T}\right) - 1} + \frac{K_2 T^2}{2} + \frac{Y}{2} K_3 \exp\left(-\frac{E_D}{RT}\right) \quad \text{EQ 75}$$

Table 7: MATPRO-11 Fuel Enthalpy Constants

Constant	UO_2	PuO_2	Units
K_1	296.7	347.4	$\frac{J}{kg - K}$
K_2	2.43×10^{-2}	3.95×10^{-4}	$\frac{J}{kg - K^2}$
K_3	8.745×10^7	3.860×10^7	$\frac{J}{kg}$
θ	535.285	571.0	K
E_D	1.577×10^5	1.967×10^5	$\frac{J}{mol}$

Additional QOIs added to the CTF HDF5 output include the fuel enthalpy, gap gas pressure, fuel hoop stress, and total hoop strain in the fuel pellet. These quantities are already

calculated in CTF but not output. Adding additional output QOIs such as the above permits the code user to obtain valuable data concerning fuel rod status during simulations.

CHAPTER 5 – Model Implementation and Test Cases

Introduction

Various models exist for calculating fission gas concentrations and releases. Steady state models are built using diffusion-based methodologies whereas the transient FGR models vary more, with some models choosing simpler temperature-based release criteria while others select a more rigorous approach using stress-based release criteria. Two models, a steady state and a transient model, are selected for implementation in CTF to aid in the extension of the code fuel rod modeling capabilities to high burnup and enrichment. The models selected are the FRAPCON steady state FGR model (denoted as the FRAPFGR model) and the FRAPTRAN transient FGR model. These models are selected for several reasons including model accuracy, licensing of codes by regulatory agencies, and compatibility with the existing CTF code infrastructure.

The selection of both FRAPCON and FRAPTRAN models for CTF implementation is significant for several reasons. FRAPCON and FRAPTRAN are both U.S. NRC approved codes. This lends a strong degree of validity to their modeling approach and shows these models are accurate, yet conservative enough to be used to validate existing nuclear reactors. In addition, much of the fuel rod modeling and dynamic gap conductance modeling already present in CTF is taken from the FRAPCON and FRAPTRAN codes. This allows a higher degree of compatibility between the source code, to the point that the insertion of additional models from FRAP within the CTF algorithm is simpler than other models considered in Chapter 4.

The compatibility of the models is also significant. While a microstructure-based model such as the FALCON FGR model is likely to be the most precise and accurate modeling methodology, CTF does not have the capabilities to model the fuel microstructure to the extent required to implement that model. Consequently, the models selected for use in CTF must either

take as input quantities that are already calculated in CTF or those that can readily be made available through the addition of smaller submodels. For the steady state FGR implementation, the diffusion-based process described by the Booth model [62] and adapted by various papers and codes (Speight [67], Forsberg and Massih [63], TRANSURANUS [66], etc.) uses many of quantities already required by CTF and submodels are available as part of FRAPCON for quantities such as grain size changes and gaseous atomic diffusion coefficients that are not currently available in CTF. The model was previously implemented in CTF in a previous work [82] and will serve as a basis for transient FGR implementation.

Details of the steady state FRAPFGR and the transient FRAPTRAN model implementations in CTF are provided in this section, including the models and submodels included in the updated code. An overview of the selected test cases for model verification in CTF is also included, as well as the test plan for verification of the steady state and transient FGR model implementations. Chapter 6 contains an in-depth analysis of verification runs performed between CTFFuel and FRAPCON.

CTF Steady State FGR Implementation

As mentioned in Chapter 4, the FRAPFGR model is a modification of the Modified Forsberg Massih model that allows further variation of grain size and diffusion coefficients, as well as changes to low power, high burnup cases. In summary, an integro-differential equation is derived by Forsberg and Massih [63] to describe the density of gas particles, incorporating time-dependent boundary conditions. A formal solution is obtained on a grain boundary, with analytical expressions for grain boundary concentration in steady state calculations. This solution is solved numerically to assess gas atom accumulation at the grain boundary, using grain and grain boundary saturation as the release criterion. The complete set of equations implemented in CTF can be found

in related works [63] [30] [44] [64] [83]. The general rate equation appears in Equations 76 and 77, where $C(r, t)$ represents the gas atom concentration at a grain surface, $D(t)$ is the diffusion coefficient, and β denotes the gas production rate. A suggested numerical treatment for this model is outlined in the appendix of Forsberg and Massih's 1985 work [63]. The full implementation from FRAPCON utilized in CTF is detailed by Geelhood et al. [44] in Equations 2.151 to 2.155, and included in Appendix A. For low-temperature, high-burnup cases, Equations 78 and 79 include an adjustment where F represents the fission gas release fraction. The saturation area density N_s and grain boundary saturation concentration gs are provided in Equations 80 and 81, where a is the grain size is, and r , set at 0.5 microns, is the radius of the gas bubble. The bubble surface tension γ is equal to $0.6 \frac{J}{m^2}$ and $V_c = 0.25$ is the critical area coverage fraction. The dihedral half angle $\theta = 50^\circ$ and the equation for $F(\theta)$ is found in Equation 82. The external pressure, which here is the rod internal pressure, is P_{ext} in Pascals.

$$\frac{\partial C(r,t)}{\partial t} = D(t)\Delta_r C(r, t) + \beta(t) \quad \text{EQ 76}$$

$$\Delta_r = \frac{\partial^2}{\partial r^2} + \frac{2}{r} \frac{\partial}{\partial r} \quad \text{EQ 77}$$

$$F = 7 \times 10^{-5} BU + C \quad \text{EQ 78}$$

$$C = \left\{ \begin{array}{l} 0, BU \leq 40 \frac{GWd}{MTU} \\ \frac{0.01(BU-40)}{10}, BU > 40 \frac{GWd}{MTU} \ \& \ F \leq 0.05 \end{array} \right\} \quad \text{EQ 79}$$

$$N_s = \left[\frac{4rF(\theta)V_c}{3K_B T \sin^2(\theta)} \right] \left(\frac{2\gamma}{r} + P_{ext} \right) \quad \text{EQ 80}$$

$$gs = \frac{3N_s}{2a} \quad \text{EQ 81}$$

$$F(\theta) = 1 - 1.5 \cos(\theta) + 0.5 \cos^3(\theta) \quad \text{EQ 82}$$

This model was further modified by PNNL to improve radial gas distribution predictions and handle very high burnup cases (over 70 GWd/MTU) [84]. Specifically, the diffusion coefficient calculation was revised from the original Forsberg and Massih model. The updated diffusion coefficient can be found in Equations 83–87, extending applicability across a wider temperature range and altering the burnup impact on the diffusion coefficient. Equation 88 details this adjustment, with the burnup limited to a maximum of 49.81 GWd/MTU [44]. Additionally, PNNL introduced a reduction in gas release to account for gas resolution [44]. Lower power effects on the diffusion constant are also addressed in Equation 89, where Pow is the local radial node power in kW/ft.

$$D(t) = 1.15 \times 10^{-23}, T < 675 \text{ K} \quad \text{EQ 83}$$

$$D(t) = 1.15 \times 10^{-17} \exp\left(-\frac{9508}{T}\right), 675 \text{ K} < T < 1381 \text{ K} \quad \text{EQ 84}$$

$$D(t) = 2.14 \times 10^{-13} \exp\left(-\frac{22884}{T}\right), 1381 \text{ K} < T < 1650 \text{ K} \quad \text{EQ 85}$$

$$D(t) = 7.14433 \times 10^{-10} \exp\left(-\frac{34879}{T}\right), 1650 \text{ K} < T < 1850 \text{ K} \quad \text{EQ 86}$$

$$D(t) = 4.63 \times 10^{-18}, T > 1850 \text{ K} \quad \text{EQ 87}$$

$$D(T, \text{Bu}) = D(T) \cdot \left(10^{\frac{\max(\text{Bu}-21, 0)}{40}} + 10 \cdot \left(\frac{\min(\text{Bu}, 12)}{12}\right)\right) \quad \text{EQ 88}$$

$$D(T, \text{Bu}, \text{Pow}) = \frac{D(T, \text{Bu})}{2.5 - 1.5 \operatorname{erf}(\text{Pow} - 3)} \quad \text{EQ 89}$$

A new model simulating grain growth is also implemented to account for recrystallization under irradiation and thermal loading. The Khoruzhii grain growth model refines earlier models to better predict growth slowdown due to irradiation and related factors [64]. This improvement

prevents overprediction of grain growth, enhancing accuracy. The core equations for grain growth appear in Equations 90, 91, and 92, where $\frac{da}{dt}$ is the grain boundary migration rate, a_{max} is the non-irradiated maximum grain size, and a_{ir} is the irradiated maximum grain size. Model parameters A and E are empirically derived, while $T_0 = 1400$ K and $F_0 = 50$ MW/tU. In CTF, $A=326.5$ and $E=5620$ are adopted, aligning with values in comparable fuel performance models [1].

$$\frac{da}{dt} = K \left(\frac{1}{a} - \frac{a}{a_{maxi}} - \frac{1}{a_{ir}} \right) \quad \text{EQ 90}$$

$$a_{ir} = \left[\frac{F_0 \cdot T_0}{F_0 \cdot T} \right] A \exp \left(-\frac{E}{T} \right) \mu\text{m} \quad \text{EQ 91}$$

$$a_{max} = 2.23 \times 1063 \exp \left(-\frac{7620}{T} \right) \mu\text{m} \quad \text{EQ 92}$$

Moreover, the HBS model derives from electron microscopy and probe analysis by Manzel and Walker [83]. Equation 93 calculates the high burnup rim thickness, comprising fully restructured grains. An adjacent region, equal in thickness, contains a mix of fully and partially restructured grains, with restructured grain fraction increasing linearly. Restructuration is absent if a node's temperature exceeds 1000°C. The rim thickness is based on average pellet burnup rather than nodal burnup. The associated porosity increase is factored into gas production calculations for local burnup below 57 GWd/MTU. This is shown in Equation 94.

$$t_{rim} = 1.439 \times 10^{-6} \cdot \text{BU}^{4.427} \quad \text{EQ 93}$$

$$P = 11.283 \ln(\text{BU}_{local}) - 45.621 \quad \text{EQ 94}$$

The fission gas release percentage varies based on prior grain saturation. For a first-time exceedance of the saturation value in a radial node, 65% of the saturation gas is retained, with excess released thereafter. Total gas release for nodes with both structured and unstructured grains

is calculated with Equation 95, where *rest* is the restructured grain fraction, and Δrel_1 and Δrel_2 represent releases from restructured and unstructured grains, respectively.

$$\Delta_{tot} = \Delta rel_1(rest^2) + \Delta rel_2(1 - rest^2) \quad \text{EQ 95}$$

Finally, an additional burnup enhancement factor, following the ANS5.4-2011 standard [85], is included in CTF. This factor, tailored for high burnup, is calculated using Equation 96 and applied before the diffusion coefficient adjustment in Equation 79.

$$D(T, Bu, Pow) = \begin{cases} D \max \left(1, - (2.54132E - 7)Bu^4 + (3.91491E - 5)Bu^3 + \right. \\ \left. .023278Bu^2 - 3.92956Bu + 156.649 \right), BU \leq 90 \frac{GWd}{MTU} \\ D(0.0084Bu + 0.2523), BU > 90 \frac{GWd}{MTU} \end{cases} \quad \text{EQ 96}$$

These equations constitute the major equations for the FRAPFGR steady state FGR model as have been implemented in CTF. This implementation and a brief verification are detailed in prior work by Abarca, Ivanov, and Avramova [82]. A full verification is planned as part of this project against the FRAPCON fuel performance code. Another change performed to CTF is a change in radial nodalization. As a default, CTF uses an equi-distant radial nodalization, where radial nodes are the same distance from one another. This leads to accurate temperature predictions and is the default for calculation of heat transfer in solids. For fission gas calculations, the distribution of gases is focused in the outer rim of the fuel, due to the HBS and other factors. Increasing radial resolution in that area of the fuel yields more accurate fission gas concentrations calculations. As such, at the sacrifice of some accuracy in the temperature prediction, particularly at the fuel axial centerline, an equi-areal radial nodalization is implemented in CTF to increase the accuracy of the FGR calculation.

CTF Transient Implementation

For the transient model implemented, the two options of low fidelity temperature or enthalpy-based limits and microcracking based methodologies exist. However, the limitations effectively mean that without significant changes, microcracking based models for tFGR cannot be implemented in CTF, as CTF lacks the specific capacities to model cracking in the fuel solid at a sufficient resolution that grain boundary tunneling is accounted for. As a result, the tFGR model selected for implementation must be a lower resolution. This results in the selection of a temperature or enthalpy limit based empirical model, such as the FRAPTRAN model [74] or NRC model [42]. The FRAPTRAN model is selected for the same reasons as the FRAPCON model is selected for, namely the compatibility with the existing code infrastructure as well as its' use by the NRC for licensing purposes.

The FRAPTRAN model is described briefly in Chapter 4 but is also included here for completeness. It can be found in Figure 15, while a proposed FGR algorithm is shown in Figure 18 below, where fgr.ctf is an output file that contains a gas concentration matrix for the fuel pellet. This file can either be generated automatically using CTF to model a steady state depletion with the fission gas flag activated or produced by preprocessing code from a fuel performance code output. Currently, only the FRAPCON fuel performance code and CTF can produce this file in the correct format.

The FRAPTRAN tFGR model is an empirical model that calculates fission gas release quantities based on nodal temperature and general grain structure. Based on the current nodal temperature and whether the fuel grains have restructured during the prior power history, the FRAPTRAN tFGR model can determine how much gas is released, remains stored in the grain

boundary, and remains stored in intra-granular sinks. This model must be informed by a depletion calculation that provides the axial and radial distributions of fission gases in both grain boundaries and intra-granular sinks, as well as what percentage of the fuel grains at a given axial and radial node have restructured. This grain structure quantification can be calculated by EQ 88 and EQ 89, and gas grain and grain boundary concentrations can be calculated by any number of fuel performance codes.

In CTF, this model is coded to accept input from the “fgr.ctf” external input file. This file, which has been briefly described in the CTF Steady State FGR Implementation section, contains the gas concentrations at grain boundaries and intra-granular sinks, as well as the total fission gas produced in the rod. The input file set-up for this file is described in Appendix A. Once the fission gas concentrations are known and saved in CTF, the release criteria are examined. The tFGR model logic can be found in Figure 19 below. The flowchart allows for ease of reading and considers nodal temperature and grain structure.

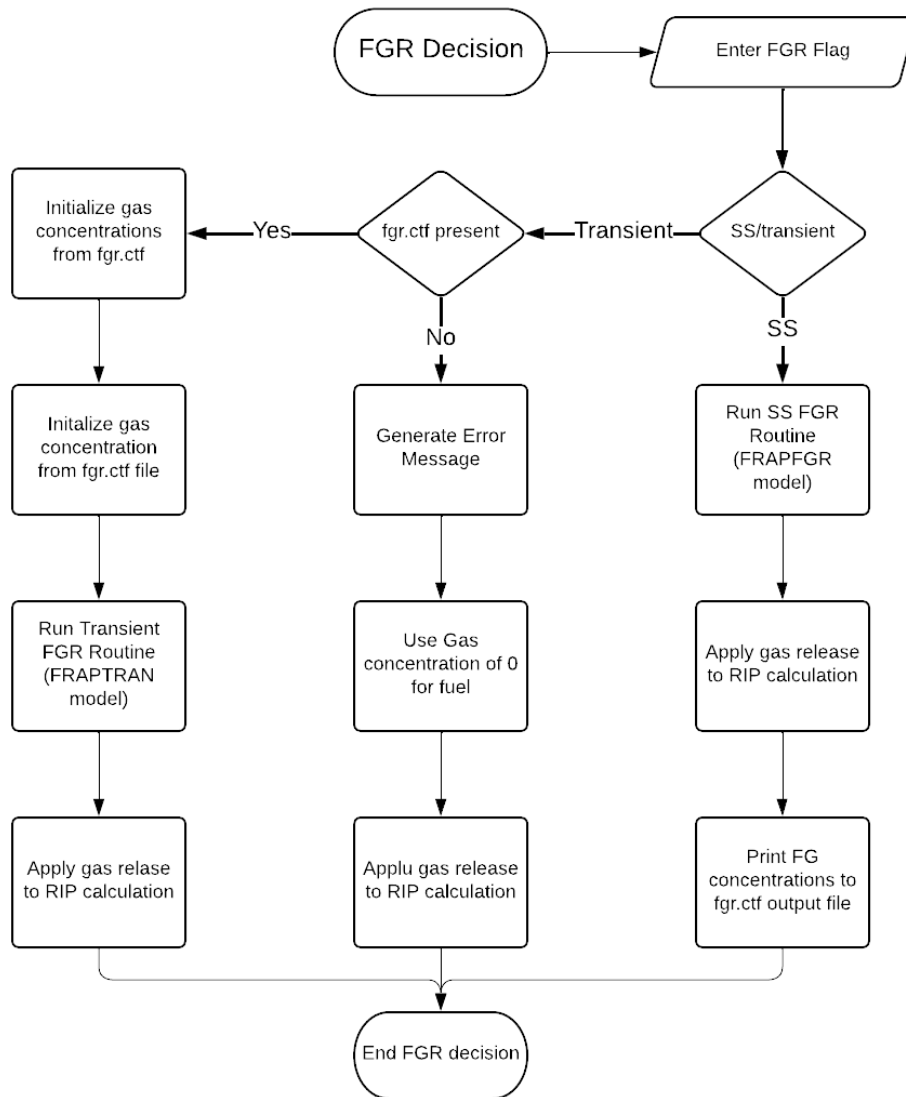


Figure 18: Proposed CTF FGR Algorithm

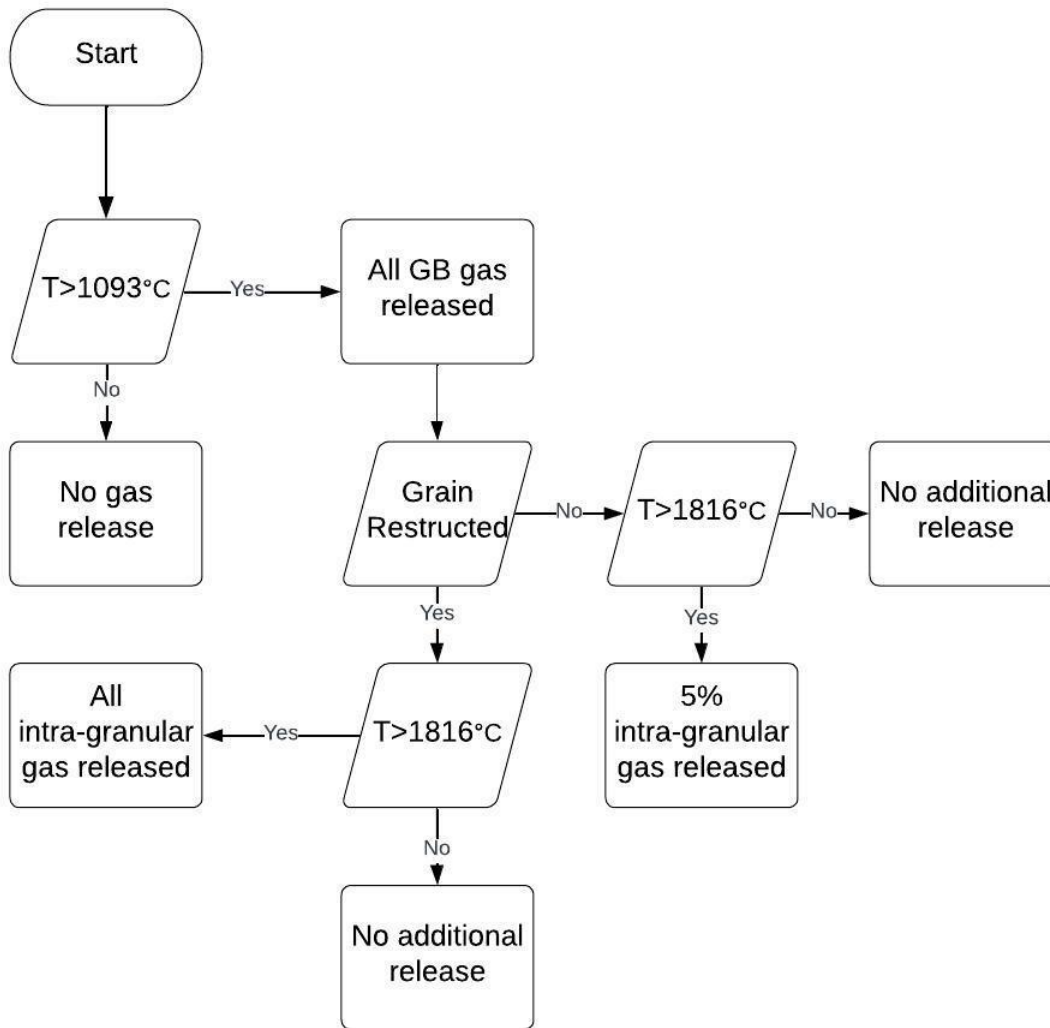


Figure 19: FRAPTRAN tFGR Model Logic and Release

Test Case Description

Test cases selected for verification of the steady state and transient model implementations are taken from two sources. A code-to-code verification between CTFFuel and FRAPCON is performed to verify the steady state model implementation. To verify the transient model implementation, a code-to-code verification between CTFFuel and FRAPTRAN is conducted,

with both codes informed by steady state fission gas concentrations calculated by FRAPCON. The FRAPCON calculated concentrations are used to test the performance of the transient model implementation only and not the performance of joint steady state and transient FGR model implementations in CTF. Following the conclusion of this test, the joint steady state and transient model implementation in CTF is compared to joint FRAPCON/FRAPTRAN cases. Simulation of the full power history and transient event for a single test will evaluate the performance of CTF with respect to full transient calculations. Additional test cases were run using the High Burnup in Reactivity Insertion Accidents (HERA) M&S Part 1 [86] Test cases to examine CTF's accuracy in simulating RIA type events. HERA is a Joint Experimental Program (JEEP) conducted under the NEA's Framework for Irradiation Experiments (FIDES). The HERA project aims to study LWR behavior under RIA conditions. The Modeling and Simulation (M&S) component of HERA is designed to simulate experiments performed by the INL and the Japan Atomic Energy Agency (JAEA) [87].

The test cases used to verify and validate the steady state FRAPFGR model implementation in CTF are the same as used in the FRAPCON-4.0 integral assessment [1]. These tests are used as the experimental information is publicly available and FRAPCON results are available as part of the report. These cases model fuel rod depletions for single rods where to power is maintained at roughly steady state levels, simulating normal operating conditions. The fuel rods are all comprised of uranium dioxide fuel with varying levels of enrichment from 3.0 to 13.0 wt% U-235 and rod-averaged burnups from 2.65 GWd/MTU to 98.9 GWd/MTU. This large range of enrichment and burnup values tests the full capability of the FGR model as implemented in CTF. The list of test cases for the code-to-code verification between CTFFuel and FRAPCON is found in Table 8 below.

The FRAPCON integral assessment is the second half of a two part document, where Part one describes the code itself [44] and serves as the theory manual and Part two describes the validation and assessment of its' capabilities [1]. The same is true for FRAPTRAN as well, with Part one of the codes' documentation describing the models [74] and Part two the assessment of its capabilities [2]. The assessments provide several FGR and tFGR cases based on experimental data. A general overview of the results taken from the integral assessment for the FRAPCON tests is provided in Table 8. Each of these cases will be simulated using a CTF steady state calculation and the results of the integral FGR will be compared to the FRAPCON-4.0 prediction. An informal analysis and comparison to the experimental values will be included, but the main objective of these tests is to demonstrate an accurate implementation of the FGR model.

Table 8: Steady State FGR Validation Cases

Test Case	Burnup (GWd/MTU)	Enrichment (wt%)	Test Case	Burnup (GWd/MTU)	Enrichment (wt%)
24i6	60.1	6.42	332	56.8	6.6
36i8	61.5	8.53	EPL-4	10.4	2.4
111i5	48.6	5.2	CBR	2.7	4.5
28i6	53.3	6.42	CBY	2.65	4.5
BNFL-DE	42.0	8.9	BNFL-DH	33.9	9.0
LFF	3.29	2.4	IFA 597.3	70.0	3.35
CBP	2.61	4.5	IFA 429-DH	98.9	13.0
4110-ae2	6.2	2.98	Oconee 15309	50.0	3.0
4110-be2	6.6	2.98			

In modeling the FRAPCON integral assessment test cases, all attempts were taken to mimic the FRAPCON modeling conditions as much as possible. The fuel modeling options in CTF found in Table 3 and Table 4 were taken to be the same options as used in the FRAPCON simulation to reduce potential sources of error in the simulation. A listing of the fuel models used in the CTF fuel simulations for the steady state FGR validation test suite is found in Table 9 below. The FRAPCON creep model that is found in the FRACAS-1 subroutine within FRAPCON is not implemented in CTF, so the ESCORE cladding creep model is used as an alternative. The Modified NFI fuel thermal conductivity model is the default fuel thermal conductivity model used in FRAPCON.

Table 9: CTFFuel Modeling Options

Fuel Phenomenon Modeled	Model Selected
Solid Fuel Swelling	FRACAS-1
Gaseous Fuel Swelling	FRACAS-1
Fuel Densification	FRACAS-1
Cladding Creep	ESCORE Model
Fuel Relocation	FRACAS-1
Fuel Thermal Expansion	FRACAS-1
Fuel Thermal Conductivity	Modified NFI Model

Similarly to FRAPCON, an integral assessment [2] was also performed for the FRAPTRAN fuel performance code. The test cases used in that integral assessment to test FRAPTRAN's FGR behavior are suggested for verification and validation of the implemented tFGR model in CTF. A listing of the test cases is found in Table 10 below. They range in burnup from 26.6 to 66.0 GWd/MTU. These simulations were initially run with a base irradiation from FRAPCON. This generates a restart file that includes gas concentrations to initialize the FRAPTRAN model. The FRAPTRAN simulation is then run and the FGR during the transient is measured. There are two separate uses for these cases:

1. For transient model verification, a CTFFuel simulation is run for each test using the same FRAPCON fission gas concentrations as the FRAPTRAN test. This allows for a direct comparison of the performance of the implemented model via a comparison of the CTFFuel generated FGR values and the FRAPTRAN generated FGR values.

2. A test of the joint steady state and transient capabilities of CTF is proposed using the same test matrix. The depletion is run using CTF instead of FRAPCON to generate fission gas concentrations in the fuel. This is then used to inform a transient simulation for each test case and the resulting FGR values are compared to both experimental and FRAPTRAN produced values.

Part 1 of the HERA M&S simulation examines the effect of PCMI during RIA conditions and assesses the potential for failure. This part comprises 12 tests, as detailed in Table 11. below. Of these test cases, cases 1-5 were conducted by JAEA at the Nuclear Safety Research Reactor (NSRR), while cases 6-12 were conducted by INL at the Transient Reactor Test Facility (TREAT) facility. The capsules used by each reactor vary slightly, with differences listed in Table 12. The setup of both capsules is shown in Figure 20, with reactor setups identical aside from the dimensional differences noted in Table 12. The general experimental parameters can be found in Table 13.

Table 10: Transient FGR V&V Test Cases

Test Case	Burnup (GWd/MTU)	Reactor Type
CABRI NA2	66.0	BR-3
CABRI NA3	53.8	PWR 17x17
CABRI NA4	62.0	PWR 17x17
CABRI NA5	64.0	PWR 17x17
NSRR FK-1	45.3	BWR 10x10
NSRR GK-1	42.1	PWR 14x14
NSRR HBO-6	49.0	PWR 17x17
NSRR MH-3	38.9	PWR 14x14
NSRR OI-2	39.2	PWR 17x17
NSRR TS5	26.6	BWR 7x7

Table 11: HERA M&S Exercise Part 1 Test Matrix

Case #	Pulse Width at FWHM (ms)	Peak Radial Average Enthalpy Increase (J/g)	Hydrogen Content/Rim thickness (ppm/μm)
1	7.5	650	400/80
2	7.5	650	200/40
3	7.5	650	600/140
4	7.5	550	400/80
5	7.5	750	400/80
6	90	650	400/80
7	90	650	200/40
8	90	650	600/140
9	90	550	400/80
10	90	750	400/80
11	50	650	400/80
12	300	650	400/80

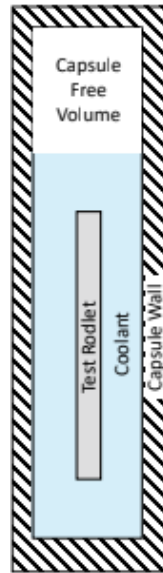


Figure 20: HERA M&S Exercise Part 1 Experimental Capsule

Table 12: Experimental Difference between TREAT and NSRR Facilities

Test Parameter	TREAT	NSRR
# of Fuel Pellets	10	12
Total Fuel Mass (g)	57.9	69.4
Rod Free volume (cc)	1.23	2.52
Water Outer Radius (mm)	25	60
Capsule Water Volume (cc)	280	6250
Capsule Argon Free Volume (cc)	500	2350

Table 13: HERA M&S Exercise Part 1 Experimental Parameters

Test Parameter	Value
Fuel Composition	Fresh UO ₂
Fuel Density (kg/m ³)	10475
Cladding Type	Zry-4, SRA
Fuel Outer Radius (mm)	4.1605
Fuel Pellet Height (mm)	10.160
Cladding Inner Radius (mm)	4.1785
Cladding Outer Radius (mm)	4.7500
Plenum Pressure (MPa @ 20°C)	0.1
Bulk Water Temperature (°C)	20
Capsule Pressure (MPa)	0.1

It is important to note that since CTF cannot model hydrogen or hydride distributions in the cladding, certain cases listed in Table 11 become redundant; without accounting for hydride thickness, they are identical to others. In this project, Cases 1, 2, and 3 are identical, as are Cases 6, 7, and 8. The HERA test cases are intended to be used to simulate the accuracy of CTF when calculating fuel performance QOIs such as fuel enthalpy, fuel and cladding temperature, and RIP.

CHAPTER 6 – Results

FRAPCON to CTFFuel

The results of the FRAPCON to CTFFuel comparison are found below. The experimental value of integral FGR is included for information purposes and not as a verification metric. The model implementation is verified solely against the FRAPCON FGR behavior, as a verification exercise. The Root Mean Square Error (RMSE) is used as a validation metric between the FRAPCON and CTFFuel. CTFFuel is used rather than running a full CTF simulation due to the presence of boundary conditions provided by FRAPCON. As these are provided at the cladding and not the coolant sub channel entrance, running the fluid solution portion of CTF would result in quantities that cannot be compared to other tests run in FRAPCON, as it does not calculate the fluid solution. Since the CTFFuel module is run during standard CTF runs using the nuclear fuel rod model, the results found using CTFFuel are expected to be the same as they would be in CTF.

The end of simulation (integral) FGR values for each test case are shown in Table 14 below. In the fifth column, the RMSE between the FRAPCON prediction and the CTFFuel prediction is included. This quantity is computed by comparing the FGR value at each state point output by the two codes, as the state points occur at the same time. The absolute error is the difference between the CTFFuel and FRAPCON predicted FGR at end-of-life. This can be compared to the experimental value for FGR, as only the end-of-life FGR is known for the experiments.

Table 14: FRAPCON vs. CTFFuel Integral Steady State FGR values

Rod Name:	Experimental FGR (%)	FRAPCON-4.0 Predicted FGR (%)	CTFFuel Predicted FGR (%)	RMSE (%)	Absolute Error (%)
24i6	21.8	22.7	26.69	NA	3.99
36i8	33.8	38.09	38.93	0.7986	0.48
111i5	14.4	14.79	16.31	3.9452	1.37
28i6	13.2	13.44	17.41	2.8413	4.14
BNFL-DE	10.7	10.24	10.6	3.6125	0.39
LFF	17.3	19.35	42.28	22.2332	23.13
CBP	14.1	14.51	32.66	18.9586	18.15
4110-ae2	22.1	16.56	36.82	16.3087	20.26
4110-be2	15.9	16.65	33.18	12.9003	16.53
332	20.9	17.24	28.23	5.7541	10.77
EPL-4	17.3	20.72	39.05	10.7140	18.33
CBR	14.1	15.58	34.70	19.9711	19.12
CBY	16.8	16.73	41.45	24.6358	24.72
BNFL-DH	20.0	15.73	18.82	7.3759	3.25
IFA 597.3	15.8	14.55	33.0	7.4282	18.45
IFA429DH	57.4	54.36	55.83	4.9241	2.04
Oconee 15309	0.8	1.25	4.32	2.0674	3.12

Initial results show good agreement between CTFFuel and FRAPCON, however several cases show significant overprediction by CTFFuel. The cases are highlighted in bold text in Table 14. These cases are mostly low burnup cases, and all have uniform axial power and burnup profiles. CTFFuel overpredicts the FGR in all cases. The time-dependent FGR values are shown in the Figures below. Each point on the graph is a printed state point for both CTFFuel and FRAPCON.

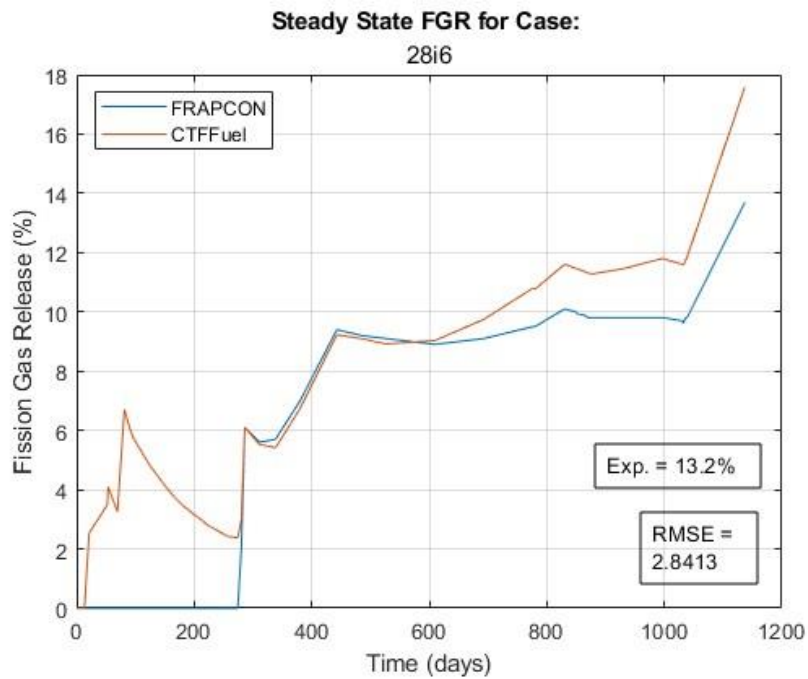


Figure 21: Case 28i6 Steady State Fission Gas Release

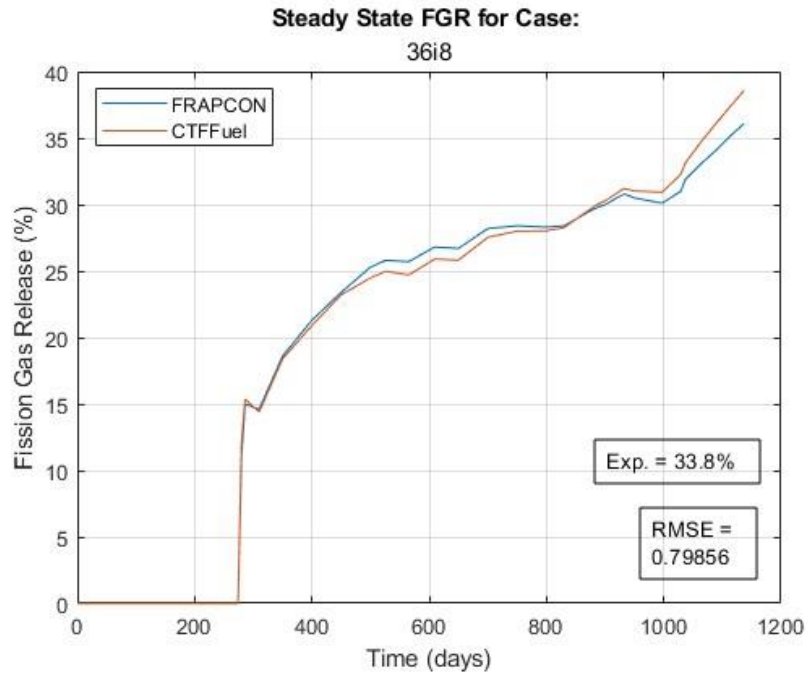


Figure 22: Case 36i8 Steady State Fission Gas Release

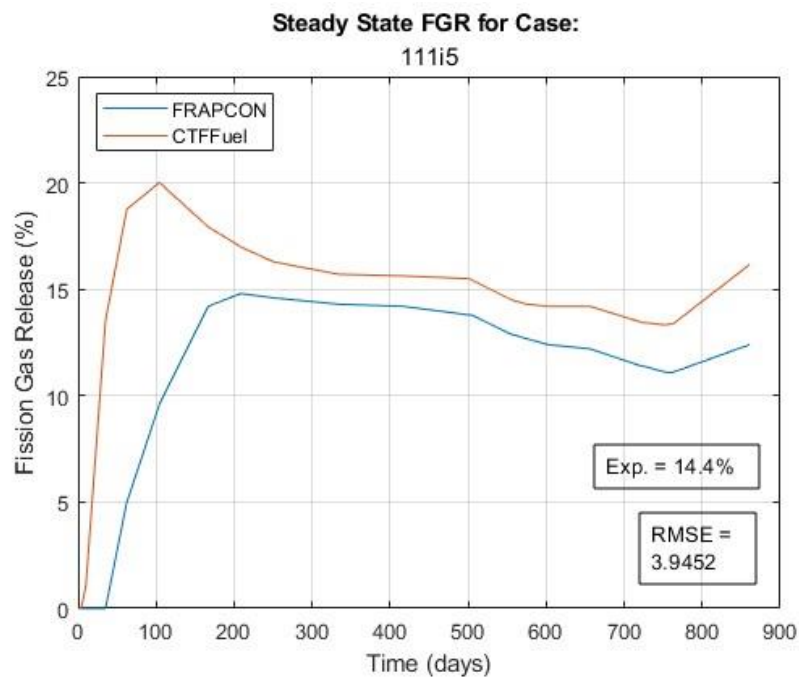


Figure 23: Case 111i5 Steady State Fission Gas Release

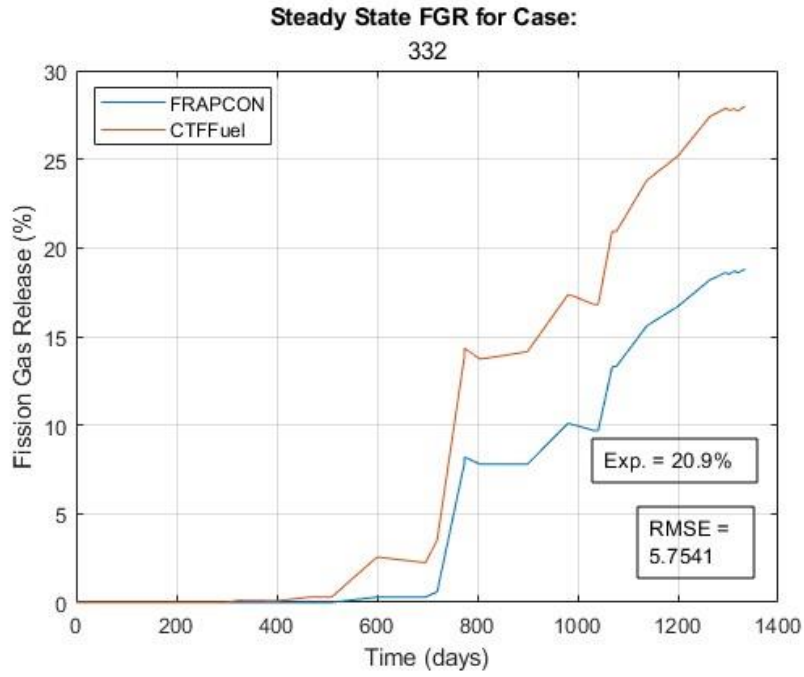


Figure 24: Case 332 Steady State Fission Gas Release

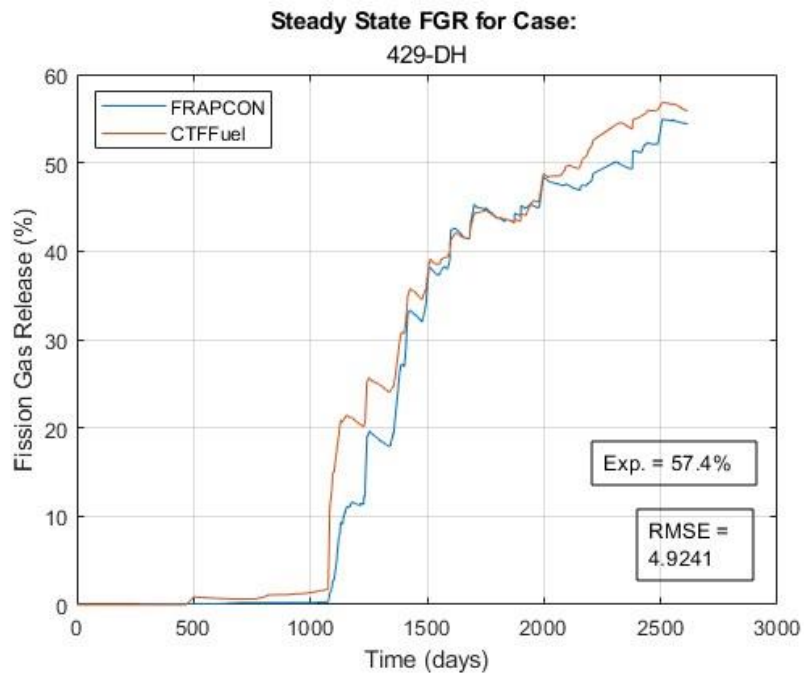


Figure 25: Case 429-DH Steady State Fission Gas Release

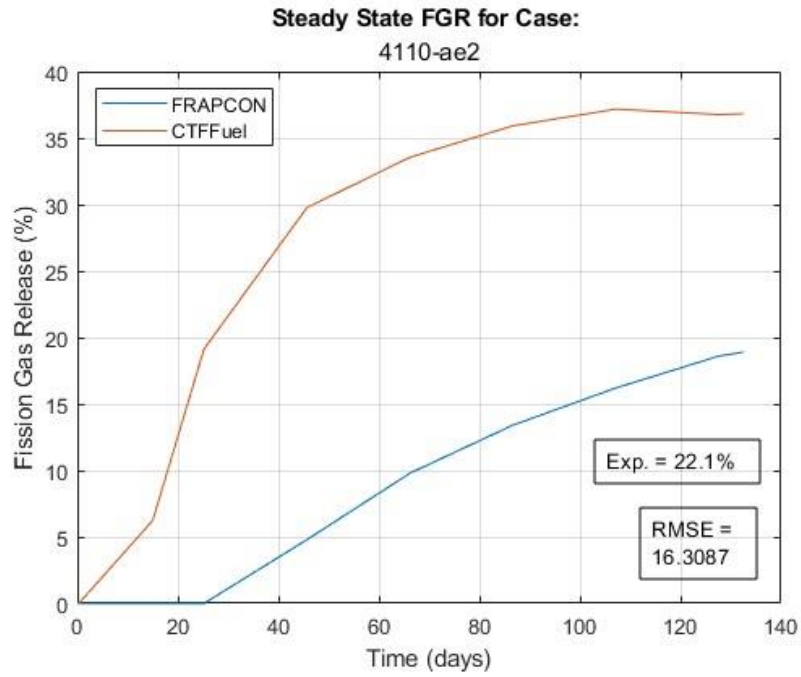


Figure 26: Case 4110-ae2 Steady State Fission Gas Release

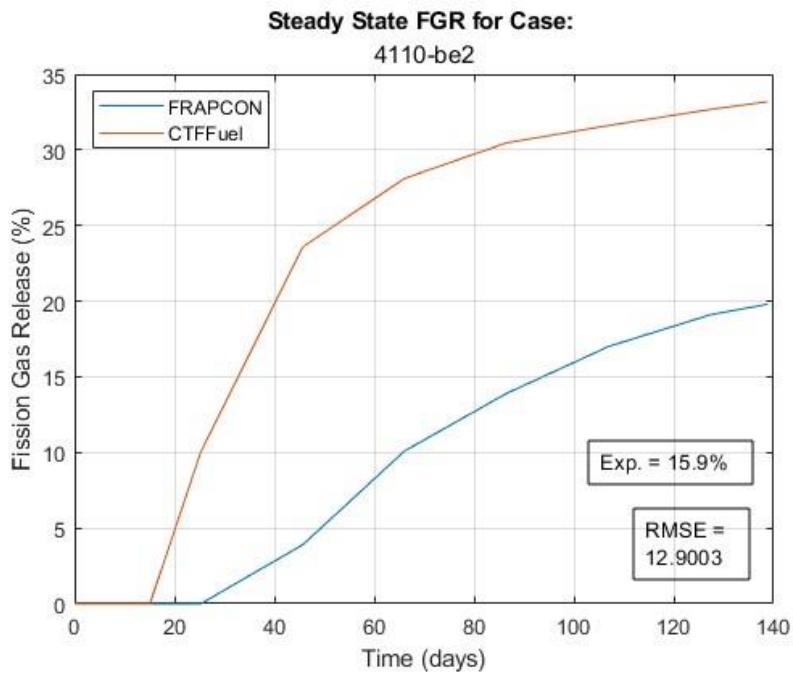


Figure 27: Case 4110-be2 Steady State Fission Gas Release

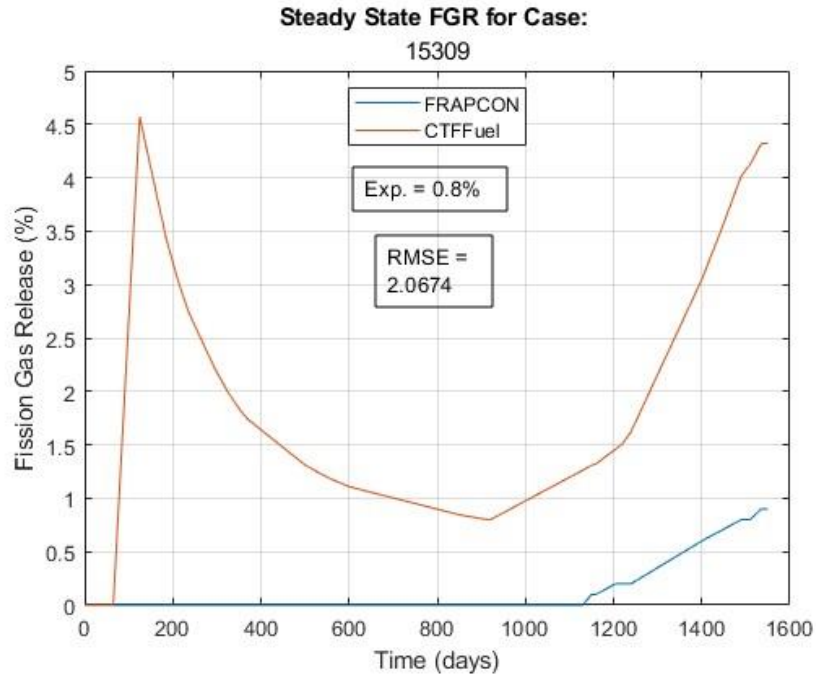


Figure 28: Case 15309 Steady State Fission Gas Release

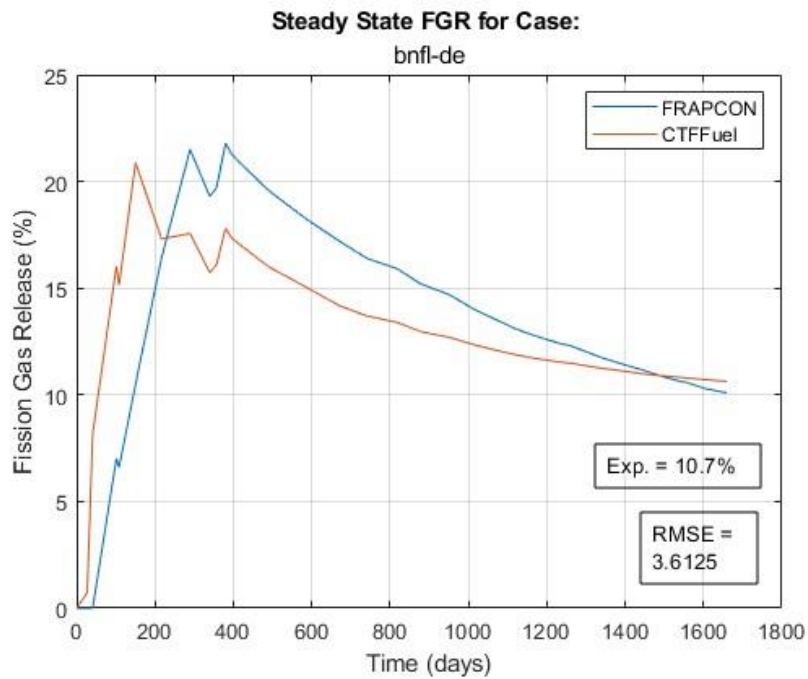


Figure 29: Case BNFL-DE Steady State Fission Gas Release

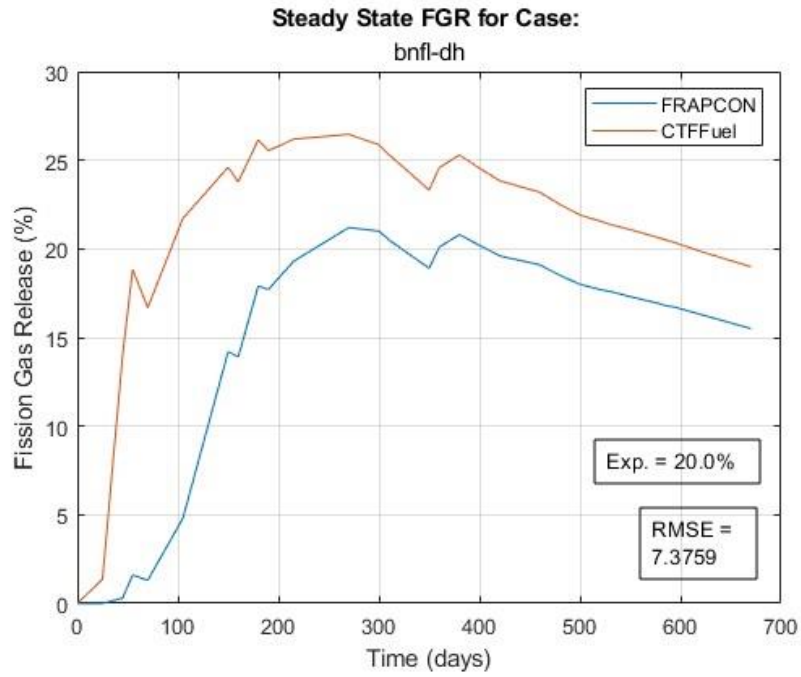


Figure 30: Case BNFL-DH Steady State Fission Gas Release

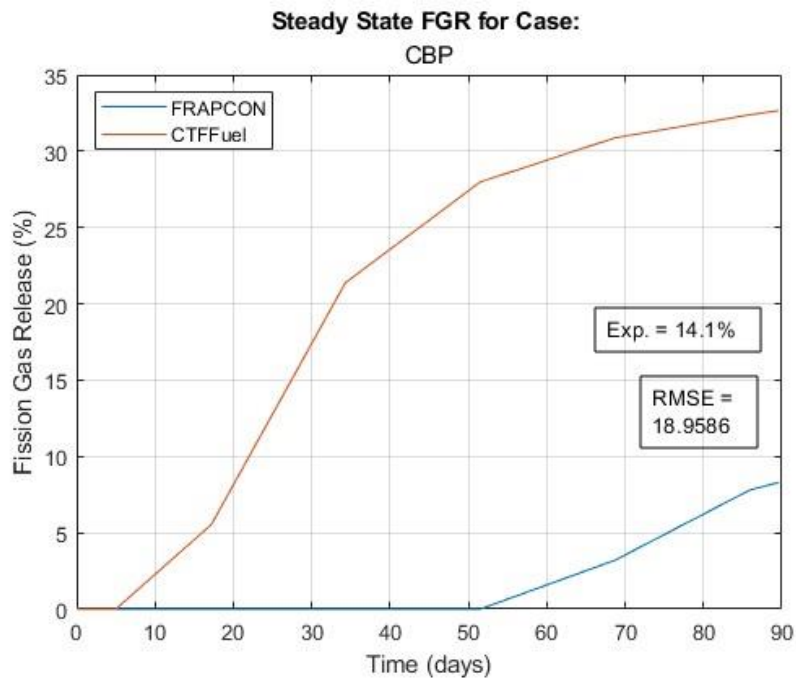


Figure 31: Case CBP Steady State Fission Gas Release

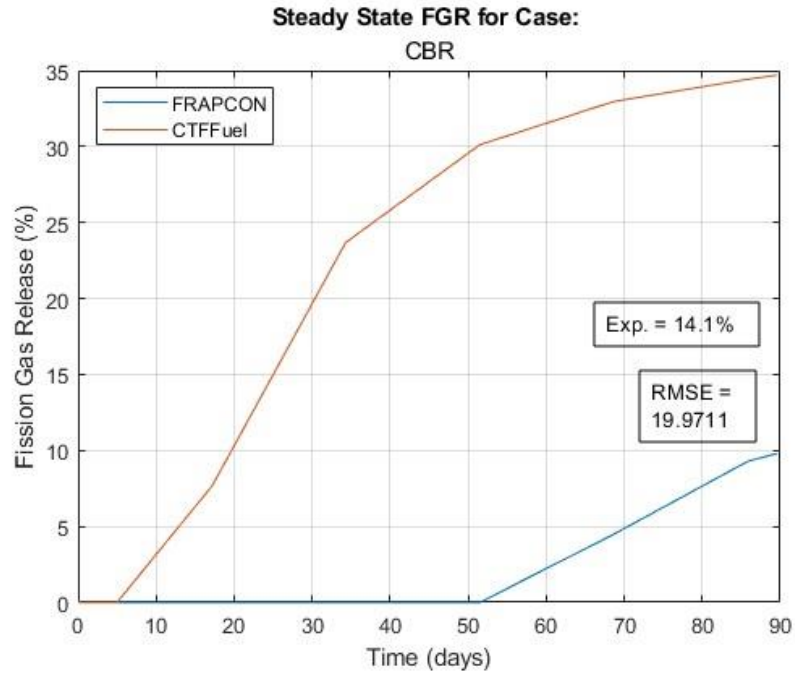


Figure 32: Case CBR Steady State Fission Gas Release

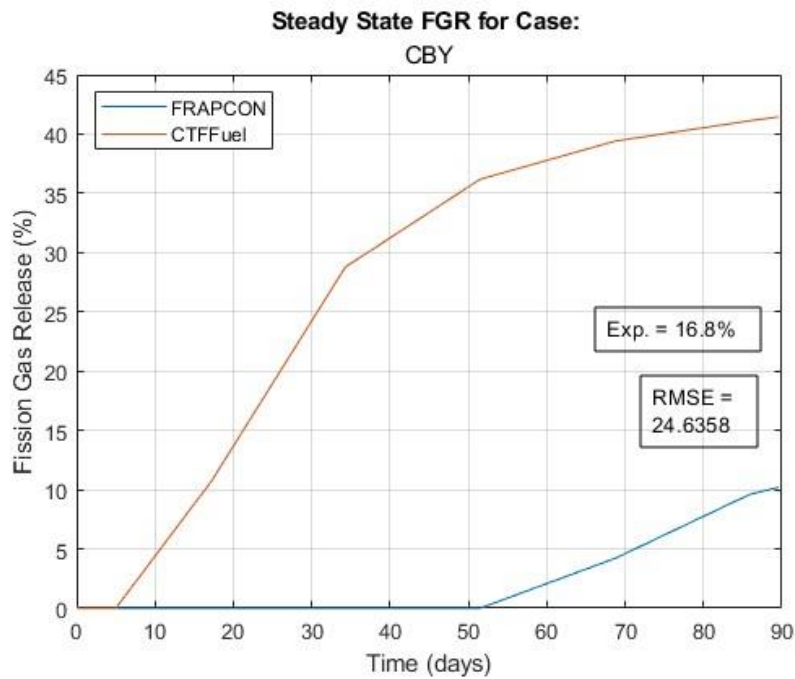


Figure 33: Case CBY Steady State Fission Gas Release

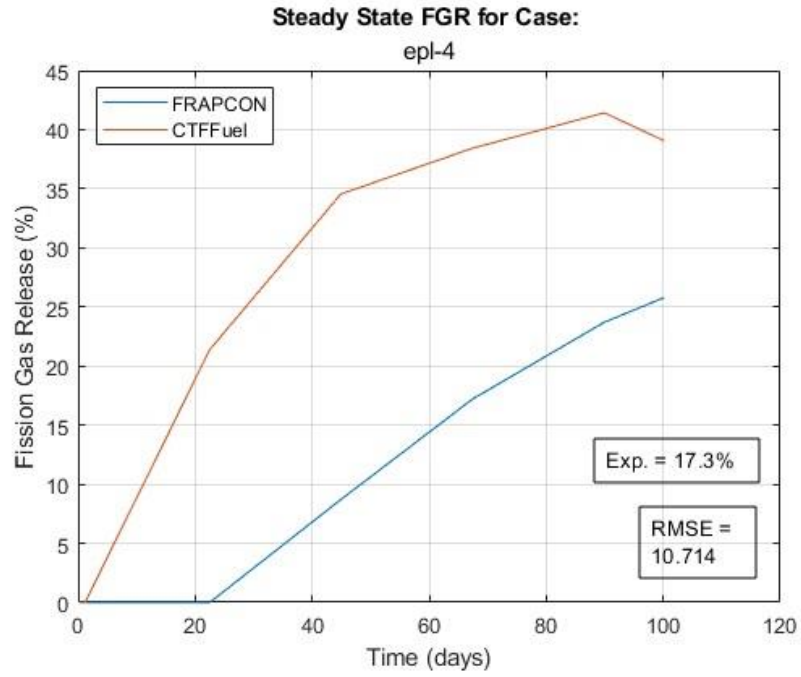


Figure 34: Case EPL-4 Steady State Fission Gas Release

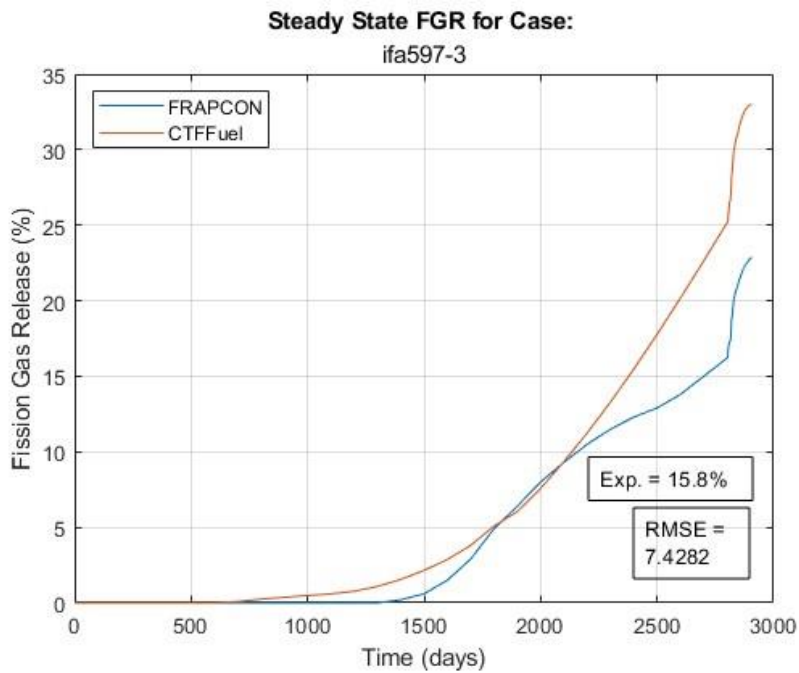


Figure 35: Case IFA597-3 Steady State Fission Gas Release

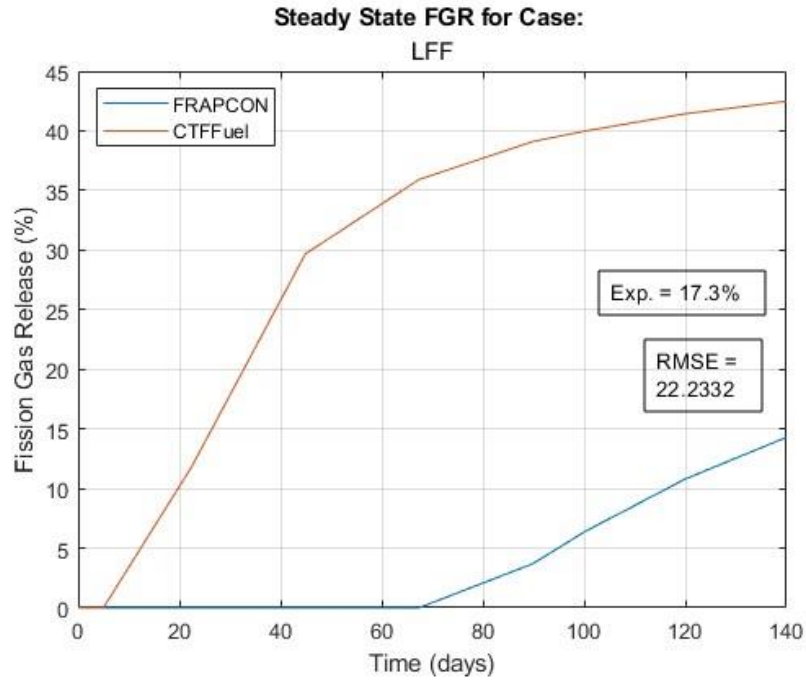


Figure 36: Case LFF Steady State Fission Gas Release

FRAPTRAN to CTFFuel

Following the tFGR model implementation, the transient test suite was conducted. Results show reasonable agreement compared to FRAPTRAN. The final FGR values for the transient test suite are shown in Table 15 below. The 0.0% prediction in Case FK-1 is taken to be an input error.

Table 15: tFGR Simulation Results

Test Case	Experimental FGR (%)	FRAPTRAN prediction (%)	CTFFuel Prediction (%)
CABRI NA2	5.54	5.59	3.6
CABRI NA3	13.7	12.31	10.66
CABRI NA4	8.3	10.02	9.23
CABRI NA5	15.1	18.84	12.24
NSRR FK-1	8.2	6.8	0.0
NSRR GK-1	12.8	6.2	6.14
NSRR HBO-6	10.4	8.45	5.18
NSRR MH-3	4.0	2.42	2.41
NSRR OI-2	10.2	4.53	6.82
NSRR TS5	8.0	1.65	5.99

HERA Sensitivity Study

A sensitivity study using the HERA Part 1 simulation test cases is run in CTFFuel, using provided cladding temperatures as boundary conditions. Prior participation in the HERA Part 1 benchmark [88] had resulted in unsatisfactory enthalpy predictions from CTF. An investigation led to the implementation of the implicit MATRPRO-11 enthalpy formulation. A verification comparing the CTF numerical formulation and MATPRO-11 implicit formulation yielded near identical enthalpy values, indicating an error in the numerical model implementation in CTF. This error was identified as an incorrect temperature conversion in the CTF algorithm and corrected.

These results led to the MATPRO-11 formulation matching the numerical approximation well and the implicit formulation not being included as an option in CTF.

The HERA M&S Benchmark Part 1 test cases were simulated in CTF using adiabatic conditions to test the energy deposition in CTF. The Total Energy Deposition (TDE) for each test case was manually calculated from the fuel geometry and the benchmark provided power profiles. It is noted that the manually calculated TDEs do not match the target enthalpy values for each case; this is due to the assumed heat transfer that leads to a peak Radial Average Enthalpy (RAE) lower than the TDE and closer to the target. The adiabatic tests were simulated with the lowest allowable gap heat transfer coefficient, forcing the heat generated to remain in the fuel. The results of this study are shown in Table 16. The HERA M&S Part 1 cases were subsequently simulated using the updated numerical enthalpy formulation, and the results shown in Table 17.

The manually computed TDE and numerical enthalpy calculation match well, indicating that the CTF enthalpy model accurately captures the energy deposition in the fuel pellet. There is an over-approximation by an average of 0.5% of the energy deposition, but this is negligible and maintains CTFs' conservatism.

Table 16: Adiabatic Gap Peak RAE Calculations

Test Case	Manually Computed TDE (J/g)	Numerical Enthalpy Calculation (J/g)
1, 2, 3	665.48	669.45
4	565.4	568.63
5	770.55	775.67
6, 7, 8	709.69	713.70
9	599.74	603.09
10	819.64	824.32
11	694.7	698.70
12	774.68	778.96

Table 17: Peak RAE Calculations using Updated Numerical Scheme in CTF

Test Case	Pulse Width (ms)	Target RAE (J/g)	Manually Computed TDE (J/g)	Numerical Enthalpy Calculation (J/g)
1, 2, 3	7.5	650	665.48	656.57
4	7.5	550	565.4	561.91
5	7.5	750	770.55	761.21
6, 7, 8	90	650	709.69	654.17
9	90	550	599.74	554.33
10	90	750	819.64	754.42
11	50	650	694.7	657.46
12	300	650	774.68	679.63

The simulated HERA tests match the peak RAE target significantly closer than the prior results [88] generated using CTF.

Following the implementation of the additional post-CHF models in CTF, the HERA M&S Benchmark Part 1 test cases were run to compare performance. Results were similar for all test cases; as such, only the results for Test Case 1 and Test Case 6 are shown below. The QOIs recorded are the cladding outer surface temperature and the RAE, both at the rod axial midpoint.

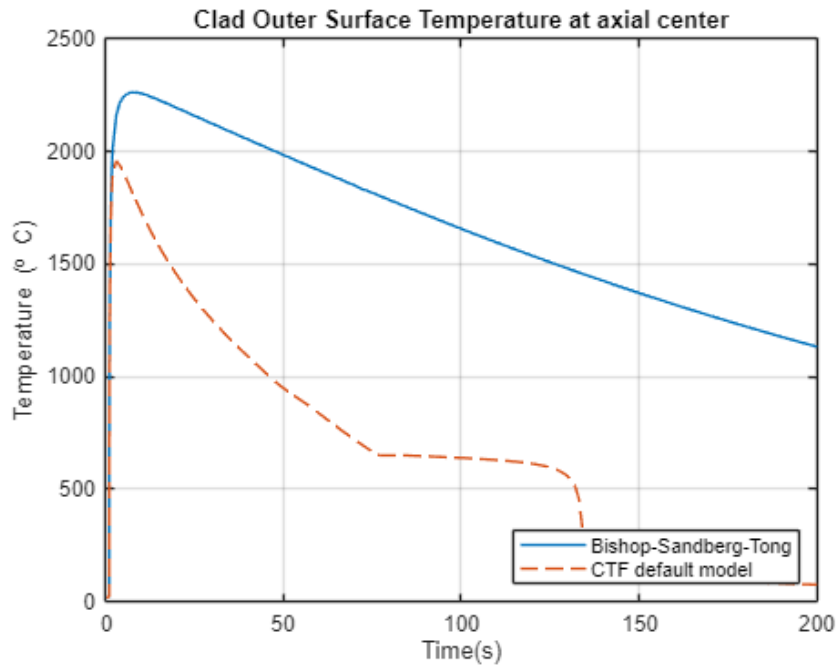


Figure 37: HERA Test Case 1 Bishop-Sandberg-Tong Peak Cladding Temperature

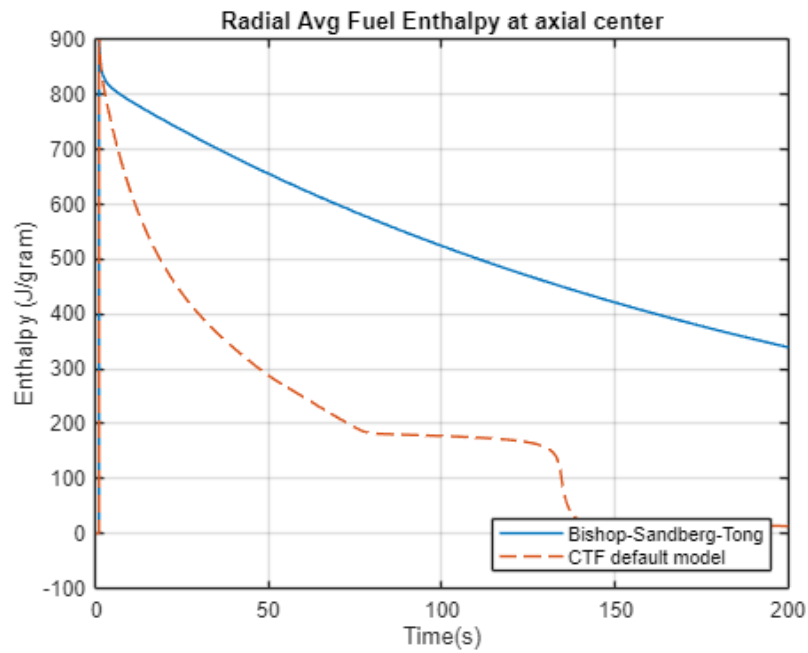


Figure 38: HERA Test Case 1 Bishop-Sandberg-Tong RAE

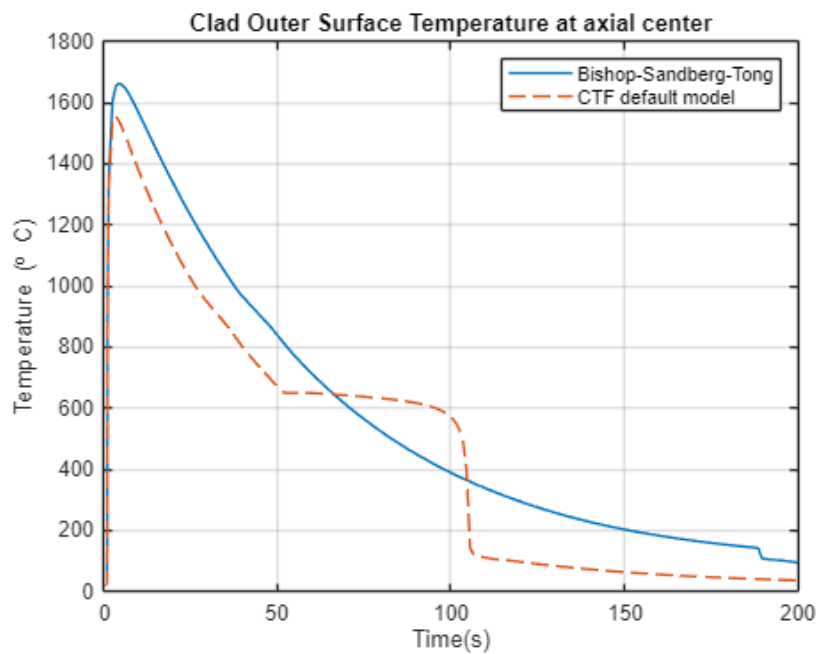


Figure 39: HERA Test Case 6 Bishop-Sandberg-Tong Peak Cladding Temperature

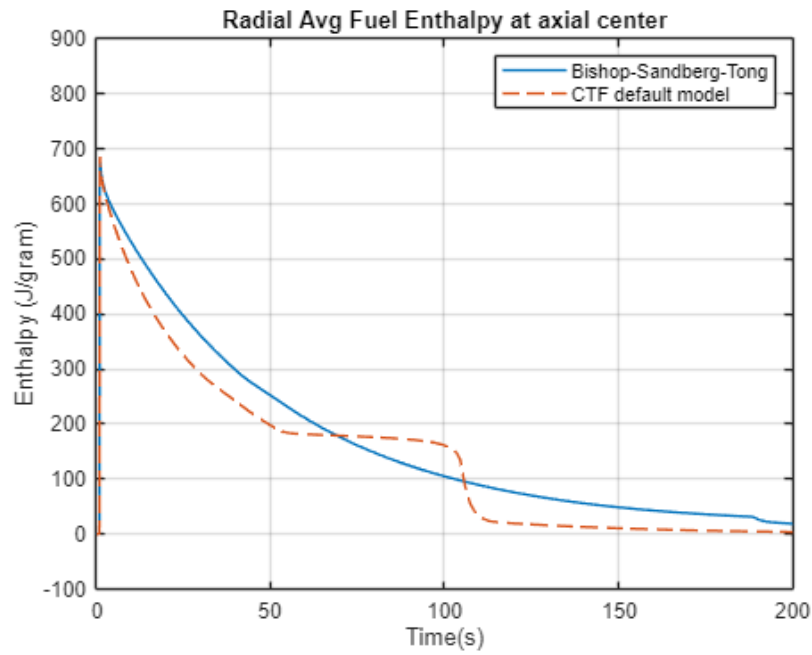


Figure 40: HERA Test Case 6 Bishop-Sandberg-Tong RAE

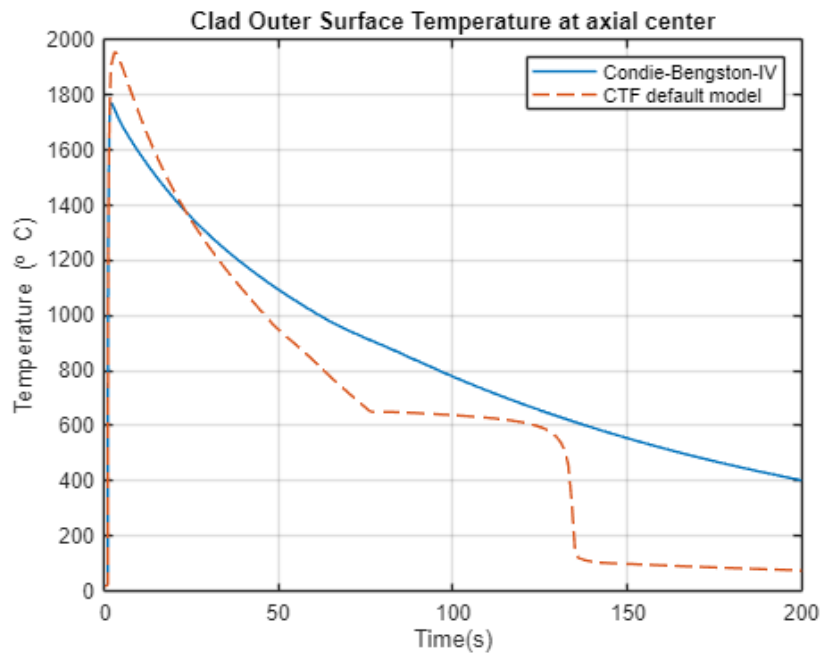


Figure 41: HERA Test Case 1 Condie-Bengston-IV Peak Cladding Temperature

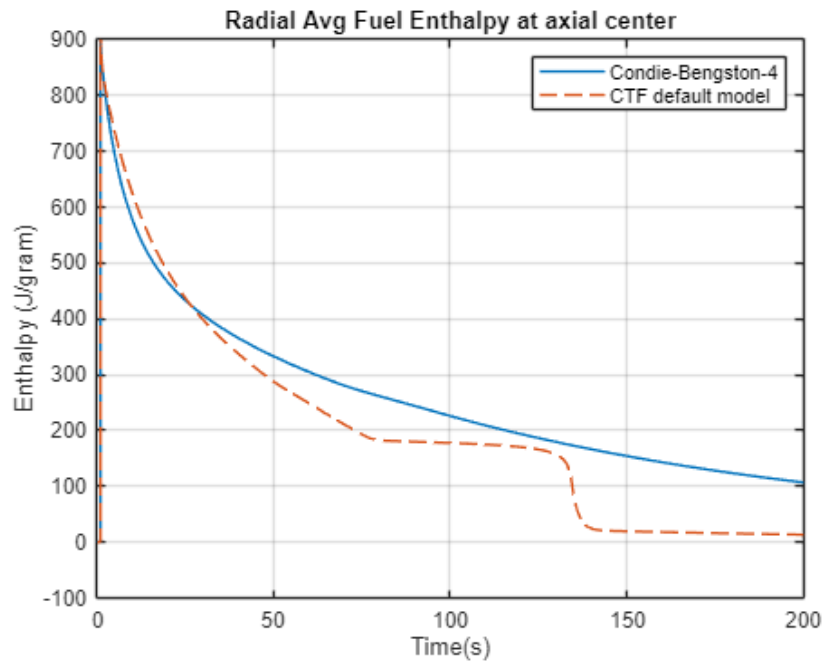


Figure 42: HERA Test Case 1 Condie-Bengston-IV RAE

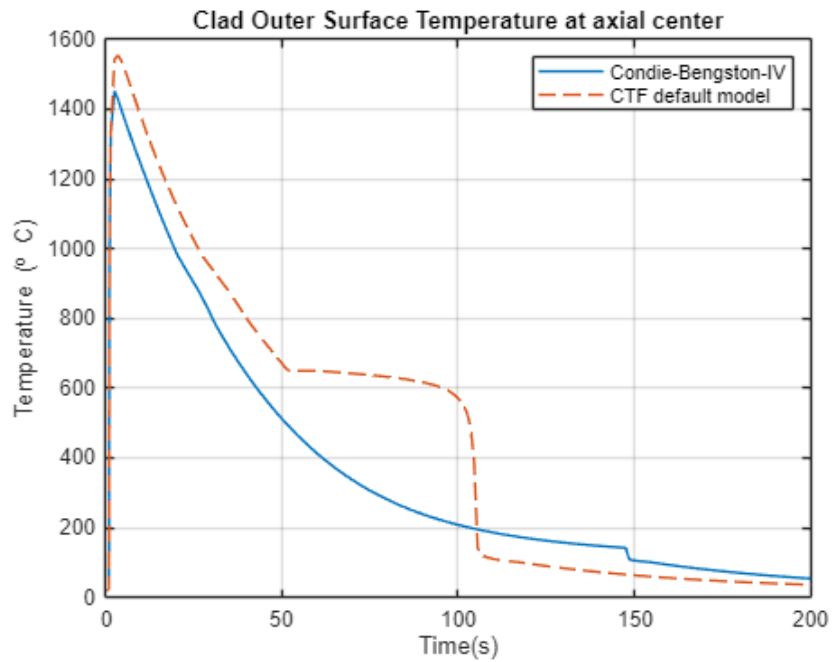


Figure 43: HERA Test Case 6 Condie-Bengston-IV Peak Cladding Temperature

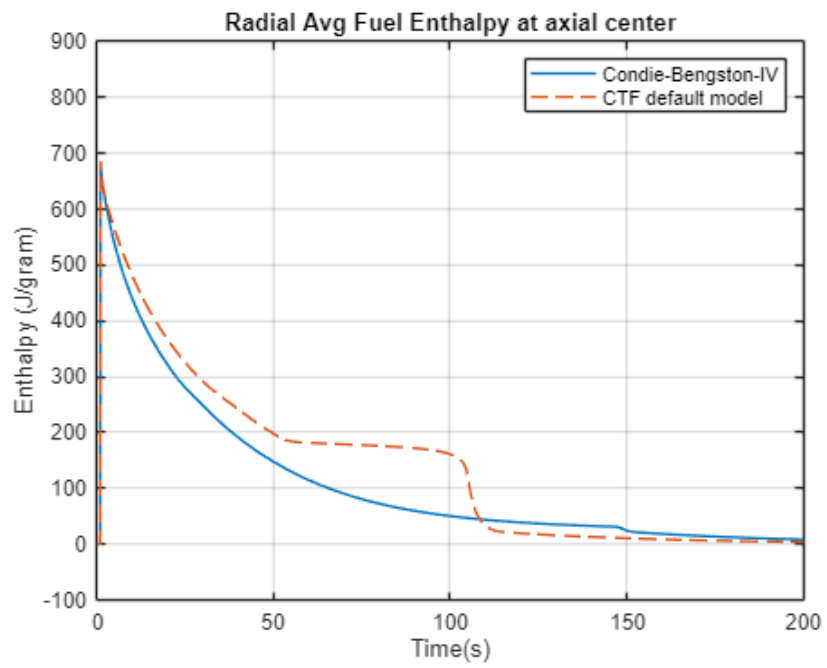


Figure 44: HERA Test Case 6 Condie-Bengston-IV RAE

CHAPTER 7 – Discussion

Discussion

The V&V of the steady state FGR model has mixed results. Around half of the cases generate acceptable FGR values compared to the FRAPCON prediction while the other half overpredict the FGR by a significant quantity. The V&V of the transient FGR model is ongoing. The enhancements in fuel performance capabilities of CTF obtain good results, where QOIs such as fuel enthalpy are calculated accurately and the output of the QOIs is of use to fuel performance and failure modeling.

Of the seventeen steady state FGR test performed, the difference between the CTFFuel FGR prediction and the FRAPCON FGR prediction is acceptable for eight cases. These cases (Case 24i6, Case 36i8, Case 111i5, Case BNFL-DE, Case BNFL-DH, Case 429-DH, Case 15309, and Case 28i6) all have a relatively high burnup, from 33.0 GWD/MTU to 98.9 GWd/MTU. They all use uniform radial power profiles, uniform axial cladding temperature profiles, and non-uniform axial power and burnup profiles. These assumptions match the assumptions used in FRAPCON and have reasonable basis for simulation purposes. The enrichments between these tests also range from 3.0 wt% to 13.0 wt%, covering a broad range. The RMSE for these test cases is also small, indicating that the difference in prediction between CTF and FRAPCON at each state point is similar. Investigation of the time-dependent figures does show that CTF has a strong tendency to overpredict the FGR earlier in the depletion, corresponding to a lower burnup.

Eight of the steady state FGR cases have significant overprediction of the CTFFuel FGR prediction compared to the FRAPCON FGR prediction. These cases (Case LFF, Case CBP, Case CBR, Case CBY, Case 4110-ae2, Case 4110-be2, Case EPL-4, and Case 597-3) all utilize the same assumptions as the more accurate cases apart from using uniform axial power and burnup profiles.

They range in burnup from 2.7 GWd/MTU to 10.4 GWd/MTU, with Case 597-3 being an outlier with a final burnup of 70.0 GWd/MTU. This aligns with what was observed in the eight higher accuracy cases, where CTF largely overpredicts the FGR at lower burnups. The uniform axial power profiles are also thought to cause extra difficulty with respect to model the temperature distribution within the fuel rod, which has a significant influence on the fission gas distribution and release in the fuel pellet.

One case, Case 332, is like Case 597-3 in the respect that it has a higher burnup but still presents a larger overprediction than the eight more accurate cases. The axial power profile is not uniform, but an overprediction of 10.77% release is still observed at the end of the depletion. The RMSE is smaller than the other cases, as with Case 597-3. Based on these observations, the conclusion is that the CTF steady state model massively overpredicts the FGR at low burnups and this error is minimized as burnup increases. Using axially uniform power profiles also gives the fuel temperature prediction model more difficulty, which can lead to incorrect fission gas concentrations in the fuel. In the case of FGR, axially uniform burnup profiles overapproximate the burnup of axial nodes near the top and bottom of the fuel rod. This will in turn artificially cause the “creation” of more fission gases than expect. A higher burnup also lowers the gas release criterion. The higher temperatures visible in the top and bottom of the rod as a result of the uniform axial power profile will accelerate the diffusion of fission gases towards grain boundaries, which are more optimal release sites. Higher nodal temperatures also lower the release criterion in CTF, causing more gas to be released than expected. While this effect is likely seen in FRAPCON as well, CTF is assumed to be more conservative in its temperature calculations, leading to a larger release.

Assessing the accuracy of the implementation in CTF is difficult due to several factors. First and foremost, the only fission gas concentration specific QOIs produced by FRAPCON is the percentage of fission gas released. This is dependent on the quantity of fission gas produced and the quantity released, allowing errors due to possible variances in the production rate of fission gases as well as the release criteria in CTF. Both quantities are heavily dependent on the temperature prediction in the fuel pellet. Differences in FRAPCON and CTF predictions will cause significant differences in the fission gas concentrations. The temperature predictions are also affected by various fuel models, for example the choice of thermal conductivity, fuel swelling models, and changes in thermal conductivity due to relocation. CTF cannot model all the same phenomena that FRAPCON does, so there will be some differences in fuel temperature predictions as a result.

The steady state FGR model is known to be applicable to burnups and enrichments that FRAPCON is licensed for, i.e. up to 62 GWd/MTU and up to 10 wt% uranium-235. In CTF, the same is true. The FRAPFGR model range of applicability depends on the range of applicability of the submodels that comprise it. The range of applicability of the fission gas solving scheme from Forsberg and Massih [30] is based on the factors that inform it, as the diffusion process is affected by burnup through the diffusion coefficient calculation. The high burnup rim thickness model is developed using fuel rods with rod average burnups of 89.5 and 97.8 GWd/MTU [83], leading us to believe it applies to fuel rods with a burnup of up to 100 GWd/MTU. The diffusion coefficient range of applicability is not provided outside of the provided FRAPCON limits, meaning it is not known if it will apply at burnups higher than 62 GWd/MTU and enrichments greater than 10 wt%. The Khoruzhii grain growth model is developed using experiments with a wide range of burnups, from around 0 to 100 GWd/MTU [64]. It finds that the maximum grain size is reached at an earlier

burnup, which can be interpreted as meaning once the burnup threshold is reached, the model applies globally. The range of enrichments used in the experiments is relatively small, less than 5 wt%. The effect of enrichment is unconfirmed based on the final model but can be assumed to apply to the same enrichment limits as FRAPCON. It may be applicable above those limits, but more investigation is required to confirm this.

The implementation of the Bishop-Sandberg-Tong and the Condie-Bengston-IV correlations yielded several important observations with respect to modeling RIAs. The primary observation is that the choice of liquid heat transfer model has a minimal effect on the peak centerline temperature and enthalpy. The differences between each model are on the order of 1 to 5 degrees Celsius and less than 3 J/g for the HERA Test Cases. The difference in peak cladding temperature predictions is more significant from model to model. Across all test cases, the Bishop-Sandberg-Tong correlation predicted the highest peak cladding temperatures and presented the slowest return to pre-CHF conditions. The Condie-Bengston-IV correlation predicted significantly smaller peak cladding temperature across all cases, visible in the peak in Figures 41 and 43. While in post-CHF conditions, the heat transfer is expected to be significantly smaller than in pre-CHF conditions (both in nucleate boiling and single phase forced convection boiling), but the model prediction shows an almost non-smooth change in temperature not visible in the other two models tested. The CTF default model predicted peak cladding temperature between the Bishop-Sandberg-Tong and Condie-Bengston-IV correlation predictions. The transition from pre- to post-CHF heat transfer is smoother than the Condie-Bengston-IV, and the heat transfer while in post-CHF is high than both the newly implemented correlations. The difference in rewet timing varies by case (i.e. pulse width, where Case 6 has a wider pulse than Case 1, resulting in a slower return to pre-CHF conditions). While not shown in all plots, all cases eventually register a return to pre-CHF

condition, indicated by the rewet point (significant drop in cladding temperature). The rewet point occurs at a higher cladding temperature for the default CTF model compared to the newly implemented models.

Results did not differ significantly between magnitude of power pulses. Larger pulses (i.e. Case 4 has a larger power spike that lasts the same amount of time than Case 1) lead to higher cladding and fuel temperatures and a slower return to pre-CHF conditions. The Bishop-Sandberg-Tong is by far the more conservative heat transfer coefficient correlation, resulting in higher temperatures and a slower return to nominal conditions. The difference between the CTF default model and the newly implemented correlations increased with shorter power pulses and with larger TDE values.

The adiabatic enthalpy predictions following the correction of the numerical enthalpy correlation matched the manually calculated TDE values to within 0.5%, with all simulations overpredicting the TDE slightly. As the calculated TDE increased, the error in predicted RAE increases, while not a significant amount. The insignificant error between the TDE and the RAE in an adiabatic case indicates that CTF accurately calculates the fuel enthalpy. Following the error correction and MATPRO-11 fuel enthalpy model implementation, it was determined that the numerical formulation was sufficiently accurate to not merit the full-time implementation of the MATPRO-11 fuel enthalpy model. The numerical formulation also has the advantage of not being dependent on material, meaning that formulation can be utilized for any material that CTF calculates the specific heat capacity without needing any modification, whereas the explicit formulation would necessitate the implementation of material specific constants.

The HERA Part 1 fuel enthalpy predictions following the error correction showed significant improvement. The predicted peak RAE values in CTF were significantly closer to the

target RAE values. They are not expected to match them exactly, as that is dependent on fuel phenomena modeled and CTF does not have the capacity to model all the phenomena occurring in nuclear fuel (i.e. the presence of hydrogen in the cladding, which is an initial condition in these tests). Even so, the enthalpy predictions were all within 5% of the target. Excluding case 12, which had a 4.5% difference in peak RAE, the next largest error was Test Case 4 with 2.1%. All other test cases presented differences at or under 1% error, lending validity to CTF's predictive ability. The error is highest in cases with shorter power pulses which mirrors what was found earlier for the adiabatic test cases. The percent error did not seem directly correlated with the magnitude of the power pulses, as in several cases with larger power pulses, the error was the same or slightly smaller than the equivalent case with smaller pulses. The largest error source appears to stem from the width of the power pulse. The exception is Case 12, with a pulse width of 300 ms. The error is significantly larger for this case. The error for the adiabatic version of this case was of similar magnitude for the other adiabatic cases. The current assumption is there is an error or bug in the input file that was not manifested in the adiabatic test case for Case 12.

The transient model V&V yielded a mix of results. The tFGR values predicted by CTF are on the same order of magnitude as both the FRAPTRAN predictions and the experimental results. It appears that at lower burnups, CTF overpredicts the tFGR. This is visible in Test Cases TS5 and OI-2. However, as burnup increases, CTF predictions cease to be conservative and the code underpredicts the release from the rods. At higher burnups, this is more evident, though the underprediction is not significant, with a maximum underprediction of 6.6 % gas released in Case NA5. Case FK-1 did not predict any fission gas release. This may be due to an approximation used to model the cladding boundary condition and power profile. Boundary conditions used in CTF were taken from the FRAPTRAN output to minimize the difference in predicted temperatures. The

FRAPTRAN output for this case was comprised of over 50,000 state points over one second, which is over the limit CTFFuel will allow for input. To model the case, the boundary was reduced by skipping three out of every four state points. Over the length of the transient the effect should be minimal but can still have an effect. The most likely possibility is that this method, which does not account for local minima in the cladding or power profiles, leading to reductions in the total energy deposited in the fuel or over/underpredictions of the cladding temperature boundary condition. This approach was repeated for all test cases other than Case NA3, NA4, and NA5, as these cases were the only ones in the test suite with a sufficiently small number of state points.

This approximation is likely to have caused some perturbation of the power profile, leading to differences in the temperature distribution within the fuel rod. This will directly affect how much gas is released, potentially leading to the discrepancy noted. This would align with the CTF predictions, where the overlooking of the local power spike present in an RIA would cause less energy deposited in the fuel. This would in turn cause the temperature distribution to be lower than FRPATRAN predicts. Another source of error in this calculation would be in the choice of fuel phenomena modeling. For example, the FRAPTRAN runs modeled the water-metal reaction that occurs between Zirconium and water using the Cathcart model, whereas CTF cannot model this. With this model active, the temperature in FRAPTRAN will be more elevated than without the model active.

The range of applicability of the tFGR model is based on the limits of the threshold temperatures and the steady state fission gas concentration model range of applicability. The threshold temperatures are determined from the CABRI and NSRR rods utilized in the FRAPTRAN-2.0 integral assessment [2], and can be taken to apply to burnups up to 66 GWd/MTU and enrichments up to 5 wt% (per the FRAPTRAN range of applicability).

CHAPTER 8 – Conclusion and Future Work

Conclusion

The steady state FGR modeling is considered fairly implemented. There are some doubts as to the accuracy of the steady state model in predicting FGR at lower burnups, especially for cases modeling with axially uniform power and burnup profiles, as these strongly affect the temperature predictions and can lead to large FGR values than in FRAPCON or other codes with less conservative temperature prediction models. The non-axially uniform power and burnup cases presented acceptable FGR values. The sources of error in the model implementation and potentially solutions are identified. Creation of a restart file for use in tFGR simulations is verified.

The tFGR model is accurately implemented and yields reasonable fission gas release values. The potential sources of error in the tFGR model implementation are identified as coarse boundary conditions potentially missing local maximums in the power profiles and cladding temperature and missing phenomena that CTF cannot currently model. The read-in of pre-existing gas concentrations from FRAPCON generated restart files is verified, and the information is processed correctly.

The implementation of additional post-CHF models resulted in several conclusions. Based on the cladding temperature predictions, the current CTF post-CHF model is considered the most accurate, with the best treatment of temperature distributions. The Bishop-Sandberg-Tong correlation is shown to be the most conservative in its approach to predicting cladding temperature and post-CHF heat transfer. The Condie-Bengston-4 correlation presents some non-smooth behavior near the peak cladding temperature that lends some doubt the accuracy of its prediction for rapid transients. The fuel enthalpy calculation methodology in CTF was investigated and errors in the implementation corrected. This correction results in excellent fuel enthalpy predictions for

uranium dioxide fuel at low burnup. Although error is noted to increase with decreasing power pulse width, the increase in error is insignificant compared to realistic power pulse widths in accident scenarios. Several avenues for improvement of the project across the steady state FGR model, the tFGR model, and the general fuel performance enhancements exist and are indicated.

Future Work

While this project has been successful in certain respects, there are areas for improvement across the model implementations. They are split between the two FGR models implemented and general improvements.

First and foremost, the tFGR model must be improved. The FGR predictions are non-conservative compared to third part code predictions and experimental values. An investigation in the model implementation with regards to the temperature predictions must be considered to improve results. Potential solutions include implementation of high burnup correction factors should the temperature prediction not be the root cause of the underprediction.

Secondly, there are several areas of improvement for the steady state model. To accurately model the fission gas concentrations, CTF uses an equi-areal radial nodalization, where the concentric rings formed by adjacent radial nodes have the same area. This differs from the default equi-distant radial nodalization used in CTF. The equi-distant approach results in better temperature predictions, but inaccurate fission gas concentrations. Forcing CTF to use equi-distant radial spacing for heat conduction calculation and using equi-volumetric spacing for FGR calculations would allow a greater degree of accuracy for both calculations. This necessitates the implementation of an interpolation scheme between the two, firstly to calculate fuel temperature at the FGR radial nodes, then to convert the FGR concentrations from FGR radial nodes to

conduction radial nodes. This will maintain the conduction equation accuracy (as it is most accurate when using equidistant nodes) while maintaining the FGR calculation accuracy. A change in the selection of the fission gas release model is also suggested to allow CTF to decide which model to use based on the current conditions. For example, the steady state fission gas release model could be used as a default if the FGR model is activated, and the transient model is used when the rate of change of temperature with respect to time is greater than a certain value.

Thirdly, for continued improvement of the CTF fuel performance capabilities not related to FGR modeling. The first suggested is continued participation in the HERA JEEP Benchmark activity to obtain access to high quality test data to gauge CTF's capabilities. In addition, some investigation of the material properties, particularly the specific heat capacity/thermal conductivity as a function of the burnup, is to be considered. A possibility would be to allow CTF to account for the increase in porosity of the fuel as a result of fission gas build up, leading to changes in the fuel thermal conductivity. Lastly, the implementation of a fuel failure model in CTF. This could come in the form of a cladding failure model depending on the hoop stress in the cladding. Another possibility could include the consideration of the hydrogen content in CTF.

References

- [1] K. J. Geelhood and W. G. Luscher, *FRAPCON-4.0: Integral Assessment*, 2015.
- [2] K. J. Geelhood and W. G. Luscher, *FRAPTRAN-2.0: Integral Assessment*, 2016.
- [3] R. Salko, M. Avramova, A. Wysocki, A. Toptan, J. Hu, N. Porter, T. Blyth, C. Dances, A. Gomez, C. Jernigan, J. Keppy and A. Abarca, *CTF Theory Manual*, CASL, 2020.
- [4] V. V. Rondinella and T. Wiss, "The high burn-up structure in nuclear fuel," *Materials Today*, vol. 13, no. 12, pp. 24-32, 2010.
- [5] H. Xiao, C. Long and H. Chen, "The formation mechanisms of high burnup structure in UO₂ fuel," *Journal of Nuclear Materials*, vol. 556, p. 3, 1 December 2021.
- [6] N. Capps, C. Jensen, F. Cappia, J. Harp, K. Terrani, N. Woolstenhulme and D. Wachs, "A Critical Review of High Burnup Fuel Fragmentation, Relocation, and Dispersal under Loss-Of-Coolant Accident Conditions," *Journal of Nuclear Materials*, p. 27, 2020.
- [7] EPRI, "Topical Report on Reactivity Initiated Accident: Bases for RIA Fuel and Core Coolability," EPRI, Palo alto, CA, 2002.
- [8] Nuclear Energy Agency, "Nuclear Fuel Behaviour Under Reactivity-initiated Accident (RIA) Conditions," OECD Publishing, Paris, 2010.
- [9] K. Lassmann, C. O'Carroll, J. v. d. Laar and C. T. Walker, "The radial distribution of plutonium in high burnup UO₂ fuels," *Journal of Nuclear Materials*, vol. 208, no. 3, pp. 223-231, 1994.
- [10] A. Leenaers, W. V. Renterghem and S. V. d. Berghe, "High burn-up structure of U(Mo) dispersion fuel," *Journal of Nuclear Materials*, pp. 218-230, 2016.
- [11] S. Bremier and C. T. Walker, "Radiation-enhanced diffusion and fission gas release from recrystallised grains in high burn-up UO₂ nuclear fuel," *Radiation Effects and Defects in Solids*, vol. 157, pp. 311-322, 2002.
- [12] J. Rest, M. W. D. Cooper, J. Spino, J. A. Turnbull, P. Van Uffelen and C. T. Walker, "Fission gas release from UO₂ nuclear fuel: a review," *Journal of Nuclear Materials*, 2018.
- [13] K. Nogita and K. Une, "Irradiation-induced recrystallization in high burnup UO₂ fuel," *Journal of Nuclear Materials*, vol. 226, no. 3, pp. 302-310, 1995.
- [14] C. T. Walker, D. Staicu, M. Sheindlin, D. Papioannou, W. Goll and F. Sontheimer, "On the thermal conductivity of UO₂ nuclear fuel at a high burn-up of around 100 MWd/kgHM," *Journal of Nuclear Materials*, p. 21, 2005.
- [15] H. Matzke and M. Kinoshita, "Polygonization and high burnup structure in nuclear fuels," *Journal of Nuclear Materials*, vol. 247, pp. 108-115, 1997.
- [16] K. Une, S. Kashibe and K. Hayashi, "Fission Gas Release Behavior in High Burnup UO₂ Fuels with Developed Rim Structure," *Journal of Nuclear Science and Technology*, pp. 668-674, 2002.
- [17] Nuclear Energy Agency, "Very High Burn-ups in Light Water Reactors," Nuclear Energy Agency, 2006.
- [18] Nuclear Energy Agency, "State-of-the-Art Report on Multi-scale Modelling of Nuclear Fuels," OECD Publishing, Paris, 2015.

- [19] U.S. NRC, "Fuel Fragmentation, Relocation, And Dispersal During the Loss-of-Coolant Accident," U.S. Nuclear Regulatory Commission, 2012.
- [20] M. Tonks, D. Andersson, R. Devanathan, R. Dubourg, A. El-Azab, M. Freyss, F. Iglesias, K. Kulacsy, G. Pastore, S. R. Phillpot and M. Welland, "Unit mechanisms of fission gas release: Current understanding and future needs," *Journal of Nuclear Materials*, vol. 504, pp. 300-317, 2018.
- [21] K. Une, S. Kashibe and A. Takagi, "Fission Gas Release Behavior from High Burnup UO₂ Fuels under Rapid Heating Conditions," *Journal of Nuclear Science and Technology*, vol. 43, no. 9, pp. 1161-1171, 2006.
- [22] B. J. Lewis, W. T. Thompson and F. C. Iglesias, "Fission Product Chemistry in Oxide Fuels," in *Comprehensive Nuclear Materials*, 2012, pp. 515-546.
- [23] P. Levi, *The periodic table*, London, England: Penguin Classics, 2000.
- [24] "Fission Product Yield," 2024. [Online]. Available: https://en.wikipedia.org/wiki/Fission_product_yield.
- [25] D. R. Olander and P. Van Uffelen, "On the role of grain boundary diffusion in fission gas release," *Journal of Nuclear Materials*, vol. 288, pp. 137-147, 2001.
- [26] Y. Li, S. Hu, R. Montgomery, F. Gao and X. Sun, "Phase-field simulations of intragranular fission gas bubble evolution in UO₂ under post-irradiation thermal annealing," *Nuclear Instruments and Methods in Physics Research Section B: Beam Interactions with Materials and Atoms*, vol. 303, pp. 62-67, 2013.
- [27] S. Kashibe, K. Une and K. Nogita, "Formation and growth of intragranular fission gas bubbles in UO₂ fuels with a burnup of 6-83 GWd.t," *Journal of Nuclear Materials*, vol. 206, no. 1, pp. 170-183, 1993.
- [28] R. White, "The development of grain-face porosity in irradiated oxide fuel," in *OECD/NEA International Seminar on Fission Gas Behavior in Water Reactor Fuels*, Cadarache, 2000.
- [29] P. Van Uffelen, "Modelling isothermal fission gas release. Technical and economic limits to fuel burnup extension," in *Technical and economic limits to fuel burnup extension*, San Carlos de Bariloche, 1999.
- [30] K. Forsberg and A. R. Massih, "Diffusion Theory of Fission Gas Migration in Irradiated Nuclear Fuel UO₂," *Journal of Nuclear Materials*, vol. 135, no. 2-3, pp. 140-148, 1985.
- [31] U.S. NRC, "Nuclear Fuel Thermal Conductivity Degradation," U.S. Nuclear Regulatory Commission, 2012.
- [32] Nuclear Energy Agency, "Fission Gas Behaviour in Water Reactor Fuels," in *Fission Gas Behaviour in Water Reactor Fuels Seminar Proceedings*, Cadarache, 2000.
- [33] J. Guo, H. Lai, W. Zhou and J. Wei, "Fission Gas Behaviors and Relevant Phenomena in Different Nuclear Fuels: A Review of Models and Experiments," *Frontiers in Energy Research*, vol. 10, 2022.
- [34] F. Al Gabr, J. Ferrandis, D. Baron and P. Chantoin, "Pressure and Composition of Gas Mixtures in Fuel Rods for Pressurized Water Reactors by an Ultrasonic Sensor," in *International conference on WWER fuel performance, modelling and experimental support*, Bulgaria, 2003.

- [35] C. T. Walker, P. Knappik and M. Mogensen, "Concerning the development of grain face bubbles and fission gas release in UO₂ fuel," *Journal of Nuclear Materials*, vol. 160, no. 1, pp. 10-23, 1988.
- [36] T. Barani, E. Bruschi, D. Pizzocri, G. Pastore, P. Van Uffelen, R. L. Williamson and L. Luzzi, "Analysis of transient fission gas behaviour in oxide fuel using BISON and TRANSURANUS," *Journal of Nuclear Materials*, vol. 486, pp. 96-110, 2017.
- [37] U.S. NRC, "Alternative Radiological Source Terms for Evaluating Design Basis Accidents at Nuclear Power Reactors," U.S. Nuclear Regulatory Commission, 2023.
- [38] M. Bales, A. Chung, J. Corson and L. Kyriazidis, "Interpretation of Research on Fuel Fragmentation, Relocation, and Dispersal at High Burnup," U.S. NRC, 2021.
- [39] W. Chen and X. Bai, "Unified Effect of Dispersed Xe on the Thermal Conductivity of UO₂ Predicted by Three Interatomic Potentials," *Journal of Materials*, pp. 1710-1718, 2020.
- [40] C. Ronchi, M. Sheindlin, D. Staicu and M. Kinoshita, "Effect of burn-up on the thermal conductivity of uranium dioxide up to 100.000 MWdt⁻¹," *Journal of Nuclear Materials*, pp. 58-76, 2004.
- [41] B. Roostaii, H. Kazeminejad and S. Khakshournia, "Including high burnup structure effect in the UO₂ fuel thermal conductivity model," *Progress in Nuclear energy*.
- [42] U.S. NRC, "Pressurized-Water Reactor Control Rod Ejection and Boiling-Water Reactor Control Rod Drop Accidents," U.S. Nuclear Regulatory Commission, 2020.
- [43] A. Toptan, R. Salko, M. Avramova, K. Clarno and D. Kropaczek, "Continuing Efforts for CTFFuel's SQA and Its Comparison to FRAPTRAN for RIA Transient," CASL, 2020.
- [44] K. J. Geelhood, W. G. Luscher, P. A. Raynaud and I. E. Porter, *FRAPCON-4.0: A Computer Code for the Calculation of Steady-State, Thermal-Mechanical behavior of Oxide Fuel Rods for High Burnup*, 2015.
- [45] Encyclopedia of Mathematics, "Simpson formula," Springer, 6 June 2020. [Online]. Available: https://encyclopediaofmath.org/index.php?title=Simpson_formula. [Accessed 19 March 2025].
- [46] M. Amaya, J. Nakamura, F. Nagase and T. Fuketa, "Thermal conductivity evaluation of high burnup mixed-oxide (MOX) fuel pellet," *Journal of Nuclear Materials*, vol. 414, no. 2, pp. 303-308, 2011.
- [47] K. Ohira and N. Itagaki, "Thermal Conductivity Measurements of High Burnup UO₂ Pellet and a Benchmark Calculation of," in *ANS International Topical Meeting on LWR Fuel Performance*, Portland, 1979.
- [48] D. L. Hagrman and G. A. Reymann, "MATPRO-Version 11: a handbook of materials properties for use in the analysis of light water reactor fuel rod behavior," n. p., United States, 1979.
- [49] P. E. MacDonald and L. B. Thompson, "MATPRO: Version 09. A handbook of materials properties for use in the analysis of light water reactor fuel rod behavior," n.p., United States, 1976.
- [50] P. G. Lucuta, H. S. Matzke and I. J. Hastings, "A Pragmatic Approach to Modeling Thermal Conductivity of Irradiated UO₂ Fuel: Review and Recommendations," *Journal of Nuclear Materials*, vol. 232, no. 2-3, pp. 166-180, 1996.

- [51] J. K. Fink, "Thermophysical properties of uranium dioxide," *Journal of Nuclear Materials*, vol. 279, no. 1, pp. 1-18, 2000.
- [52] D. D. Lanning and C. R. Hann, "Review of Methods Applicable to the Calculation of Gap Conductance," Pacific Northwest Laboratory, United States, 1975.
- [53] C. E. Beyer, C. R. Hann, D. D. Lanning, F. E. Panisko and L. J. Parchen, *User's Guide for GAPCON-THERMAL-2: A Computer Program for Calculating the Thermal Behavior of an Oxide Fuel*, Richland, Washington: Pacific Northwest Laboratories, 1975.
- [54] M. G. Cooper, B. B. Mikic and M. M. Yovanovich, "Thermal contact conductance," *International Journal of Heat and Mass Transfer*, vol. 12, no. 3, pp. 279-300, 1969.
- [55] G. Jacobs and N. Todreas, "Thermal Contact Conductance in Reactor Fuel Elements," *Nuclear Science and Engineering*, pp. 283-290, 1973.
- [56] EPRI, "Fuel Analysis and Licensing Code: FALCON MOD01: Volume 1: Theoretical and Numerical," EPRI, Palo Alto, CA, 2004.
- [57] J. D. Hales, R. L. Williamson, S. R. Novascone, G. Pastore, B. W. Spencer, D. S. Stafford, K. A. Gamble, D. M. Perez, R. J. Gardner, W. Liu, J. Galloway, C. Matthews, C. Unal and N. Carlson, "BISON Theory Manual The Equations Behind Nuclear Fuel Analysis," Idaho National Laboratory, Idaho Falls, 2016.
- [58] M. Mogensen, I. L. F. R. C. T. Walker and M. Coquerelle, "Local Fission Gas Release and Swelling in Water Reactor Fuel during Slow Power Transients," *Journal of Nuclear Materials*, vol. 131, no. 2-3, pp. 162-171, 1985.
- [59] N. E. Hoppe, "Engineering model for zircaloy creep and growth," in *Proceedings of the ANS-ENS International Topical Meeting on {LWR} Fuel Performance*, Avignon, France, 1991.
- [60] T. A. Hayes and M. Kassner, "Creep of Zirconium and Zirconium Alloys," *Metallurgical and Materials Transactions A*, vol. 37A, pp. 2389-2396, 2006.
- [61] K. J. Geelhood, "Fuel Performance Considerations and Data Needs for Burnup above 62 GWd/MTU," Pacific Northwest National Laboratory, 2019.
- [62] A. H. Booth, "A Method of Calculating Fission Gas Diffusion From UO₂ Fuel and Its application to the X-2 Loop Test," 1957.
- [63] K. Forsberg and A. R. Massih, "Fission Gas Release Under Time-Varying Conditions," *Journal of Nuclear Materials*, vol. 127, no. 2-3, pp. 141-145, 1985.
- [64] O. V. Khoruzhii, S. Y. Kourtchatov and V. V. Lihanskii, "New model of equiaxed grain growth in irradiated UO₂," *Journal of Nuclear Materials*, vol. 265, no. 1-2, pp. 112-116, 1999.
- [65] M. R. Tonks, P.-C. A. Simon and J. Hirschhorn, "Mechanistic grain growth model for fresh and irradiated UO₂ nuclear fuel," *Journal of Nuclear Materials*, vol. 542, 2021.
- [66] P. Van Uffelen, G. Pastore, V. Di Marcello and L. Luzzi, "Multiscale modelling for the fission gas behaviour in the TRANSURANUS Code," *Nuclear Engineering and Technology*, vol. 43, pp. 477-488, 2011.
- [67] M. V. Speight, "A Calculation on the Migration of Fission Gas in Material Exhibiting Precipitation and Re-solution of Gas Atoms Under Irradiation," *Nuclear Science and Engineering*, vol. 37, no. 2, pp. 180-185, 1969.

- [68] G. Pastore, L. Luzzi, V. D. Marcello and P. Van Uffelen, "Physics-based modelling of fission gas swelling and release in UO₂ applied to integral fuel rod analysis," *Nuclear Engineering and Design*, vol. 256, 2013.
- [69] G. Khvostov, "A Dynamic Model for Fission Gas Release and Gaseous Swelling Integrated into the FALCON Fuel Analysis and Licensing Code," in *Water Reactor Fuel Performance meeting/TopFuel*, Paris, 2009.
- [70] A. Scolaro, I. Clifford, C. Fiorina and A. Pautz, "The OFFBEAT multi-dimensional fuel behavior solver," *Nuclear Engineering and Design*, vol. 358, 2020.
- [71] OpenCFD, "OpenFOAM," 2024. [Online]. Available: <https://www.openfoam.com/>.
- [72] G. Zullo, D. Pizzocri and L. Luzzi, "The SCIANTIX code for fission gas behaviour: Status, upgrades, separate-effect validation, and future developments," *Journal of Nuclear Materials*, vol. 587, 2023.
- [73] P. M. Clifford, "Regulatory Guide 1.236 Fuel Rod burnup Range of Applicability," U.S. Nuclear Regulatory Commission, 2020.
- [74] K. J. Geelhood, W. G. Luscher, J. M. Cuta and I. A. Porter, *FRAPTRAN-2.0: A Computer Code for the Transient Analysis of Oxide Fuel Rods*, 2016.
- [75] G. Khvostov, "Models for numerical simulation of burst FGR in fuel rods under the conditions of RIA," *Nuclear Engineering and Design*, vol. 328, pp. 36-57, 2018.
- [76] D. T. Hagrman, C. M. Allison and G. A. Berna, "SCDAP/RELAP5/MOD 3.1 code manual: MATPRO, A library of material properties for Light-Water-Reactor accident analysis," n. p., 1995.
- [77] D. Pizzocri, G. Pastore, T. Barani, E. Bruschi, L. Luzzi and P. Van Uffelen, "Modeling of Burst Release in Oxide Fuel and Application to the TRANSURANUS Code," in *11th International Conference on WWER Fuel Performance, Modeling and Experimental Support*, Varna, 2015.
- [78] G. Pastore, D. Pizzocri, J. D. Hales, S. Novascone, D. M. Perez, B. Spencer, P. V. u. R. L. Williams and L. Luzzi, "Modelling of Transient Fission Gas Behaviour in Oxide Fuel and Application to the BISON Code," in *Proceedings of the Enlarged Halden Programme Group Meeting*, Røros, 2014.
- [79] A. A. Bishop, R. O. Sandberg and L. S. Tong, "Forced Convection Heat Transfer at High Pressure After the Critical Heat Flux," American Society of Mechanical Engineers, 1965.
- [80] D. G. Morris, C. B. Mullins and G. L. Yoder, "An Analysis of Transient Film Boiling of High-Pressure Water in a Rod Bundle," Oak Ridge National Laboratory, 1982.
- [81] G. A. Reymann, "Fuel Specific Heat Capacity (FCP) and Fuel Enthalpy (FENTHL)," U.S. NRC, 1980.
- [82] A. Abarca and M. A. K. Ivanov, "Implementation and Validation of a Fission Gas Release Model for CTFFuel using the NEA/OECD IFPE database," in *PHYSOR2020 – International Conference on Physics of Reactors: Transition to a Scalable Nuclear Future*, 2021.
- [83] R. Manzel and C. T. Walker, "EPMA and SEM of fuel samples from PWR rods with an average burn-up of around 100 MWd/kgHM," *Journal of Nuclear Materials*, vol. 301, no. 2-3, pp. 170-182, 2002.

- [84] J. M. Johns and K. J. Geelhood, "Optimization of FAST Fission Gas Release Model Parameters Using Machine Learning Accelerated Evolutionary Algorithms," in *TopFuel 2018*, 2018.
- [85] American Nuclear Society (ANS), *Method for Calculating the Fractional Release of Volatile Fission Products from Oxide Fuel*, 2011.
- [86] D. Kamerman, C. Jensen, D. Wachs and N. W. , "High-Burnup Experiments in Reactivity Initiated Accidents (HERA)," Idaho National Laboratory, 2022.
- [87] C. Jensen and D. K. C. P. Folsom, "HERA M&S Exercise Problem Description Report," Idaho National Laboratory, Idaho Falls, ID, 2022.
- [88] S. Seo, C. Folsom, C. Jensen, D. Kamerman, L. Giaccardi, M. Cherubini, P. Suk, M. Sevecek, J. Sercombe, I. Guenot-Delahaie, A. Scolaro, M. Reymond, K. Kulacs, L. H. F. Feria, P. Aragon, G. Khvostov, I. Khan, A. Deo, S. Ravva, R. Calabrese, F. Boldt, J. Sappl, J. Falk, A. Arkoma, V. Georgenthum, Y. Tasaki, K. Kakiuchi, Y. Udagawa, G. Delipei, C. Cheron, J. Corson, J. Zhang, T. Drieu, J. Klouzal, M. Dostal, V. Matocha, T. Kinkorova and C. Fiorina, "International fuel performance study of fresh fuel experiments for PCMI effects during RIA experiments," *Nuclear Engineering and Design*, vol. 430, 2024.
- [89] C. P. Folsom, J. L. Schulthess, D. W. Kamerman, N. E. Woolstenhulme, C. B. Jensen and D. M. Wachs, "Overview of the Water-Based RIA Testing in TREAT," in *TopFuel*, 2021.
- [90] B. Lee, Y. Koo and D. Sohn, "Development of a thermal conductivity correlation for the pellet rim region and its application to the analysis of behaviour of high burnup fuel," International Atomic Energy Agency, 1998.
- [91] F. Lemoine, "High burnup fuel behavior related to fission gas effects under reactivity initiated accident (RIA) conditions," *Journal of Nuclear Materials*, pp. 238-248, 1997.
- [92] A. Toptan, R. Salko, J. Hu, A. Wyxocki and M. Avramova, *CTFFuel User's Manual*, CASL, 2019.
- [93] T. Tsuruta and T. Fujishiro, "Evaluation of Thermocouple Fin effect in Cladding Surface Temperature Measurement during Film Boiling," *Journal of Nuclear Science and Technology*, pp. 515-527, 1984.

APPENDICES

Appendix A: Description of fgr.ctf input file

The “fgr.ctf” input file is an additional input file that is used in transient CTF calculations to inform the transient model of the existing gas concentrations in the fuel pellet. It is organized in the following manner:

1. The first line must be an integer equal to 3(ngasmod). This indicates to the code that the FRAPFGR model has been used to develop fission gas concentrations.
2. The second line contains the number of radial nodes (nr) in the fission gas concentration matrix. It must be equal to the number of nodes in the CTF transient calculation.
3. The third line contains a vector of nr entries that describes the radial length of each node. This is currently not used in CTF, as the model currently forces the nodalization to remain the same between the depletion and transient simulation. Future work could involve allowing interpolation between different nodalization in the simulation.
4. The next 3 lines are printed once for each axial level in the fuel pellet.
 - a. The first line is a vector of length nr that describes the fraction of gas contained in the grain boundary that can be released.
 - b. The second line is a vector of length nr that describes the fraction of gas contained in the intra-granular sinks that can be released.
 - c. The third line contains the quantity in moles of fission gas produced at that axial level (fgmp).
5. The 3 lines in part 4 are printed repeatedly for each axial level in the fuel pellet. The number of axial nodes in the depletion simulation and the transient simulation must match exactly.

An example file format is provided below, where ny is the number of axial nodes, nr, the number of radial nodes, radius (j) is the radial node length, GB(i,j) is the grain boundary fraction, where i

